EFFECT OF FIBER-REINFORCED CONCRETE

IN THIN OVERLAYS

by

Min Ook Kim

A dissertation submitted to the faculty of
The University of Utah
in partial fulfillment of the requirements for the degree of

Doctor of Philosophy

Department of Civil and Environmental Engineering

The University of Utah

May 2016

The University of Utah Graduate School

STATEMENT OF DISSERTATION APPROVAL

The dissertation of   **Min Ook Kim**

has been approved by the following supervisory committee members:

Amanda Bordelon	, Chair	**10/23/15**
		Date Approved
Chris Pantelides	, Member	**10/23/15**
		Date Approved
Pedro Romero	, Member	**10/23/15**
		Date Approved
Luis Ibarra	, Member	**10/29/15**
		Date Approved
Eunhye Kim	, Member	**10/23/15**
		Date Approved

and by   **Michael Barber**   , Chair/Dean of

the Department/College/School of   **Civil and Environmental Engineering**

and by David B. Kieda, Dean of The Graduate School.

ABSTRACT

Cracking and debonding are important considerations for pavement maintenance because they are linked with the service life of pavement structures. Concrete overlay pavements are expected to have reduced crack widths and reduced debonding rates when the concrete mixture contains fibers. The age-dependent changes in flexural and fracture properties of fiber-reinforced concrete (FRC) between 3 and 90 days were experimentally investigated. Compared to plain unreinforced concrete, steel and polymeric macro-FRC of up to 1% by volume of fibers were confirmed to have no significant effects on compressive strength, free drying shrinkage, or coefficient of thermal expansion. For both steel-fiber-reinforced concrete (SFRC) or polymeric-fiber-reinforced concrete (PFRC) mixtures, fracture properties as used in the FEA model were found, through wedge-splitting testing, to increase with age. However, the property currently used in the FRC overlay pavement design is the residual strength ratio, which was found to decrease with age for both SFRC and PFRC. A simple crack width equation was developed to predict the crack width of thin FRC overlays based on the addition of fibers to the concrete. The predicted crack widths were validated against data from a field project on variable joint spacing and subjected to temperature and humidity variations. Both the tensile and shear bond between an aged concrete and a newly cast fiber-reinforced mortar were investigated. The tensile interfacial energy between the fiber-reinforced mortar cast

against the aged and sand-blasted concrete was higher than that of plain unreinforced mortar. It was found that this tensile interfacial energy was proportional to the physical number of fibers located near the interface surface, particularly because some of the fracture path went through the mortar layer and was bridged by these fibers. No statistical trend could be found between the peak strengths associated with either the tensile or the shear bond and the addition of fibers in the overlay mixture. In addition, a performed finite element analysis (FEA) study indicated that, as expected, crack width, vertical liftoff, and debonding length all decreased as the fracture energy of the FRC increased or as the interfacial tensile bond increased. The developed crack width equation and finite element model were found to predict the crack widths within 0.19 mm (or 26%) compared to actual pavement. The previously developed FEA model was modified to resemble 150 mm thick pavement in order to to compare FRC pavement responses to that of unreinforced concrete containing dowels. Compared to completely unreinforced pavement, it was found that dowel reinforcement reduced crack widths by 3 times, while a typical 0.5% volume fraction of PFRC reduced crack widths by only 1.3 times. Dowel bars are used only in thick pavements rather than thin pavements, so among thin overlays, FRC is a good option to reduce crack width, debonding length, and vertical deflection.

To my parents

TABLE OF CONTENTS

LIST OF TABLES

LIST OF FIGURES

ACKNOWLEDGEMENTS

CHAPTER 1

INTRODUCTION

Fiber-reinforced concrete (FRC) has been widely utilized to improve the performance of plain concrete and has been used in new infrastructures as well as in rehabilitation, repair, and retrofits (ACI Committee 544, 1993; Banthia and Sheng, 1996; Banthia et al., 1996; Gilbert et al., 2012; Grzybowski and Shah, 1990; Jenq and Shah, 1986; Li et al., 1993; Song et al., 2005; Zollo, 1997). The principal role of the fibers is to control the crack widths and growth rates of FRC by resisting tensile opening across the cracks (Mindess et al., 2002). A reduced crack width has been linked to this fiber-bridging effect of FRC (Banthia et al., 1996; de Oliveira e Sousa and Gettu, 2006; Guo et al., 1999; Wang et al., 1990). Recently, use of FRC for ultrathin (<4" thick) overlays on asphalt pavement has become increasingly popular in pavement rehabilitation (Banthia et al., 2004; Harrington, 2008; Roesler et al., 2008). Fibers may be of particular benefit to thin overlays, because fibers are said to minimize crack widths, reduce surface spalling, and increase wear resistance (Rasmussen and Rozycki, 2004). Furthermore, it has been hypothesized that use of FRC can increase the load transfer efficiency, bond performance, and service life of overlay pavement.

In thin pavement, construction limitations often prevent the traditional reinforcement of dowel bars across joints, but there is further hypothesis that

fibers might provide load-transfer effects similar to those provided by dowel bars, as well as reduced vertical deflection effects.

Pavement cracking and debonding are mainly caused by stress differences between the overlay and substrate. These stresses can originate from relative humidity gradients, temperature gradients, and applied traffic loads (Denarié and Silfwerbrand, 2004). Concrete slabs undergo volume changes as environmental conditions such as humidity and temperature change. Slab curling occurs when the top and the bottom of a slab differ in drying shrinkage and temperature. Volume changes, along with restraint and friction, create internal stress that leads to cracking at the surface of the concrete overlay or cracking (later leading to debonding) at the interface between the layers (Lange and Shin, 2001). According to several researchers, relative humidity-based shrinkage is considered as the single most important factor determining the service life of concrete overlay (Granju et al., 2004; Rahman et al., 2000; Weiss et al., 1998; Yuan et al., 2003). The effects of drying shrinkage and temperature gradients on pavement systems have been studied several times (Al-Qadi et al., 2005; Aure and Ioannides, 2012; Ioannides, 2005; Kohler and Roesler, 2004; Lederle and Hiller, 2012; Tompkins et al., 2012). These studies have developed empirical equations or calibration factors that estimate volumetric changes and slab curling responses for pavement design procedures.

In concrete pavements, construction joints are placed at a certain spacing to reduce net curling deformation and to localize potential cracking to a specific known location. If the joints are too close, the cost of saw-cutting for more joints will increase and the ride quality can decrease. But if the joints are too sparse, slabs can curl significantly, often resulting in mid-panel cracks and decreased ride quality. For thin

overlay slabs constructed at 4-6" thickness, common practice guidelines recommend joints be placed at 12 to 18 times the pavement thickness (or 4-9 feet in this case) (Rasmussen and Rozycki, 2004). One FRC overlay study by Carlsward considered that crack width depends mainly on two factors: the extent of debonding and the effect of fibers bridging the crack (Carlsward, 2006). It was found that joints that cracked at early ages (within the first seven days) after concrete placement were then always the widest cracks at later ages (McCullough and Dossey, 1999). This implies that understanding cracking and debonding against the age-dependent properties of FRC is significant for the maintenance of FRC overlay pavement structures.

The FRC residual strength ratio has been utilized for the design of FRC overlay structures. However, the effects of fiber on joint crack opening, slab deflection, and the bond between substrate and overlay are not well understood yet. This is because there is a limited number of FRC pavements and fewer projects have attempted to correlate FRC's lab-tested properties to FRC pavement performance. Thus, existing designs of FRC overlays are based on either experience-based decisions or on simplified designs with estimated residual strength ratios.

The main objective of this research is to predict the crack width, vertical deflection, and underlying interfacial debonding responses of a thin FRC overlay when subjected to thermal loading. A secondary objective is to verify whether fiber properties used in design can vary with age. Fibers' effects on interfacial bonds between substrate concrete and fiber-reinforced overlays were investigated through experimentation and finite element analysis. Data from a field-constructed FRC overlay subjected only to environmental loading were used to calibrate the crack width prediction of a thin FRC

overlay.

The research is presented in five parts: the experimentally determined age-dependent FRC properties, the FRC overlay crack width prediction equation, experimentally determined interfacial bond properties, the finite element model (FEM) that predicts pavement response, and a response comparison between a dowel bar and FRC.

The first part (Chapter 3) investigates how much the mechanical properties of FRC change with age. The following properties are measured: compressive strength, free drying shrinkage, coefficient of thermal expansion, flexural strength, and fracture energy.

The second part of the study (Chapter 4) focuses on the theoretical equation, which predicts the crack width of thin FRC overlays. To validate the modified theoretical equation, the field measurements from an actual thin FRC overlay structure are utilized.

The third part (Chapter 5) identifies whether there is any fiber effect on the interfacial bond between substrate concrete pavement material and fiber-reinforced mortar overlay material. Tensile and shear bond strengths are measured using a wedge-splitting test and a bi-surface shear test, respectively.

The fourth part (Chapter 6) focuses on the developed finite element model, which predicts pavement response. Crack width, vertical deflection, and debonding length are investigated through FEM and validated using the field measurements from an actual thin FRC overlay.

Lastly, in the fifth part (Chapter 7), the effect of FRC on reducing the crack width and debonding of a jointed overlay is compared to the effect of a potential dowel reinforcement bar.

1.1 References

ACI Committee 544, Guide for Specifying, Proportioning, Mixing, Placing, and Finishing Steel Fiber Reinforced Concrete. *ACI Materials Journal* **1993**, *90(1)*, 94-103.

Al-Qadi, I.; Hassan, M.; Elseifi, M. Field and Theoretical Evaluation of Thermal Fatigue Cracking in Flexible Pavements. *Transportation Research Record: Journal of the Transportation Research Board* **2005**, *1919*, 87-95.

Aure, T. W.; Ioannides, A. M. Numerical Analysis of Fracture Process in Pavement Slabs. *Canadian Journal of Civil Engineering* **2012**, *39(5)*, 506-514.

Banthia, N.; Gupta, R.; Mindess, S. Developing Crack Resistant FRC Overlay Materials for Repair Applications. *NSF Conference, Bergamo, Italy* **2004**, 99-106.

Banthia, N.; Sheng, J. Fracture Toughness of Micro-Fiber Reinforced Cement Composites. *Cement and Concrete Composites* **1996**, *18(4)*, 251-269.

Banthia, N.; Yan, C.; Mindess, S. Restrained Shrinkage Cracking in Fiber Reinforced Concrete: a Novel Test Technique. *Cement and Concrete Research* **1996**, *26(1)*, 9-14.

Carlswärd, J. Shrinkage Cracking of Steel Fibre Reinforced Self Compacting Concrete Overlays: Test Methods and Theoretical Modeling. Doctoral Thesis, Luleå University of Technology, Sweden, 2006.

de Oliveira e Sousa, J. L. A.; Gettu, R. Determining the Tensile Stress-Crack Opening Curve of Concrete by Inverse Analysis. *Journal of Engineering Mechanics* **2006**, *132(2)*, 141-148.

Denarié, E.; Silfwerbrand, J. Structural Behaviour of Bonded Concrete Overlays. *RILEM Workshop on Bonded Concrete Overlays* **2004**, 38-45.

Gilbert, R.; Bradford, M.; Gholamhoseini, A.; Chang, Z.-T. Effects of Shrinkage on the Long-Term Stresses and Deformations of Composite Concrete Slabs. *Engineering Structures* **2012**, *40*, 9-19.

Granju, J.-L.; Sabathier, V.; Turatsinze, A.; Toumi, A. Interface Between an Old Concrete and a Bonded Overlay: Debonding Mechanism. *Interface Science* **2004**, *12(4)*, 381-388.

Grzybowski, M.; Shah, S. P. Shrinkage Cracking of Fiber Reinforced Concrete. *ACI Materials Journal* **1990**, *87(2)*, 138-148.

Guo, X.; Tin-Loi, F.; Li, H. Determination of Quasibrittle Fracture Law for Cohesive Crack Models. *Cement and Concrete Research* **1999**, *29(7)*, 1055-1059.

Harrington, D. Guide to Concrete Overlays. *National Concrete Pavement Technology Center. Ames, IA* **2008**.

Ioannides, A. Stress Prediction for Cracking of Jointed Plain Concrete Pavements, 1925-2000: An Overview. *Transportation Research Record: Journal of the Transportation Research Board* **2005**, *1919*, 47-53.

Jenq, Y.; Shah, S. Crack Propagation in Fiber-Reinforced Concrete. *Journal of Structural Engineering* **1986**, *112(1)*, 19-34.

Kohler, E.; Roesler, J. Active Crack Control for Continuously Reinforced Concrete Pavements. *Transportation Research Record: Journal of the Transportation Research Board* **2004**, *1900*, 19-29.

Lange, D.; Shin, H.-C. Early Age Stresses and Debonding in Bonded Concrete Overlays. *Transportation Research Record: Journal of the Transportation Research Board* **2001**, *1778*, 174-181.

Lederle, R.; Hiller, J. New Warping and Differential Drying Shrinkage Models for Jointed Plain Concrete Pavements Derived with Nonlinear Shrinkage Distribution. *Transportation Research Record: Journal of the Transportation Research Board* **2012**, *2305*, 3-13.

Li, V. C.; Stang, H.; Krenchel, H. Micromechanics of Crack Bridging in Fibre-Reinforced Concrete. *Materials and Structures* **1993**, *26(8)*, 486-494.

McCullough, B.; Dossey, T. Considerations for High-Performance Concrete Paving: Recommendations from 20 years of Field Experience in Texas. *Transportation Research Record: Journal of the Transportation Research Board* **1999**, *1684*, 17-24.

Mindess, S.; Young, J. F.; Darwin, D. *Concrete*. Prentice Hall: New Jersey, 2002.

Rahman, M.; Baluch, M.; Al-Gadhib, A. Simulation of Shrinkage Distress and Creep Relief in Concrete Repair. *Composites Part B: Engineering* **2000**, *31(6)*, 541-553.

Rasmussen, R. O.; Rozycki, D. K. *Thin and Ultra-Thin Whitetopping: A Synthesis of Highway Practice*. Transportation Research Board: **2004**, *338*.

Roesler, J.; Wang, D. An Analytical Approach to Computing Joint Opening in Concrete Pavements. *Pavement Cracking: Mechanisms, Modeling, Detection, Testing and Case Histories* **2008**, *79*.

Song, P.; Hwang, S.; Sheu, B. Strength Properties of Nylon-and Polypropylene-Fiber-Reinforced Concretes. *Cement and Concrete Research* **2005**, *35(8)*, 1546-1550.

Tompkins, D.; Saxena, P.; Khazanovich, L.; Gotlif, A. Modification of Mechanistic-Empirical Pavement Design Guide Procedure for Two-Lift Composite Concrete Pavements. *Transportation Research Record: Journal of the Transportation Research Board* **2012**, *2305*, 14-23.

Wang, Y.; Li, V. C.; Backer, S. Experimental Determination of Tensile Behavior of Fiber Reinforced Concrete. *ACI Materials Journal* **1990**, *87(5)*, 461-468.

Weiss, W. J.; Yang, W.; Shah, S. P. Shrinkage Cracking of Restrained Concrete Slabs. *Journal of Engineering Mechanics* **1998**, *124(7)*, 765-774.

Yuan, Y.; Li, G.; Cai, Y. Modeling for Prediction of Restrained Shrinkage Effect in Concrete Repair. *Cement and Concrete Research* **2003**, *33(3)*, 347-352.

Zollo, R. F. Fiber-Reinforced Concrete: An Overview after 30 years of Development. *Cement and Concrete Composites* **1997**, *19(2)*, 107-122.

CHAPTER 2

LITERATURE REVIEW

2.1 Fiber Reinforced Concrete Properties

2.1.1 Toughness

Fiber-reinforced concrete (FRC) has been quantified to improve toughness (Banthia and Sheng, 1996; Jenq and Shah, 1986; Kim and Bordelon, 2015; Li et al., 1993; Song et al., 2005; Wang et al., 1990). Figure 2.1 shows a schematic representation of fibers bridging across a crack under tension. There is a traction-free zone where the crack is wide enough for all of the fibers to have pulled out, a fiber-bridging zone in which stresses are transferred by the frictional slip of the fibers, and a micro-cracked matrix process zone with enough aggregate interlock to transfer some stress within the matrix itself (Mindess et al., 2002). At the fiber-bridging zone, the matrix cannot carry a load across the crack surface, but the fibers carry all postcracking loads taken by the composite. In this bridging zone, the fibers tend to transfer the tensile stress to the matrix through shear frictional bond stresses.

2.1.2 FRC Shrinkage

Shrinkage is a leading contributor to slab curling, joint opening, and the widening of cracks found in pavement.
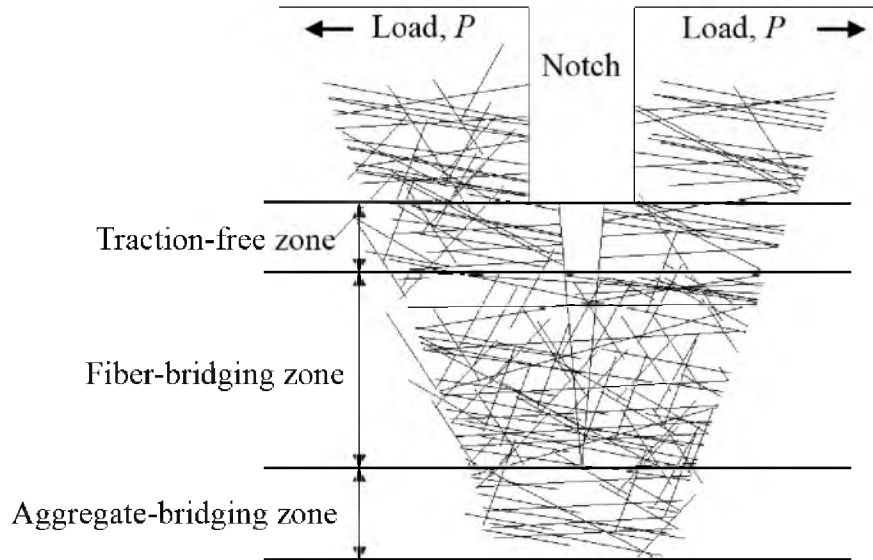
Figure 2.1. Schematic representation of fibers bridging across a crack under tension.

Although this research focuses only on the use of macrofibers, the use of microfibers at a low volume fraction ($V_f < 1\%$) is commonly thought to reduce shrinkage cracking (Mehta and Monteiro, 2006). However, the role of microfibers in reduced shrinkage is still controversial, as some experimental studies have demonstrated a reduction in free shrinkage and others show negligible effects on free shrinkage (Balaguru and Ramakrishnan, 1988; Mangat and Azari, 1988; Sanjuan, 1999; Swamy and Stavrides, 1979). This phenomenon might be related to the fiber type, fiber distribution, and different casting or testing conditions.

Research has shown that when low amounts of polypropylene or nylon fibers (0.1% of volume fraction) are added to concrete, plastic shrinkage cracking can be reduced (Folliard and Berke, 1997). Gryzbowski and Shah (1990) found that the addition of fibers as low as 0.25% by volume substantially reduced crack widths resulting from restrained drying shrinkage (Gryzbowski and Shah, 1990).

2.1.3 FRC Overlay Interfacial Bond

Since stresses from differential expansion and contraction are the highest at boundaries, such as cracks, joints or edges, these stresses can lead to debonding (Delatte et al., 2000). If the vertical and axial stresses at the interface exceed the bond strength between the overlay and the substrate, the overlay will begin to debond. Debonding of the overlay from the underlying substrate can be a separate phenomenon or can be concurrent with the effects of shrinkage curling and loading strains in a pavement slab. The effect of steel fibers on debonding have been investigated in a laboratory, and it has been found that steel fiber does not increase bond strength itself, but delays the crack-opening rate after crack initiation (Granju, 1996). Figure 2.2 shows some results from the article (Granju, 1996).
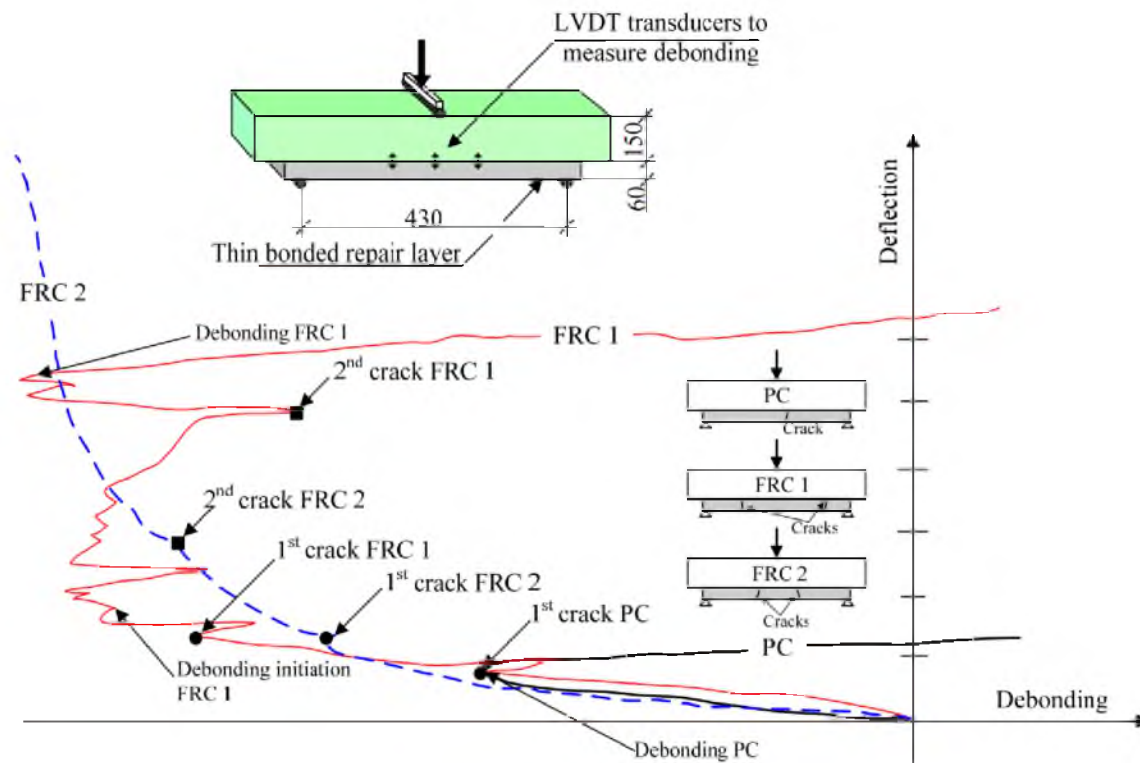
Figure 2.2. Influence of steel fibers on the debonding and cracking of repair layers (Granju, 1996).

A SFRC mixture containing 1.0% V_f was found to have initial debonding when the first crack developed through the overlay, yet exhibited delay in propagation of the debonded area. A different steel fiber type at 0.4% V_f exhibited no debonding itself. Field experimental studies have suggested a stronger bond occurs with steel-macrofiber-reinforced concrete (SFRC) overlays as compared to unreinforced or polymeric-macrofiber-reinforced concrete (PFRC) (Chanvillard et al., 1989; Delatte et al., 2000).

2.1.4 Age-Effect

Some researchers reported that the widths of cracks formed at early ages were greater than the widths of the same cracks at later-ages (McCullough and Dossey, 1999). This implies that understanding cracking and debonding behavior at early ages is significant for the maintenance of concrete pavement structures. Some experimental studies have been carried out to investigate the age-dependent properties of FRC (Bernard, 2015; Bordelon, 2007; Chan and Li, 1997; Hodicky et al., 2013). An earlier study by Bernard, which tested FRC at different ages from 7 to 365 days, found that SFRC exhibited a constant residual strength ratio between 7 and 90 days while PFRC showed a decreasing residual strength ratio from 7 to 90 days (Bernard, 2015). Bordelon also reported a reduction of residual strength ratio of PFRC between 7 and 28 days (Bordelon, 2007). Conversely to flexural tests, a wedge-split fracture test by Hodicky and coworkers found that the fracture energy and tensile strength of SFRC were increased with age (Hodicky et al., 2013). On a microstructure level, the fiber-to-cement interfacial bond between 0.5 to 28 days, as determined from a pull-out test, was found to increase only within the first 2 days, but have no significant change from 7 to 28 days (Chan and Li, 1997).

2.2 Pavement Design

2.2.1 Response due to Environmental Loading

Figure 2.3 shows schematic figures of shrinkage curling and temperature curling. The pavement slabs can be exposed to significant temperature and moisture gradients, depending on the temperature and moisture exposure conditions. To further complicate the curling response, the temperature and moisture gradient occurring in the slab at the time of setting can create a permanent curling response, called "built-in curling". Temperature and moisture gradients can cause the slabs either to curl to greater magnitudes or may actually act counter to the built-in curling and produce a slab that appears uncurled. The weight of the slab upon high curling deformation can sometimes be high enough to create a flexural stress that exceeds the strength of a slab and causes a mid-panel crack to form.

(a) Pavements without any deformation

(b) Curling due to drying shrinkage ($\varepsilon_{sh,Top} > \varepsilon_{sh,Bottom}$)

(c) Day, downward curling due to temperature ($T_{Top} > T_{Bot}$)

(d) Night, upward curling due to temperature ($T_{Top} < T_{Bot}$)
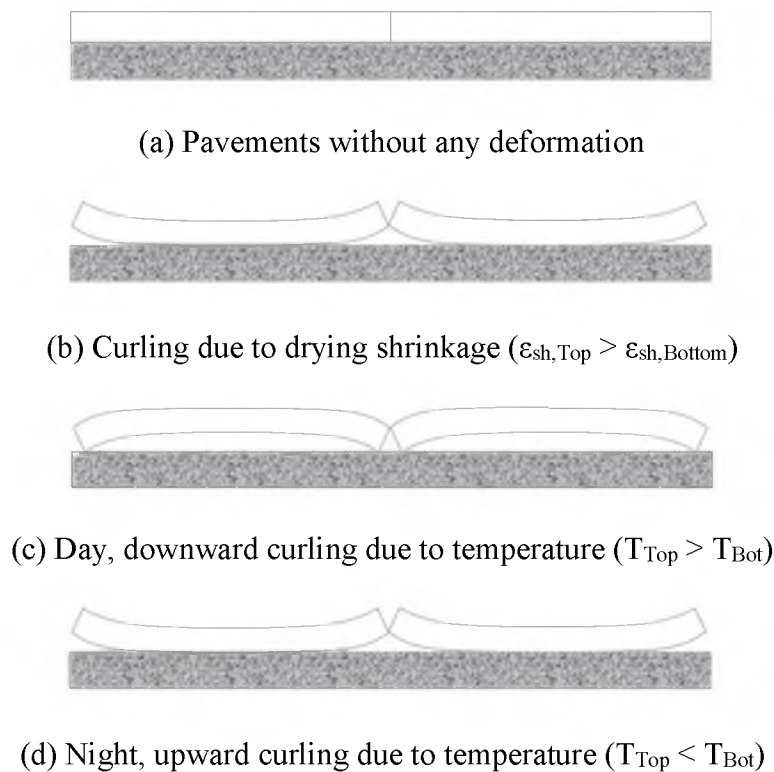
Figure 2.3. Schematics of curling response in pavement slabs.

In this research, fiber effect on built-in curling was not investigated, while both temperature gradient and shrinkage will significantly influence built-in curling response.

2.2.2 Fiber-Reinforced Concrete in Pavement Design

The addition of fibers has been shown the increased flexural capacity of concrete structures such as slabs or ultra-thin whitetopping (UTW). According to the American Concrete Pavement Association (ACPA) procedure, current FRC pavement design is based on the measured FRC residual strength properties. A residual strength ratio, R_{150}, which is determined from ASTM C1609 (2007), is utilized for FRC overlay design. It is recommended that the majority of UTW use a R_{150} of 20%, which is similar to the Illinois Department of Transportation's specified value (Roesler et al., 2008). Pavement thickness can be reduced with an increased amount of macrofibers in a paving mixture. This reduction in thickness can also contribute to the reduction of total cost for pavement construction. As pavement thickness is reduced, it is anticipated that higher fiber content is required to reduce pavement cracking or deflection under the same loading condition. However, age-dependent changes in R_{150} are not fully understood yet, while R_{150} measured at 28 days is usually utilized.

2.2.3 Failures with Thin Overlays

Thinly bonded overlay-substrate composites are intended to move monolithically, and the bond at the interface ensures the continuity of deformations between the overlay and the base. It is expected that most FRC pavement will show its cracking in corners, while the extended service life of FRC pavement still unknown. Some researchers have

stated that whenever debonding is found, typically corner cracking will occur (Emmons et al., 2000; Vaysburd and Emmons, 2000).

2.3 Controlling and Predicting Crack Widths

Wider cracks may allow transport of moisture and have low shear or tensile bridging stress, and thus curl more and deteriorate faster. Cracks can be further controlled by the use of dowel bars and tie bars as longitudinal and transverse reinforcement, respectively, or by using a continuous reinforcing bar system, as done with continuously reinforced concrete pavements (Kohler and Roesler, 2004).

2.3.1 Saw-cut Joint Spacing

Currently, the joint opening of jointed plain concrete pavement (JPCP) is approximated using Eq. (2.1), originally from Darter and Barenberg's study and used in the AASHTO pavement design guide for thicker (> 6 in.) or greater pavements (Darter and Barenberg, 1977; AASHTO, 1993).

$$\Delta L = CL_{slab}\big(\alpha_t \Delta T_{air} + (\varepsilon_{sh,free} - \varepsilon_{sh,res})\big) \qquad (2.1)$$

where ΔL: joint opening caused by temperature change and drying shrinkage of concrete; C: adjustment factor due to slab-subbase friction; L_{slab}: joint spacing or slab length; α_t: coefficient of thermal expansion of concrete; ΔT_{air}: difference in extreme air temperature over a 1 month timespan; $\varepsilon_{sh,free}$: free drying shrinkage of concrete; $\varepsilon_{sh,res}$: restrained shrinkage at the bottom of the slab. The adjustment coefficient, C, was derived using

limited field testing data but is still utilized in current modeling (Minkarah et al., 1981). It was originally developed from empirical data, and it was found that values of 0.65 or 0.8 are adequate to describe either a stabilized base or granular subbase, respectively (Papagiannakis and Masad, 2008).

2.3.2 Reinforcement across Cracks and Joints

Besides pavements, ordinary reinforced concrete (RC) structures can also contain fibers. Researchers have attempted to determine crack spacing and crack widths for these structures (ENV-1992-1-1, 1991; Jansson et al., 2010; Kelpša et al., 2014; Löfgren, 2007; RILEM TC162-TDF, 2000). A structural beam design accepted by RILEM TC 162-TDF (2000) and CNR DT 204-2006 (2006) has incorporated the benefits of steel fiber reinforcement. The structural RILEM/CNR design proposal is a modification of a crack width calculation that was originally developed for an unreinforced concrete from ENV 1992-1-1(1991).

$$w = \beta * s * \varepsilon_{bar} \tag{2.2}$$

$$S_{rm} = \left(50 + 0.25 k_{bond} k_{strain} \frac{d_{bar}}{A_{bar}/A_{beam}}\right) * k_a \tag{2.3}$$

$$k_a = \left(\frac{50}{L_f/D_f}\right) \leq 1.0 \tag{2.4}$$

where w: average crack width; β: coefficient relating the average crack width with beam design value; s: average crack spacing; ε_{bar}: strain in the tension (nonfiber) reinforcement; k_{bond}: coefficient of bond properties of tensile (nonfiber) reinforcement; k_{strain}: coefficient that takes account of the form of strain distribution; d_{bar}: tensile (nonfiber) reinforcement

bar diameter; A_{bar}: tensile (nonfiber) reinforcement cross-sectional area; A_{beam}: beam cross-sectional area; and L_f/D_f: fiber aspect ratio.

The original beam crack width and spacing equations are modified in this RILEM/CNR calculations with an empirically determined reduction factor k_a (see Eq. 2.4). The $50/(L_f/D_f)$ factor was determined because it was found to empirically match the average crack spacing of the tested SFRC slabs. However, this factor considers the influence only of the aspect ratio of the steel fibers, but it does not consider the fiber content or other properties of the fiber.

Löfgren (2007) and Jansson and coworkers (2010) have further proposed a modification: they state that the factor provided better prediction of crack spacing for steel FRC compared to the k_a (Löfgren, 2007; Jansson et al., 2010). The average crack width, according to Löfgren (2007), can be expressed as

$$w = s_{max}\left(\varepsilon_{bar} - \varepsilon_{frc}\right) \tag{2.5}$$

$$S_{max} = 3.4c + 0.425k_{bond}k_{strain}k_b \frac{d_{bar}}{A_{bar}/A_{beam}} \tag{2.6}$$

$$k_b = \left(1 - \frac{f_{residual}}{f_{mor}}\right) = (1 - R_{150}) \tag{2.7}$$

where s_{max}: the maximum crack spacing; ε_{bar}: strain in the nonfiber reinforcement; ε_{frc}: strain in the remaining fiber-reinforced concrete between cracks: k_{bond} and k_{strain} are the same as in the RILEM/CNR method; and c: concrete cover depth. The $f_{residual}/f_{mor}$ ratio was determined by Löfgren using a flexural beam test according to RILEM TC162-TDF (2000). Eqs. (2.4) and (2.7) will be utilized to modify Eq. (2.1) and modified equation will be validated in Chapter 4.

2.4 Quantifying FRC Benefits to Crack Control

2.4.1 Residual Strength Ratio

The design of FRC overlays utilizes a residual strength ratio which is the measured FRC postcracking stress normalized by the flexural strength at first cracking. Residual strength ratio has been used to represent the flexural toughness of FRC in concrete overlay design (Bordelon and Roesler, 2011). Un-notched flexural beam specimens can represent realistic applications, which normally would not have a prescribed crack initiation location or propagation orientation.

Several standardized empirical tests have been developed, as shown in Figure 2.4, such as the testing of a thin round panel under center loading to simulate point load cracking (ASTM C1550, 2008), the testing of a flexural un-notched beam with third-point or center-point loading to simulate flexural bending strength and toughness (ASTM C1609, 2007; JCI-SF4, 1984), and the testing of a flexural un-notched beam loaded against a rigid plate to determine residual strength from distributed cracking and distributed energy (ASTM C1399, 2007). Each of these test procedures has been developed to simulate or predict FRC behavior for a specific or unique loading situation. Thus, many of these tests are performed to a given cut-off deflection or displacement level that often relates to expected cracking magnitudes for that loading situation. For example, the ASTM C1609 (2007) and JCI-SF4 (1984) both use third-point bending beams of dimensions 150 × 150 × 500 mm (with a span of 450 mm) and calculate the area under the load-deflection curve until 3 mm of deflection is reached. These un-notched test specimens are size- and geometry-dependent, and thus reproducible results can only be obtained by following the specifications of the standards.
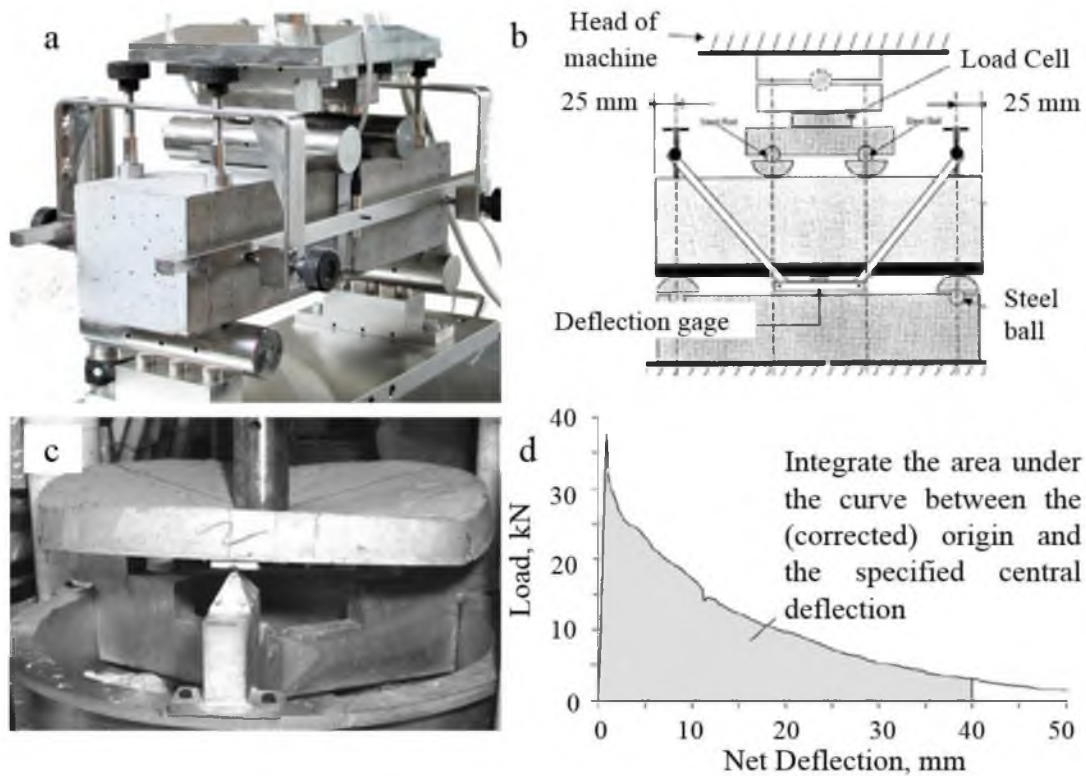
Figure 2.4. Test methods for determining toughness or residual strength properties of FRC, including: a) simply supported flexural beam bending tests (from ASTM C1609, 2007), b) uniformly-supported flexural bending beam test (from ASTM C1399, 2007), and c) round panel tests (from ASTM C1550, 2008); d) load versus deflection plot schematic showing calculated area for toughness at 40mm deflection with the round panel test results.

It is also reported that many of these un-notched specimens have high variability in the measured properties, especially for thinner or smaller specimens (Gopalaratnam et al., 1991), where random individual fibers may dominate the measurement if a crack should propagate through the fiber's spatial location.

2.4.2 Fracture Energy

The total fracture energy G_F is one of the main parameters for characterizing the unique benefit of the fiber reinforcement occurring after a crack has initiated. A common

method of measuring G_F of plain unreinforced concrete was proposed by Hillerborg (1985). Based on this method, G_F is obtained from the area under the completed load versus crack mouth opening displacement (CMOD) curve from a notched specimen, divided by the total crack ligament area. However, there is no existing technique to determine specimen geometry- or size-independent values of the total fracture energy for unreinforced or FRC. Fracture properties of FRC are commonly assessed using a beam test. An example of such a test is a single-edge notched three-point bending (SENB) specimen (Hillerborg, 1985; Jenq and Shah, 1985), shown in Figure 2.5. For all fracture tests, the total fracture energy (G_F) or work of fracture is determined from the total energy, normalized to the fracture area. For a notched beam used in a fracture test, the total fracture energy can be calculated as shown in Eq. (2.8).

$$G_F = \frac{\left[\int_0^{\delta final}(P-CMOD)\right]-W_0}{(h-a_0)b} \qquad (2.8)$$

where P is the applied load; $CMOD$: the crack mouth opening displacement: δ_{final}: the final displacement reading at the end of the test; W_0: the self-weight of the beam; h: the beam depth, a_0: the initial notch length, b: the beam width.
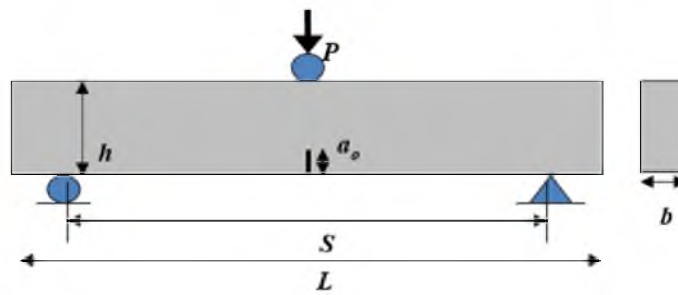
Figure 2.5. Schematic of the single-edge notched beam test.

Even based on plain unreinforced concrete tests, Bazant and coworkers (2010) indicated that there is a large scatter in the calculated total fracture energy using the Hillerborg method (1985). Investigation of experimental data reveals that the coefficient of variation of G_F is almost twice as large as that of G_f. Much of this scatter is hypothesized to originate from: 1) inherent randomness in the tail end of the load-CMOD curve, 2) uncertainty in extrapolating the tail end of the curve to zero load, and 3) difficulty eliminating nonfracture sources of energy dissipation. Figure 2.6 shows load versus CMOD curves of FRC (Bordelon, 2007).

	P_{max} (kN)	G_f (N/m)	G_{F_2mm} (N/m)	G_{F_4mm} (N/m)	G_{F_total} (N/m)
sample 1	3.28	49.5	567	1190	2809
sample 2	2.97	63.0	515	918	1802
sample 3	2.81	36.6	215	305	340
sample 4	3.31	37.1	301	761	681
sample 5	3.22	43.7	305	1145	1167
COV	7%	24%	40%	41%	72%

— Vf = 0.5% (66 lb) 38mm length crimped steel FRC, tested at 7 days
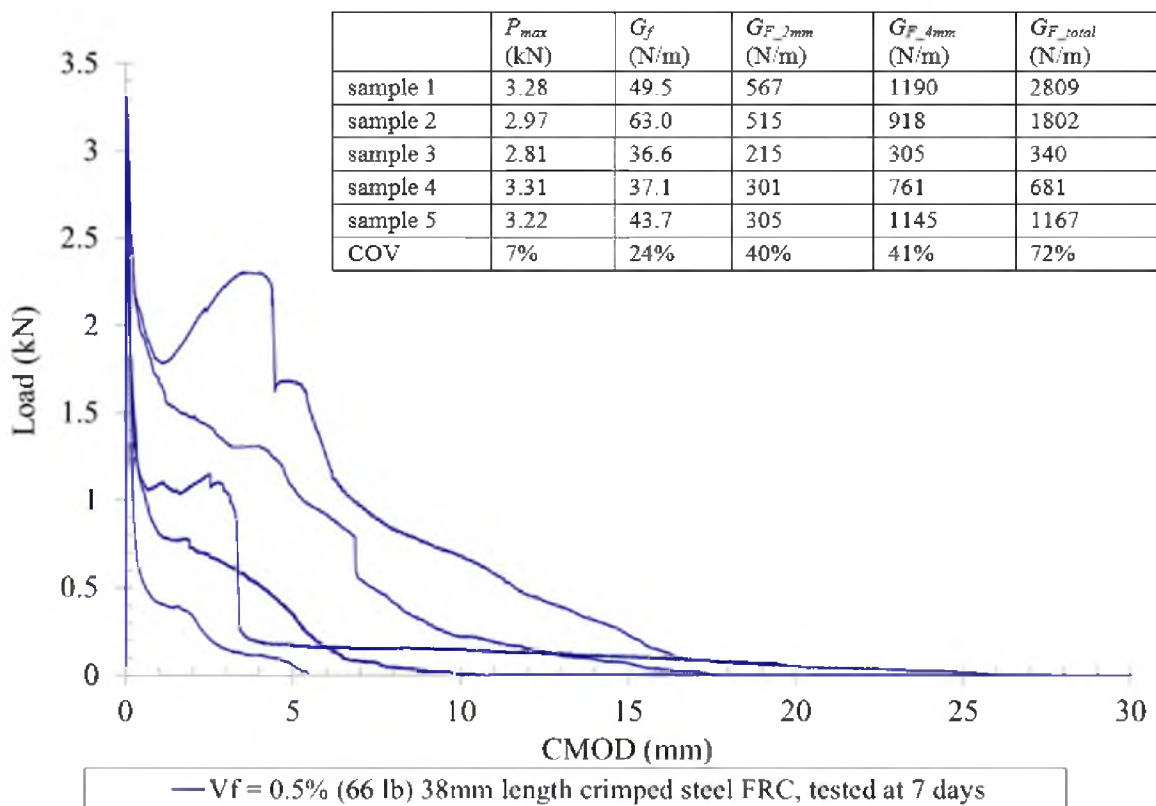
Figure 2.6. Load versus CMOD curves (Bordelon, 2007; Roesler et al., 2008) for replicate samples of the same SFRC mixture (at 0.5% fiber by volume of concrete) tested at 7 days age as a single-edge-notched beam until complete failure.

With FRC, additional scatter in the total fracture energy has been found due to nonuniform dispersion, subsequent nonuniform pull-out performance (as seen in Figure 2.6), and again interpretations of where the tail end of the curve is defined.

For replicate samples of the same FRC mixture, the measured total fracture energy can have even a 72% coefficient of variation (Bordelon, 2007; Roesler et al., 2008). Furthermore, it may be unrealistic to exhibit any structure containing FRC which would have crack openings seen in many of these tests, such as up to 40 or 50 mm of crack opening. Many laboratories may not be equipped to measure the CMOD values large enough for the complete failure of these beam specimens. Therefore, the majority of researchers have tried to focus fracture testing on only capturing the initial fracture energy, G_f, critical stress intensity factor, K_{IC}, or critical crack opening displacement $CTOD_c$. These initial fracture properties are based on the initiation of cracking and do not capture the crack propagation information significantly altered by the addition of fiber reinforcement in concrete. There is no technique to determine specimen-geometry- or size-independent values of the total fracture energy for unreinforced or FRC.

One alternative solution to quantifying the postcracking response of FRC, but without requiring full specimen failure, is called a cut-off criterion method. For the majority of flexure tests with low-volume fraction FRC, there is often some significantly small residual load carried by the bending beam at the larger displacements. Thus, this alternative approach to the Hillerborg method is to utilize a cut-off displacement value as the final displacement in the calculation of the total fracture energy (Bordelon, 2007; Roesler et al., 2007). For example, if the application of the FRC is anticipated to have design cracks less than 2 mm in opening, fracture energy (G_{F_2mm}) can be calculated up to

2 mm of CMOD. This cut-off criterion method was implemented in this research with existing flexural toughness tests done on un-notched beams, in which 150 mm beam specimens are loaded until 4 mm of midspan deflection.

Previous researchers recommend a wedge-split tension or compact-disc tension (see Figure 2.7) instead of a SENB because the fracture area is larger relative to the specimen volume and weight. Usually the self-weight of these compact specimens is also found to be negligible. According to Brühwiler and Wittmann (1990), this larger fracture area produces a more stable and more consistent fracture energy calculation (Brühwiler and Wittmann, 1990). It is anticipated that the variation in the measured total fracture energy would be significantly lower for these compact specimen tests. The minimum dimensions of these tests are recommended by Brühwiler and Wittmann (1990) to be roughly 3 or 4 times that of the fiber length or maximum aggregate size in order to reduce the variations created by random individual fiber pull-out, dispersion, and orientation effects.
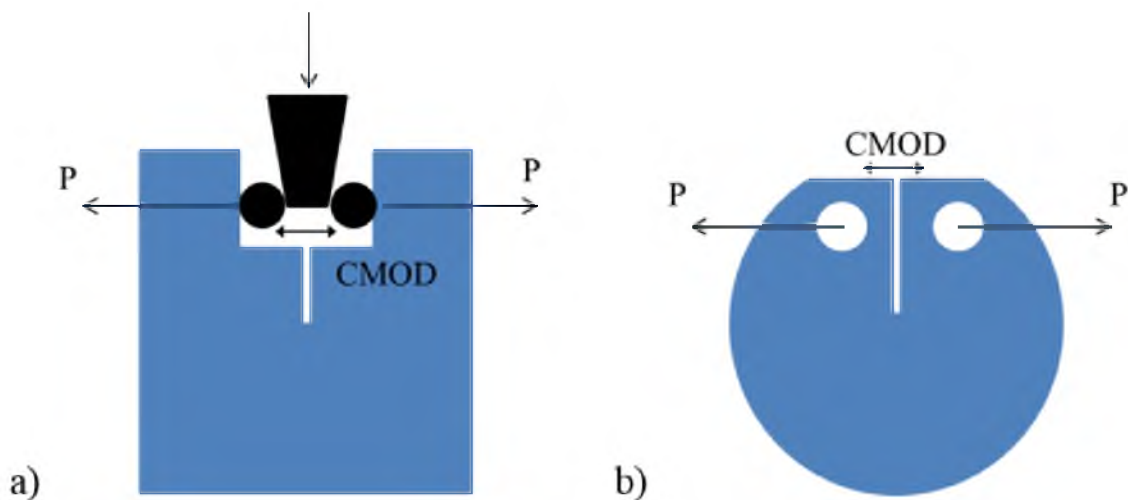
Figure 2.7. Schematics of a) wedge-split compact tension and b) compact disc tension fracture test specimens.

2.5 References

AASHTO, *AASHTO Guide for Design of Pavement Structures*, AASHTO, 1993.

ASTM Standard C1399, Standard Test Method for Obtaining Average Residual-Strength of Fiber-Reinforced Concrete. ASTM C1399/C1399M-10, West Conshohocken Pennsylvania: 2007.

ASTM Standard C1550, Standard Test Method for Flexural Toughness of Fiber Reinforced Concrete (Using Centrally Loaded Round Panel). ASTM C1550-12a, West Conshohocken Pennsylvania: 2008.

ASTM Standard C1609, Standard Test Method for Flexural Performance of Fiber Reinforced Concrete (Using Beam with Third-Point Loading). ASTM C1609/C1609M-05, West Conshohocken Pennsylvania: 2007.

Balaguru, P.; Ramakrishnan, V. Properties of Fiber Reinforced Concrete: Workability, Behavior under Long-Term Loading, and Air-Void Characteristics. *ACI Materials Journal* **1988**, *85(3)*, 189-196.

Banthia, N.; Sheng, J. Fracture Toughness of Micro-Fiber Reinforced Cement Composites. *Cement and Concrete Composites* **1996**, *18(4)*, 251-269.

Bažant, Z.; Yu, Q.; Cusatis, G.; Cedolin, L.; Jirásek, M. Misconceptions on Variability of Fracture Energy, Its Uniaxial Definition by Work of Fracture, and Its Presumed Dependence on Crack Length and Specimen Size. *Fracture mechanics of concrete and concrete structures, Proceedings of the 7th international conference on fracture mechanics of concrete and concrete structures (FraMCoS-7), Jeju, Korea* **2010**, *1*, 29-37.

Bernard, E. S. Age-Dependent Changes in Post-Crack Performance of Fibre Reinforced Shotcrete Linings. *Tunnelling and Underground Space Technology* **2015**, *49*, 241-248.

Bordelon, A. Fracture Behavior of Concrete Materials for Rigid Pavement Systems. MS Thesis, University of Illinois at Urbana-Champaign, Urbana, IL, 2007.

Bordelon, A.; Roesler, J. Flowable Fibrous Concrete for Thin Concrete Inlays. *Transportation and Development Institute Congress* **2011**, 874-883.

Brühwiler, E.; Wittmann, F. The Wedge Splitting Test, a New Method of Performing Stable Fracture Mechanics Tests. *Engineering Fracture Mechanics* **1990**, *35(1)*, 117-125.

Chan, Y.-W.; Li, V. C. Age Effect on the Characteristics of Fibre/Cement Interfacial Properties. *Journal of Materials Science* **1997**, *32(19)*, 5287-5292.

Chanvillard, G.; Aitcin, P.; Lupien, C. Field Evaluation of Steel Fiber Reinforced Concrete Overlay with Various Bonding Mechanisms. *Transportation Research Record: Journal of the Transportation Research Board* **1989**, *1226*, 48-56.

Darter, M. I.; Barenberg, E. J. Zero-Maintenance Design for Plain Jointed Concrete Pavements. Proceedings of the International Conference on Pavement Design, Purdue University, 1977.

Delatte, N. J.; Williamson, M. S.; Fowler, D. W. Bond Strength Development with Maturity of High-Early-Strength Bonded Concrete Overlays. *ACI Materials Journal* **2000**, *97(2)*, 272-280.

Emmons, P. H.; CzarneckiI, L.; McDonald, J. E.; Vaysburd, A. Durability of Repair Materials: Current Practice and Challenges. *International Symposium on Brittle Matrix Composites* **2000**, 263-274.

ENV-1992-1-1, *Eurocode 2: Design of Concrete Structures: Part 1-1: General Rules and Rules for Buildings.* British Standards Institution: 1991.

Gopalaratnam, V. S.; Shah, S. P.; Batson, G.; Criswell, M.; Ramakishnan, V.; Wecharatana, M. Fracture Toughness of Fiber Reinforced Concrete. *ACI Materials Journal* **1991**, *88(4)*, 339-353.

Granju, J. Thin Bonded Overlays: About the Role of Fiber Reinforcement on the Limitation of Their Debonding. *Advanced Cement Based Materials* **1996**, *4(1)*, 21-27.

Grzybowski, M.; Shah, S. P. Shrinkage Cracking of Fiber Reinforced Concrete. *ACI Materials Journal* **1990**, *87(2)*, 138-148.

Hillerborg, A. The Theoretical Basis of a Method to Determine the Fracture Energy G_F of Concrete. *Materials and Structures* **1985**, *18(4)*, 291-296.

Hodicky, K.; Hulin, T.; Schmidt, J. W. Wedge Splitting Test on Fracture Behaviour of Fiber Reinforced and Regular High Performance Concretes. *13th International Concrete on Fracture* **2013**.

Jansson, A.; Löfgren, I.; Gylltoft, K. Flexural Behaviour of Members with a Combination of Steel Fibres and Conventional Reinforcement. *Nordic Concrete Research* **2010**, *2(42)*, 155-171.

JCI-SF 4, JCI Standards for Test Methods of Fiber Reinforced Concrete. Japan Concrete Institute: 1984.

Jenq, Y.; Shah, S. Crack Propagation in Fiber-Reinforced Concrete. *Journal of Structural Engineering* **1986**, *112(1)*, 19-34.

Kelpša, Š.; Augonis, M.; Daukšys, M.; Augonis, A. Analysis of Crack Width Calculation of Steel Fibre and Ordinary Reinforced Concrete Flexural Members. *Journal of Sustainable Architecture and Civil Engineering* **2014**, *6(1)*, 50-57.

Kim, M. O.; Bordelon, A. Determination of Total Fracture Energy for Fiber-Reinforced Concrete. *ACI Special Publication* **2015**.

Kohler, E.; Roesler, J. Active Crack Control for Continuously Reinforced Concrete Pavements. *Transportation Research Record: Journal of the Transportation Research Board* **2004**, *1900*, 19-29.

Li, V. C.; Stang, H.; Krenchel, H. Micromechanics of Crack Bridging in Fibre-Reinforced Concrete. *Materials and Structures* **1993**, *26(8)*, 486-494.

Löfgren, I. Calculation of Crack Width and Crack Spacing. *Nordic Mini Seminar: Fibre reinforced concrete, Trondheim, Norway* **2007**, 1-12.

Mangat, P.; Azari, M. M. Shrinkage of Steel Fibre Reinforced Cement Composites. *Materials and Structures* **1988**, *21(3)*, 163-171.

McCullough, B.; Dossey, T. Considerations for High-Performance Concrete Paving: Recommendations from 20 years of Field Experience in Texas. *Transportation Research Record: Journal of the Transportation Research Board* **1999**, *1684*, 17-24.

Mehta, P. K.; Monteiro, P. J. *Concrete: Microstructure, Properties, and Materials.* McGraw-Hill: New York, 2006; Vol. 3.

Mindess, S.; Young, J. F.; Darwin, D. *Concrete.* Prentice Hall: New Jersey, 2002.

Minkarah, I.; Cook, J.; McDonough, J. Magnitude of Horizontal Movement in Jointed Concrete Pavements. *Transportation Research Record* **1981**, *821*, 61-67.

Papagiannakis, A. T.; Masad, E. A. *Pavement Design and Materials.* John Wiley & Sons: New Jersey, 2008.

RILEM TC162-TDF, Test and Design Methods for Steel Fibre Reinforced Concrete: Bending Test. *Mater Struct*, **2000**, *33*, 3-5.

Roesler, J.; Paulino, G.; Gaedicke, C.; Bordelon, A.; Park, K. Fracture Behavior of Functionally Graded Concrete Materials for Rigid Pavements. *Transportation Research Record: Journal of the Transportation Research Board* **2007**, *2037*, 40-49.

Roesler, J. R.; Bordelon, A.; Ioannides, A.; Beyer, M.; Wang, D. *Design and Concrete Material Requirements for Ultra-Thin Whitetopping*; 0197-9191; Illinois Center for Transportation: 2008.

Sanjuan, M. Effect of Low Modulus Sisal and Polypropylene Fibre on the Free and Restrained Shrinkage of Mortars at Early Age-Optimisation to Control Plastic Shrinkage. *Cement and Concrete Research* **1999**, *29(10)*, 1597-1604.

Song, P.; Hwang, S.; Sheu, B. Strength Properties of Nylon-and Polypropylene-Fiber-Reinforced Concretes. *Cement and Concrete Research* **2005**, *35(8)*, 1546-1550.

Swamy, R.; Stavrides, H. Influence of Fiber Reinforcement on Restrained Shrinkage and Cracking. *ACI Journal Proceedings* **1979**, *76(3)*, 443-460.

Vaysburd, A.; Emmons, P. How to Make Today's Repairs Durable for Tomorrow-Corrosion Protection in Concrete Repair. *Construction and Building Materials* **2000**, *14(4)*, 189-197.

Wang, Y.; Li, V. C.; Backer, S. Experimental Determination of Tensile Behavior of Fiber Reinforced Concrete. *ACI Materials Journal* **1990**, *87(5)*, 461-468.

CHAPTER 3

AGE-DEPENDENT PROPERTIES OF FIBER-REINFORCED CONCRETE

USED IN CONCRETE OVERLAY

3.1 Introduction

This chapter presents the experimental tests to quantify whether the age of testing,

fiber type, fiber length, fiber aspect ratio, or fiber volume content affect the flexural and

fracture properties of fiber-reinforced concrete (FRC). Age-dependent flexural and fracture

properties of FRC were investigated through various experimental studies. Standard

flexural beam and wedge-splitting fracture tests were conducted for FRC samples of ages

between 3 and 90 days, which can represent a range in service life performance for which

an overlay section is expected to already have cracked from initial temperature fluctuations

and may continue to develop additional joint cracks. The general concrete properties of

compressive strength, free drying shrinkage, and coefficient of thermal expansion were

also measured but expected not to change due to the fiber content.

3.2 Mixture Design and Test Variables

Table 3.1 shows the concrete mixture proportions utilized in this study. All FRC

specimens were cast with the same mass proportions in the concrete, but with varying

volumetric dosages of fibers.

Table 3.1 Plain concrete and FRC mix proportions

Material		Plain	Short Steel	Long Steel	Long Polymeric	Slender and Long Polymeric
Water		167 kg/m^3 (281 pcy)				
Cement		292 kg/m^3 (492 pcy)				
Fly Ash		125 kg/m^3 (211 pcy)				
Coarse Aggregate		1052 kg/m^3 (1773 pcy)				
Fine Aggregate		857 kg/m^3 (1445 pcy)				
High-Range Water Reducer		1028 mL/m^3 (26.4 fl.oz./yd^3)				
Air Entraining Admixture		107 mL/m^3 (2.7 fl.oz./yd^3)				
Fiber	(for 0.5% volume fraction)	0	40 kg/m^3 (67 pcy)	40 kg/m^3 (67 pcy)	4.5 kg/m^3 (7.6 pcy)	4.5 kg/m^3 (7.6 pcy)
	(for 1.0% volume fraction)	0	79 kg/m^3 (133 pcy)	79 kg/m^3 (133 pcy)	9.0 kg/m^3 (15 pcy)	9.0 kg/m^3 (15 pcy)

All had the same dosage of polycarboxylate high-range water reducer. This dosage was determined based on the previous research (Bordelon, 2007). The fibers were selected to cover different material types of steel versus polymeric, different fiber lengths of 35 mm (1.38 in.) to 60 mm (2.36 in.), and different aspect ratios (65 versus 90). The four selected macrofibers (two steel and two polymeric) were studied as listed in Table 3.2. All of these selected fibers are commonly used in concrete overlay or thin shell structures. All fibers were dispersed by hand and mixed for 2 minutes into a rotary drum mixer, after the plain concrete was mixed. The FRC was placed in the molds using a hand scoop and vibrated using a vibrating table. FRC specimens were demolded after 24 hours of casting and moist cured at a temperature around 30 °C (86 °F). Specimens were tested within 6 hours after being removed from the fog room. Specimens for free drying shrinkage were placed in a controlled temperature and humidity chamber at 23 °C (73 °F) and 50% relative humidity after demolding.

Table 3.2 Properties of fibers

Fiber Type	Short Steel	Long Steel	Long Polymeric	Slender and Long Polymeric
Material	Hooked steel	Hooked steel	Polypropylene	Polypropylene-polyethylene
Cross section	Circular	Circular	Rectangular (bi-tapered)	Rectangular (straight)
Length	35 mm (1.4 in.)	60 mm (2.4 in.)	50 mm (2.0 in.)	40 mm (1.6 in.)
Diameter	0.55 mm (0.022 in.)	0.9 mm (0.035 in.)	-	-
Thickness	-	-	0.4 mm (0.016 in.)	0.11 mm (0.004 in.)
Width	-	-	1.2 mm (0.047 in.)	1.4 mm (0.055 in.)
Aspect ratio	65	65	75	90
Tensile strength	1345 MPa (195 ksi)	1160 MPa (168 ksi)	550 MPa (79.8 ksi)	620 MPa (89.9 ksi)
Elastic modulus	210 GPa (30.5 Msi)	210 GPa (30.5 Msi)	7.0 GPa (1.01 Msi)	9.5 GPa (1.38 Msi)
Photograph				

3.3 Test Specimens and Measurement Ages

The compressive strength of FRC was determined using an average of three standard cylinder specimens according to the ASTM C39 (2005). The flexural strength of FRC was determined using an average of two standard 150 × 150 × 533 mm (6 × 6 × 21 in.) beams with a span of 450 mm (18 in.) and a constant loading rate of 0.10 mm/min (0.004 in./min), according to the ASTM C1609 (2007). A mounted deflection frame and a calculated average deflection from two LVDTs were used to measure the midspan deflection on the flexure beams. All strengths were measured from samples at the ages of

3, 7, 14, 28, 56, and 90 days.

Fracture properties of the FRC were determined using an average of two cube specimens of 150 × 150 × 150 mm (6 × 6 × 6 in.) with a 50 mm (2 in.) initial notch length. Cube specimens were tested according to a wedge-splitting tensile test as shown in Figure 3.1 (Brühwiler and Wittmann, 1990). The splitting force was applied with 9.1 degrees of total angle wedge through a roller assembly at a constant deflection rate of 1 mm/min (0.04 in./min); crack-opening displacement (COD) was recorded from two LVDTs mounted to the sides of the specimen near the initial notch tip. Fracture properties were measured at the age of 7, 28, and 56 days. The coefficient of thermal expansion was recorded according to AASHTO T336-11 (2011), and only one sample at 1% volume fraction of each fiber type was utilized at one age (roughly 30 days).
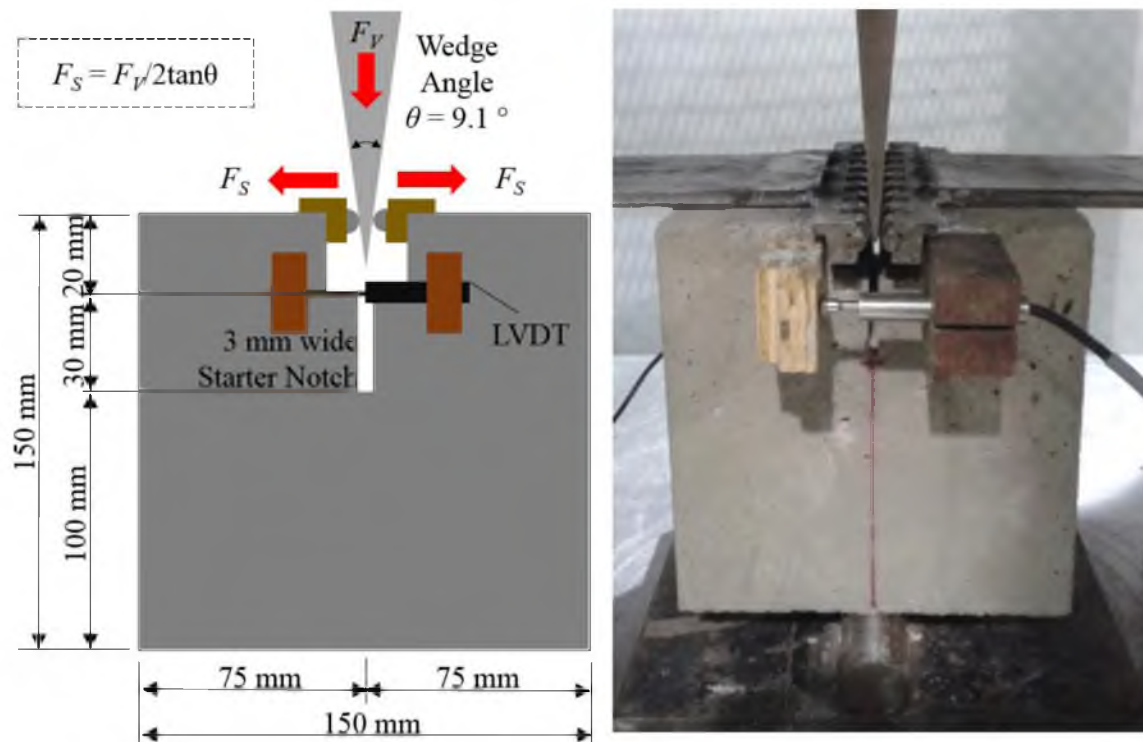
Figure 3.1. Wedge-splitting test configuration and photograph of setup.

The free drying shrinkage of the FRC was determined using an average of three standard 75 × 75 × 286 mm (3 × 3 × 11.25 in.) prismatic specimens according to ASTM C157 (2004). Shrinkage tests were conducted at ages 1, 3, 7, 14, 28, 56, and 90 days.

3.4 Data Analysis

The properties from the flexural beam test were analyzed according to three different standards such as ASTM C1609 (2007), JCI-SF 4 (1984), and Naaman and Reinhardt (2006). Figure 3.2 shows a typical load versus deflection curve of FRC. It is stated that FRC shows either deflection-hardening or deflection-softening behavior. The first peak load (P_1) is defined as the first point on the load-deflection curve when the slope is zero and the concrete initially cracks.
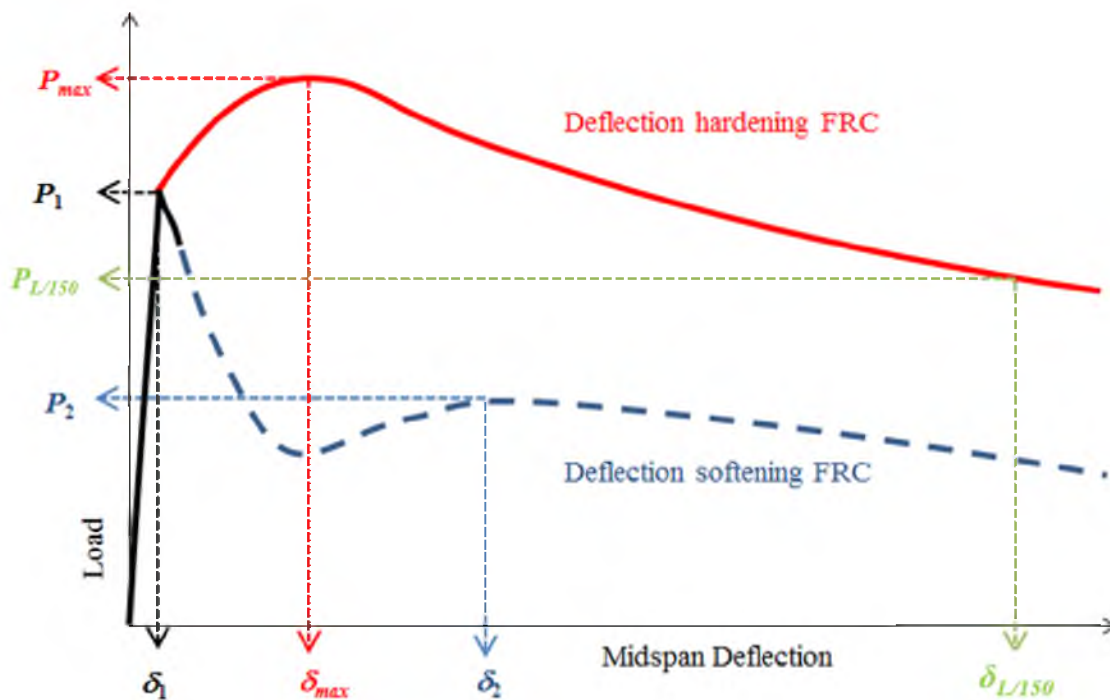
Figure 3.2. Typical load-deflection curves of FRC.

The reported modulus of rupture (MOR) is determined as the flexural strength from this first cracking. In some deflection-hardening samples, the sample continues to carry load to a higher value, in this case the ultimate load is defined as P_{max} (Kim et al., 2008; Mobasher et al., 2014; Naaman and Reinhardt, 2006). Naaman and Reinhardt (2006) suggests also recording the secondary peak load for deflection-softening samples, in this case labelled P_2.

The recorded load values are summarized as follows:

1. P_1: First-crack load; either used for MOR with deflection softening, or called the Limit of Proportionality with deflection hardening

2. P_{max}: Maximum peak load for deflection hardening

3. P_2: Second peak load for deflection softening

4. $P_{L/150}$: the load reading for when the midspan deflection reaches 1/150 of the span

The stresses are then calculated at the first crack, and maximum deflection-hardening peak or deflection-softening second peak based on Eqs. (3.1), (3.2), or (3.3), respectively.

$$f_1 = P_1 \cdot \frac{L}{bh^2} \tag{3.1}$$

$$f_{max} = P_{max} \cdot \frac{L}{bh^2} \tag{3.2}$$

$$f_2 = P_2 \cdot \frac{L}{bh^2} \tag{3.3}$$

where L is the span length, b is the width of specimen, and h is the height of specimen.

Based on the ASTM C1609 standard (2007), the residual strength and residual strength ratio both can be calculated using Eqs. (3.4) and (3.5), as shown below.

$$f_{L/150}^{ASTM} = P_{L/150} \cdot \frac{L}{bh^2} \tag{3.4}$$

$$R_{150}^{ASTM} = \frac{f_{L/150}}{f_1} \times 100 \tag{3.5}$$

The JCI-SF4 standard calculates the residual strength and residual strength ratio both based on the toughness, or the area under load-deflection, as shown in Eqs. (3.6), (3.7), and (3.8), respectively.

$$f_{L/150}^{JCI} = \frac{T_{L/150}}{L/150} \cdot \frac{L}{bh^2} \tag{3.6}$$

$$R_{150}^{JCI} = \frac{f_{L/150}}{f_1} \times 100 \tag{3.7}$$

$$T_{L/150} = area(P \cdot \delta)_0^{L/150} \tag{3.8}$$

where $T_{L/150}$ is the area under load-deflection curve between 0 and L/150 of deflection.

To analyze the results of the wedge-splitting test, the splitting force, F_S, and a cut-off total fracture energy, $G_{FRC,\ 2.5mm}$, were calculated using Eqs. (3.9) and (3.10).

$$F_S = \frac{F_V}{2 \tan \theta} \tag{3.9}$$

$$G_{FRC,2.5mm} = \frac{area(F_S \cdot COD)_0^{2.5}}{A} \tag{3.10}$$

where F_V is the vertical force applied through the wedge, as shown in Figure 3.1; θ is the total wedge angle, as shown in Figure 3.1; *area* is the sum of the area under the F_S versus average COD curve between 0 and 2.5 mm (0.1 in.) of averaged COD values, and A is the area of the fracture path.

3.5 Experimental Results and Discussion

3.5.1 Compressive Strength

Table 3.3 shows the calculated P values between f_c of plain unreinforced concrete and f_c of each fiber reinforced concrete. Figure 3.3(a) and (b) show the measured compressive strengths for steel-fiber-reinforced concrete (SFRC) and polymeric-fiber-reinforced concrete (PFRC), respectively. Based on the calculated P values, it can be seen that fiber affects on compressive strength for both SFRC and PFRC are not significant. Namely, SFRC showed the same or reduced compressive strengths with age, while PFRC exhibited all reduced compressive strengths with age. Overall, test results did not show any trends between the addition of fibers and the measured compressive strength of FRC at different ages.

Table 3.3 P values (two-tailed) between f_c of plain concrete versus f_c of each fiber reinforced concrete

Steel Fiber		Polymeric Fiber	
Type and contents (%)	P value	Type and contents (%)	P value
Short steel 0.5%	0.986	Long polymeric 0.5%	4.0E-4 (FRC strength lower than plain)
Short steel 1.0%	2.0E-6 (FRC strength lower than plain)	Long polymeric 1.0%	2.3E-5 (FRC strength lower than plain)
Long steel 0.5%	0.012 (FRC strength lower than plain)	Slender and long polymeric 0.5%	5.6E-6 (FRC strength lower than plain)
Long Steel 1.0%	0.056	Slender and long polymeric 1.0%	9.4E-5 (FRC strength lower than plain)

Note: P value less than 0.05 indicates the properties are not the same.
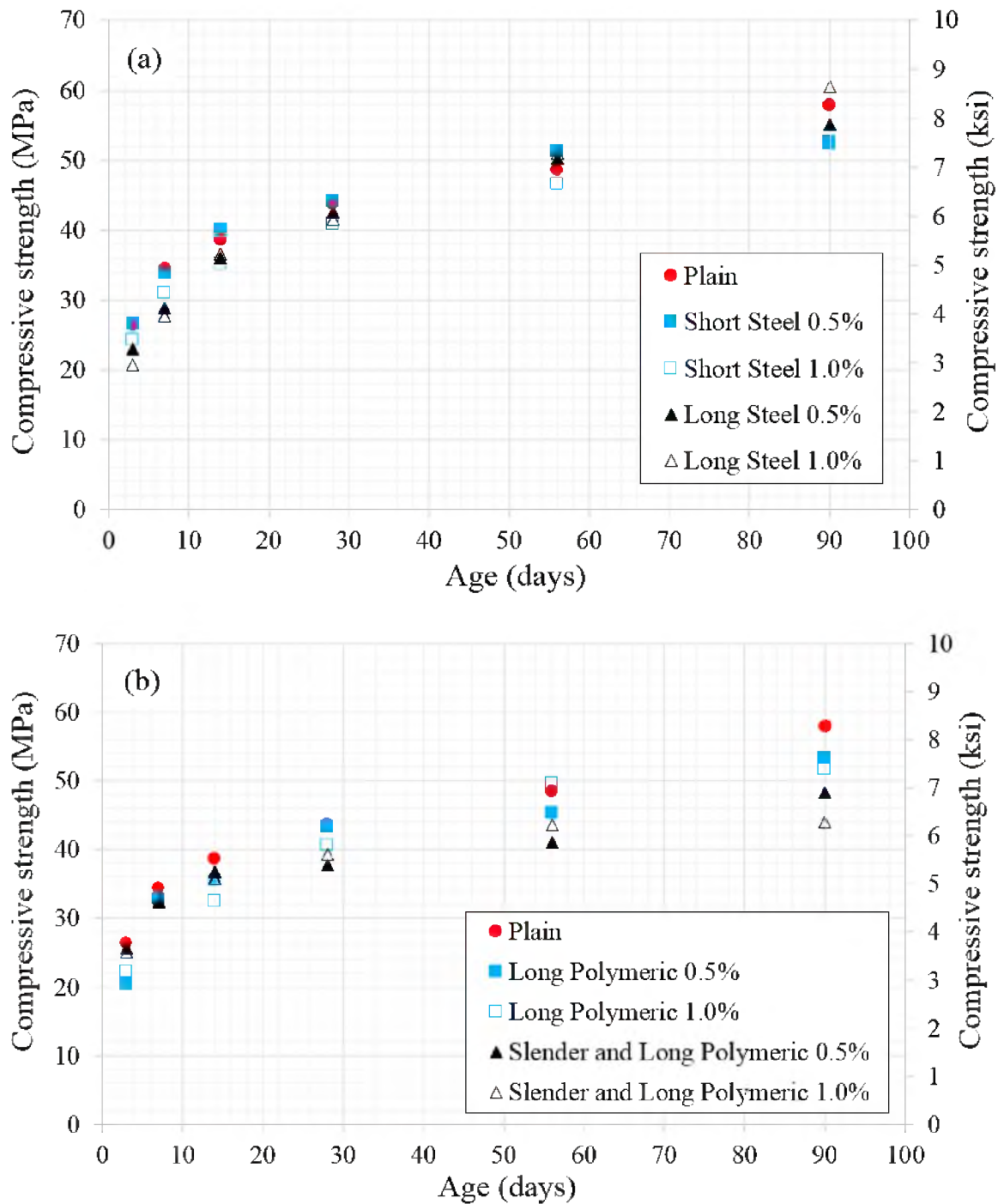
Figure 3.3. Effect of fibers on compressive strength values for (a) SFRC and (b) PFRC.

3.5.2 Free Drying Shrinkage

Table 3.4 shows the P values between measured free shrinkage of plain concrete versus shrinkage of each fiber-reinforced concrete mixture. Figure 3.4(a) and (b) show the measured free drying shrinkage from 3 to 90 days for SFRC and PFRC mixtures, respectively. The addition of fibers was again confirmed to not substantially change the free drying shrinkage, regardless of fiber type. Namely, SFRC showed same or lower free drying shrinkage, and PFRC showed same or higher shrinkage than that of plain concrete.

3.5.3 Coefficient of Thermal Expansion

Figure 3.5 shows the measured coefficient of thermal expansion (CTE) of one cylinder sample for each mixture at 1% volume fraction. No statistical analysis was performed on this data since there was only one sample of each mixture tested. Yet even with the limited sample data, the CTE appeared to exhibit negligible influence with a 1.0% volume fraction addition of each fiber type to the concrete.

Table 3.4. P values (two-tailed) between ε_{sh} of plain concrete versus ε_{sh} of each fiber reinforced concrete

Steel Fiber		Polymeric Fiber	
Type and contents (%)	P value	Type and contents (%)	P value
Short steel 0.5%	0.440	Long polymeric 0.5%	0.675
Short steel 1.0%	0.019 (lower than plain)	Long polymeric 1.0%	0.037 (higher than plain)
Long steel 0.5%	0.180	Slender and long polymeric 0.5%	0.793
Long Steel 1.0%	0.014 lower than plain)	Slender and long polymeric 1.0%	0.138

Note: P value less than 0.05 indicates the properties are not the same.
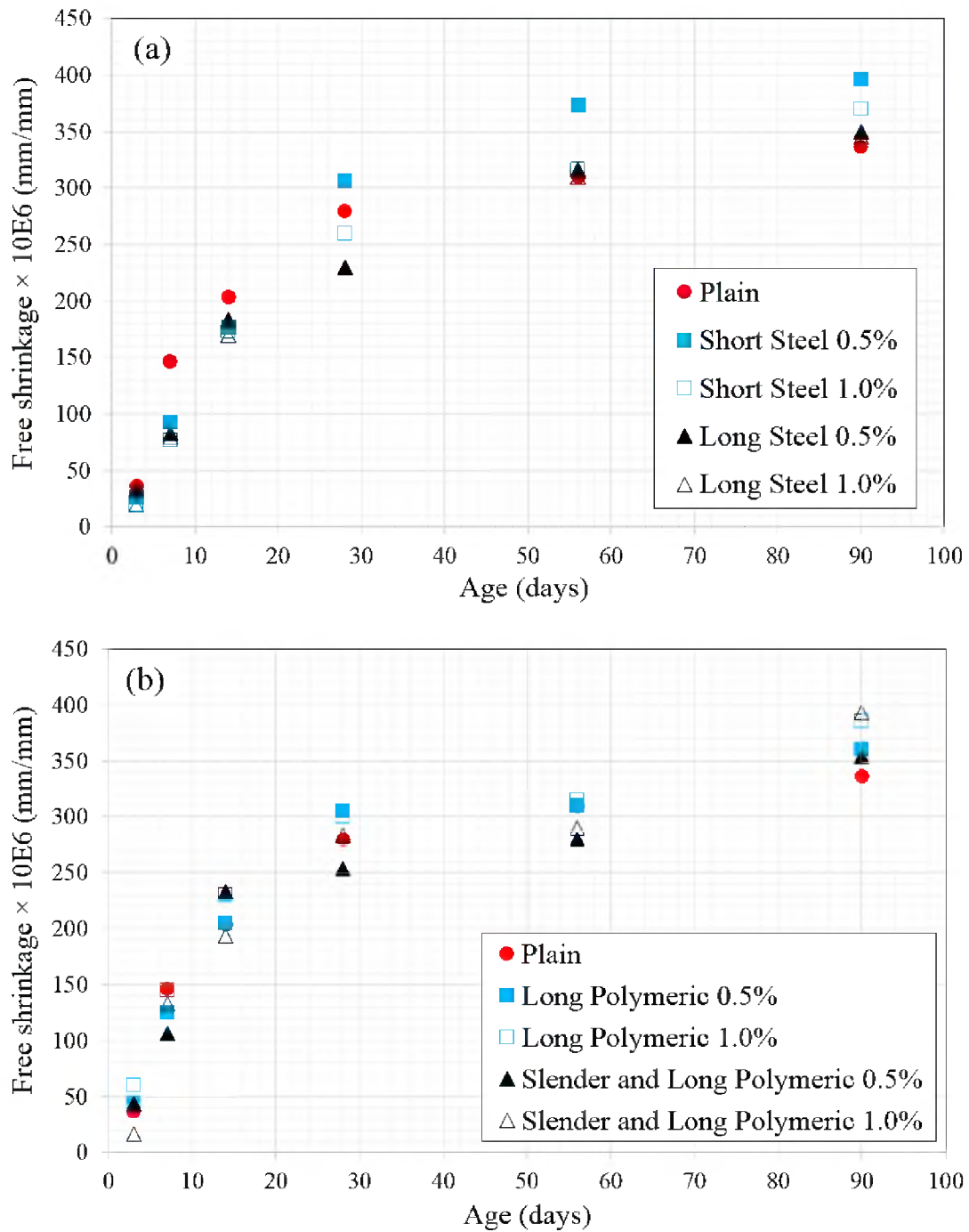
Figure 3.4. Effect of fibers on free drying shrinkage for (a) SFRC and (b) PFRC.
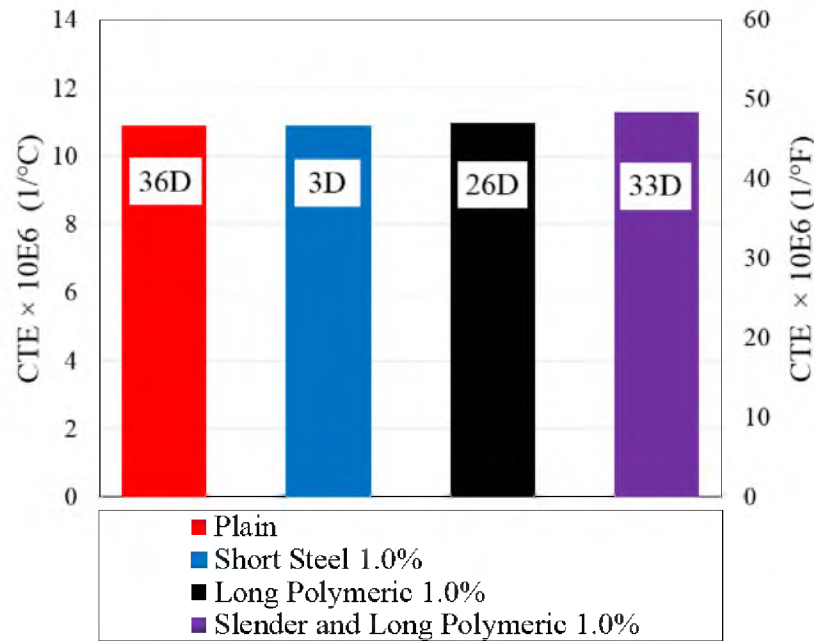
Figure 3.5. Effect of fibers on the coefficient of thermal expansion (showing age of cylinder during test).

3.5.4 Flexural Strength

Figure 3.6 (a) and (b) show the flexural load versus deflection curves of short steel FRC with 1.0% V_f between 3 and 90 days. And Figure 3.7 (a) and (b) show the flexural load versus deflection curves of slender and long polymeric fiber with 1.0% V_f between 3 and 90 days. The SFRC at 1% V_f undergoes a deflection-hardening response, while many of the PFRC samples and 0.5% SFRC samples exhibited deflection-softening responses. As mentioned previously, stresses (f_1, f_2 or f_{max}, and $f_{L/150}$) at different points along the load versus deflection curve were recorded. Comparisons of the addition of fibers to the measured flexural properties are indicated in the following sections. Figure 3.8 shows the fiber effect on the first cracking stress for both deflection hardening and deflection softening FRC. As shown in Table 3.5, there is no statistically significant difference (with 95% confidence) compared to the plain concrete.
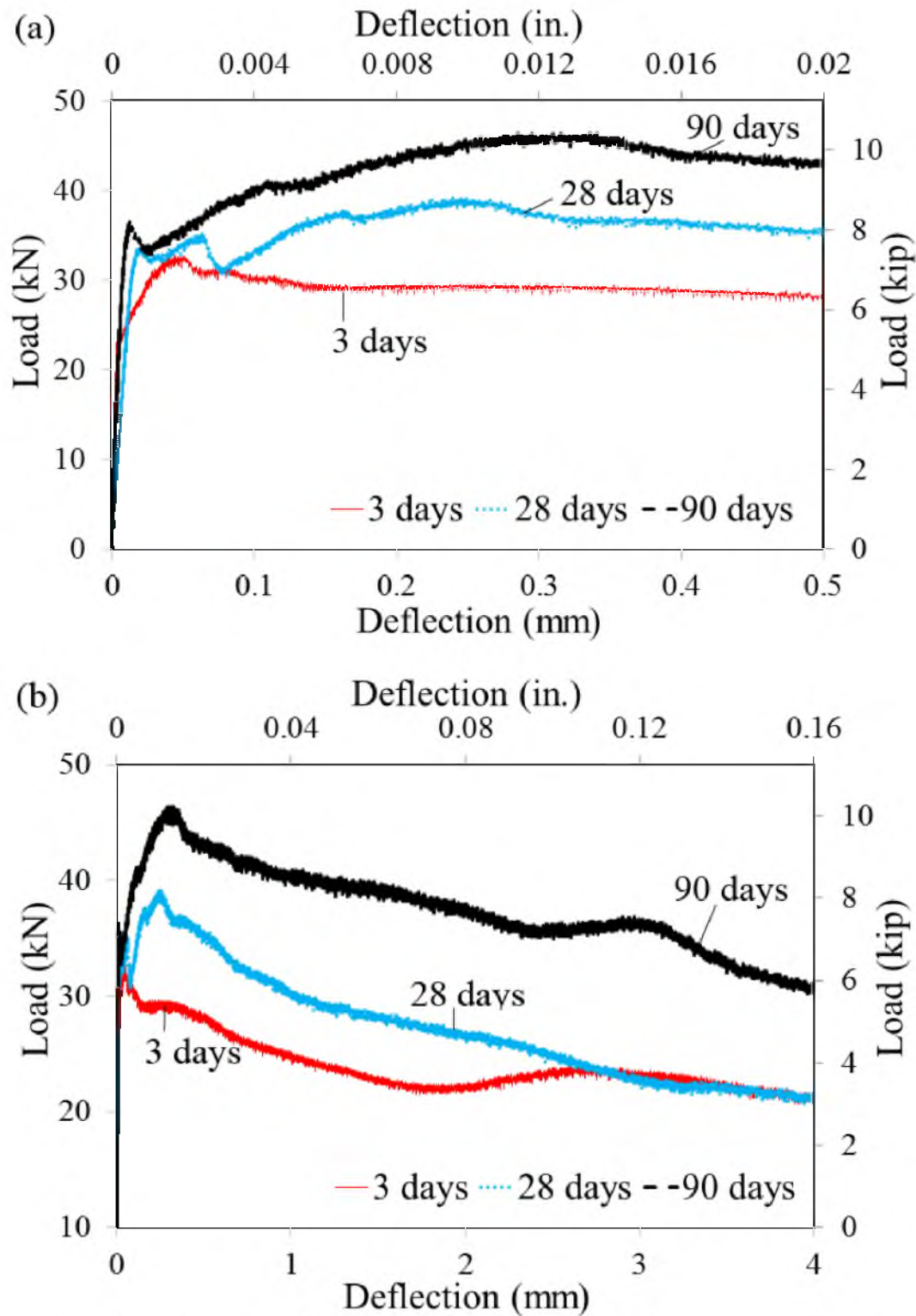
Figure 3.6. Typical load versus deflection of a beam containing short steel FRC 1.0% volume fraction (a) small deflection test range and (b) full deflection test range.
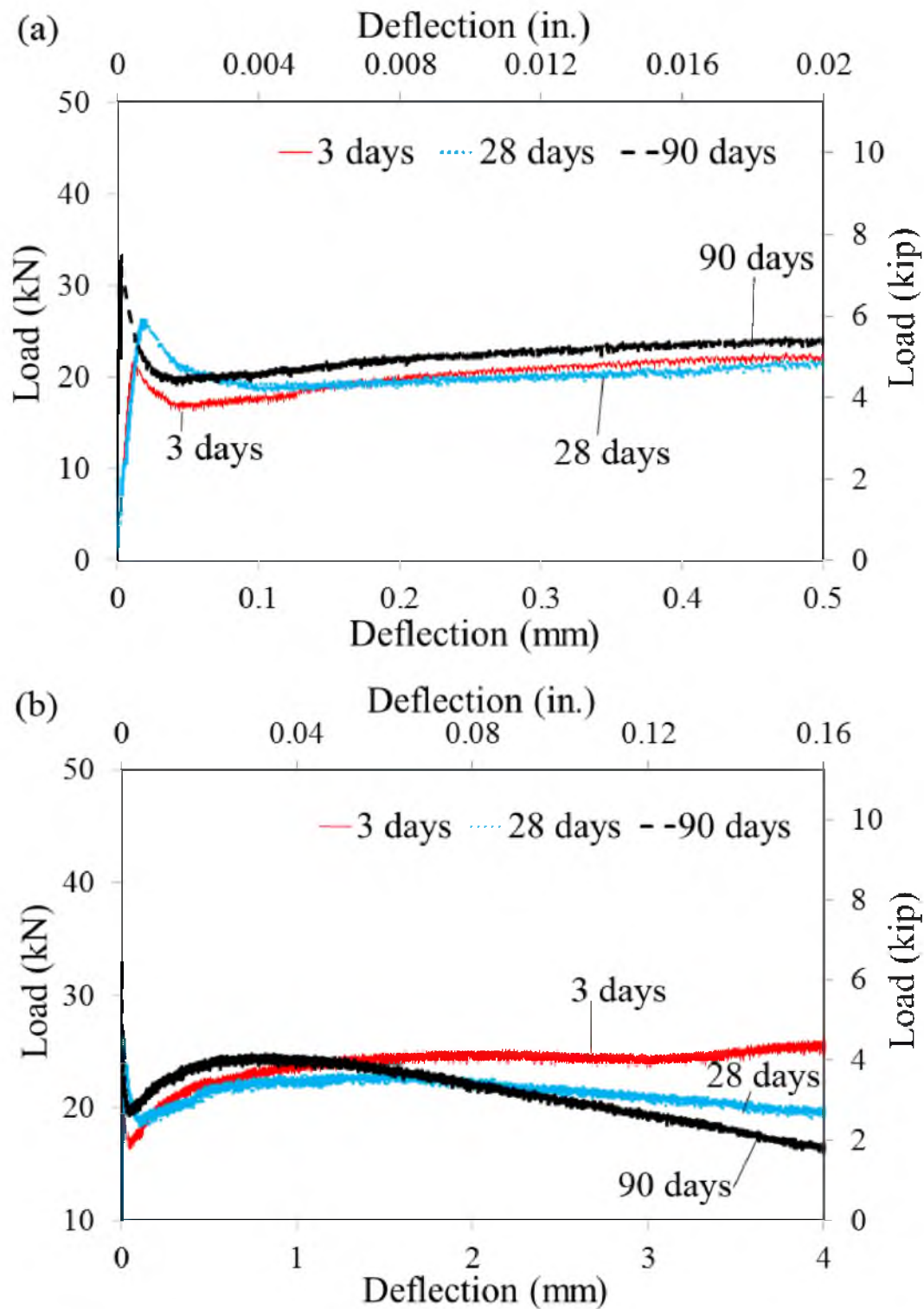
Figure 3.7. Typical load versus deflection of a beam containing slender and long polymeric FRC 1.0% volume fraction (a) small deflection test range and (b) full deflection test range.
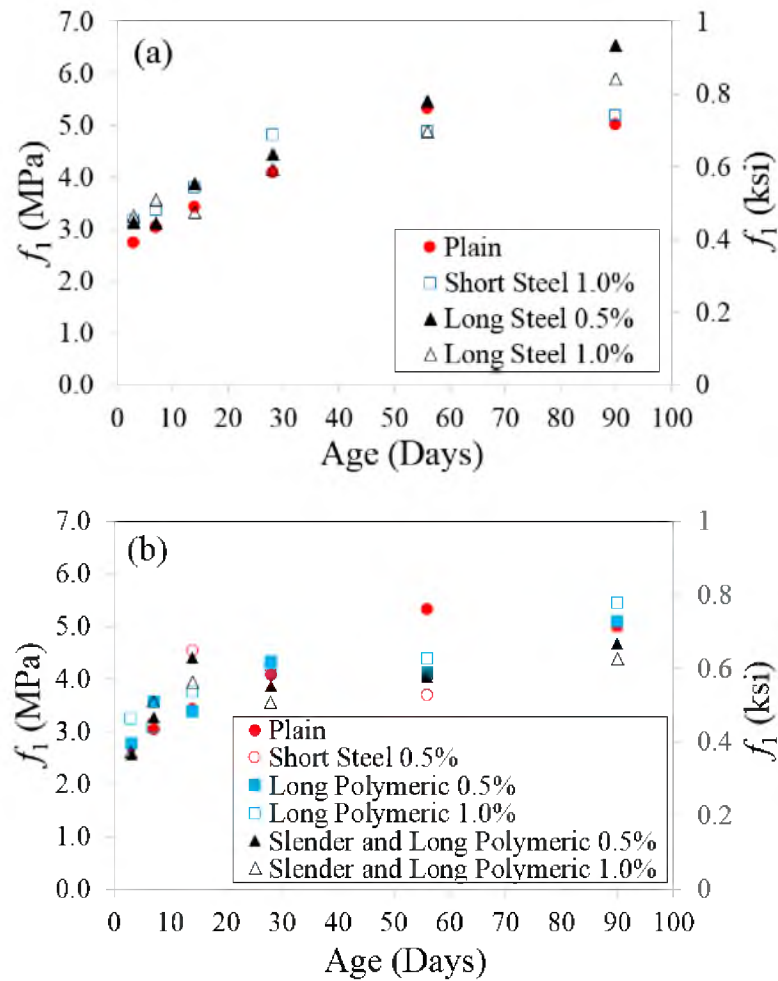
Figure 3.8. Effect of fibers on first peak cracking stress for (a) deflection-hardening FRC and (b) deflection-softening FRC.

Table 3.5 P values (two-tailed) between f1 of plain concrete versus f1 of each fiber-reinforced concrete

Steel Fiber		Polymeric Fiber	
Type and contents (%)	P value	Type and contents (%)	P value
Short steel 0.5%	0.939	Long polymeric 0.5%	0.943
Short steel 1.0%	0.076	Long polymeric 1.0%	0.440
Long steel 0.5%	0.041 (Higher than plain)	Slender and long polymeric 0.5%	0.889
Long Steel 1.0%	0.152	Slender and long polymeric 1.0%	0.524

Note: P value less than 0.05 indicates the properties are not the same.

If the highest stress value was used to describe the MOR in pavement design instead of the first-cracking stress, then the deflection-hardening samples (which is most of the SFRC mixtures) clearly would have a greater MOR value. Among deflection-softening samples (see Figure 3.9) (which is all of the PFRC and low volume fraction of SFRC), no clear trend can be seen between age and fiber type or fiber content on the secondary peak stress. A closer look at the measured property values reveals that the short steel FRC exhibited an increased f_{max} and $f_{L/150}$ as a function of age, while slender and long polymeric FRC does not show any trend in f_2 and $f_{L/150}$ with age.
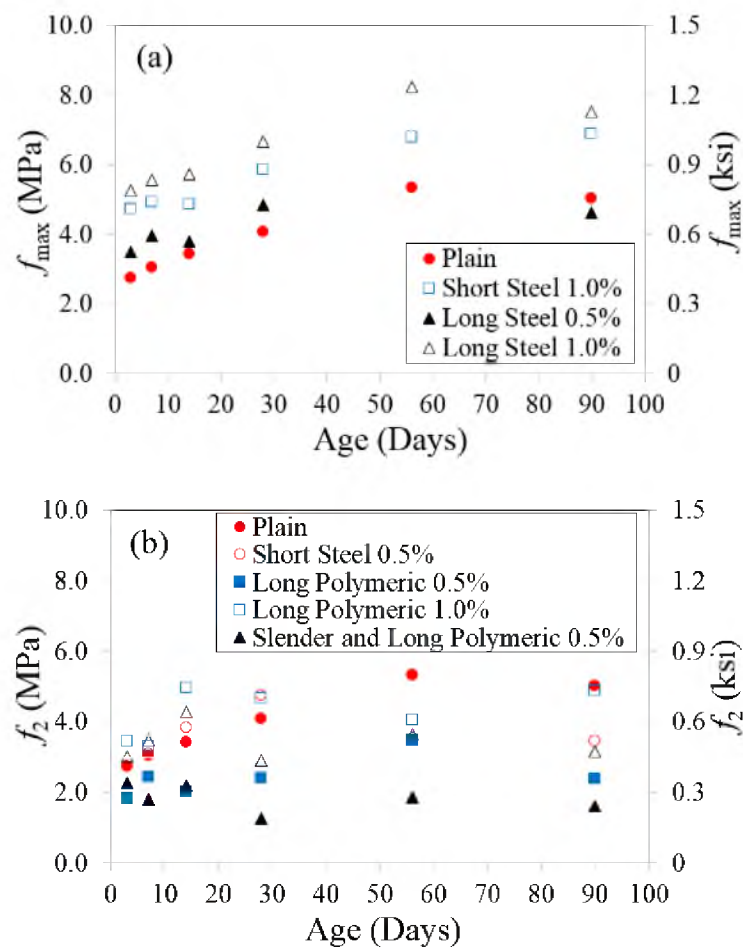
Figure 3.9. Effect of fibers on maximum peak (or second peak) stress for (a) deflection-hardening FRC and (b) deflection-softening FRC.

The effects of fiber volume fraction, fiber length, and fiber aspect ratio on f_{max} or f_2 were investigated. f_{max} or f_2 for all FRC mixtures were both increased as fiber volume fraction or fiber length increased. Those results are reasonable because increased effective bonding area from more fibers or longer embedment lengths are expected to improve both flexural performance and cracking resistance. A unique result compared to this expectation was that among the two PFRC mixtures, there was a decrease in the secondary peak f_2 as the aspect ratio increased. Although this was not explicitly studied, it is assumed that the higher mechanical friction of the long polymeric fibers in comparison to the smooth surface of the slender long polymeric fiber caused a higher pull-out resistance.

3.5.5 Residual Strength Ratio

Figures 3.10 (a) and (b) indicate the effects of fiber length and fiber aspect ratio on the ASTM residual strength ratio, respectively. And Figure 3.11 (a) and (b) show the effects of fiber volume content on the ASTM residual strength ratio.
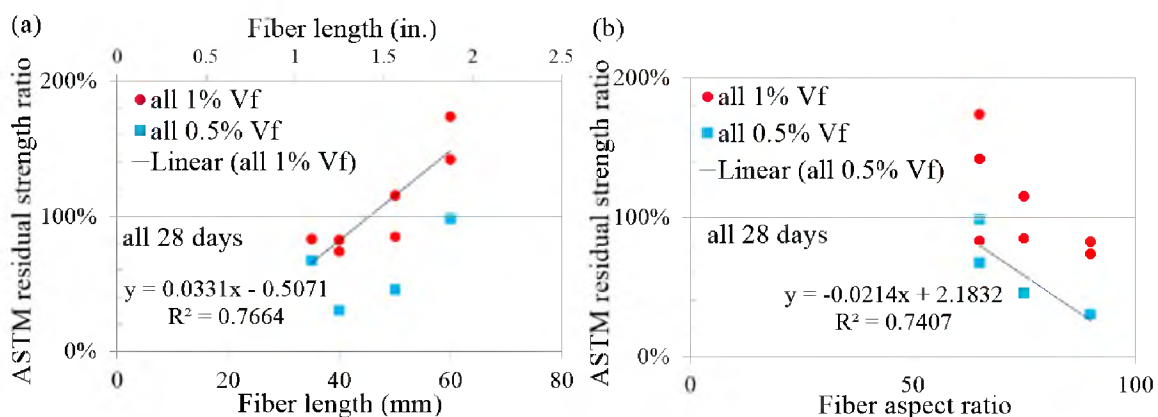
Figure 3.10. Effects of (a) fiber length and (b) fiber aspect ratio on ASTM residual strength ratio.
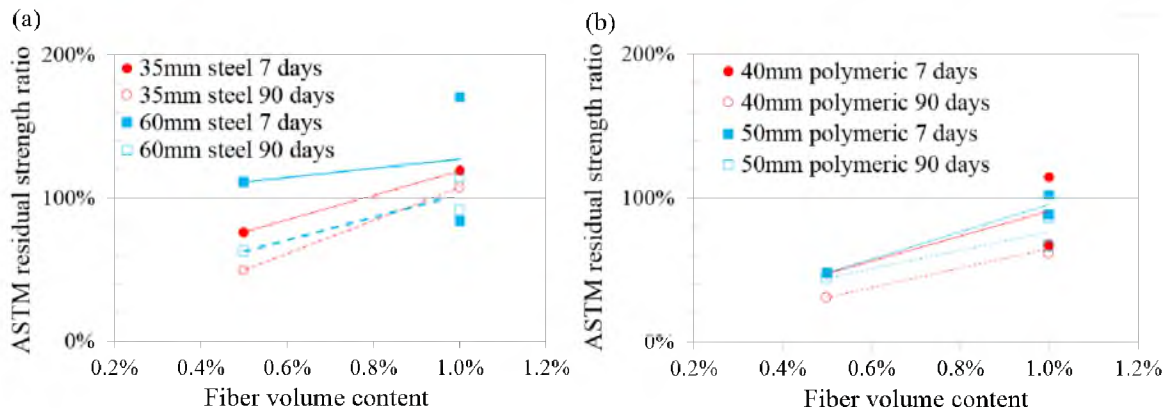
Figure 3.11. Effects of fiber volume content on ASTM residual strength ratio
(a) SFRC and (b) PFRC.

All FRC mixtures showed the increased residual strength ratio as the fiber length or the fiber volume fraction increased, as illustrated in Figure 3.10(a) and Figure 3.11. The more slender fibers with larger aspect ratios were found to have a decreased residual strength ratio as shown in Figure 3.10(b). As previously found, thinner fibers are more likely to fail before complete pull-out resistance is reached.

The trend found among the toughness values (see Figure 3.12) was that the deflection-hardening samples all had an increased $T_{L/150}$ as a function of age while deflection-softening samples exhibited no trend in $T_{L/150}$ versus age. In Figure 3.13 and 3.14, R_{150} from two different standards (ASTM C1609 or JCI-SF4) showed a constant or decreasing trend with age as expected.

Both the longer or more slender fibers of steel and polypropylene in FRC actually decreased in R_{150} as a function of age. This is unlike the expected result reported by other researchers indicating that long steel fibers in FRC will show a constant R_{150} with age (Bernard, 2015).
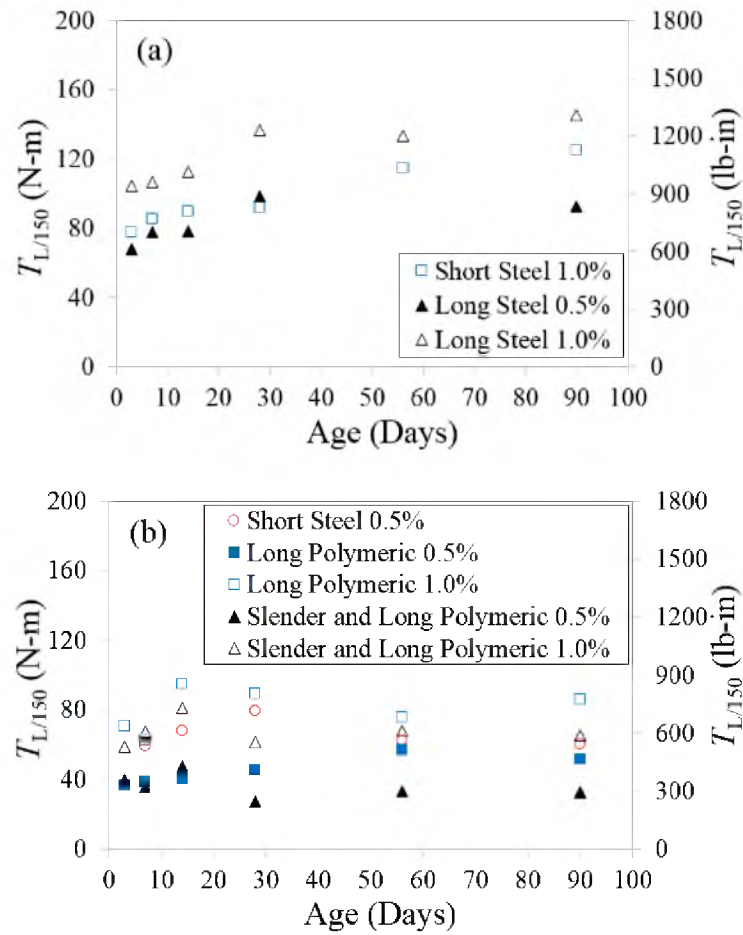
Figure 3.12. Effect of fibers on toughness for (a) deflection-hardening samples and (b) deflection-softening samples.
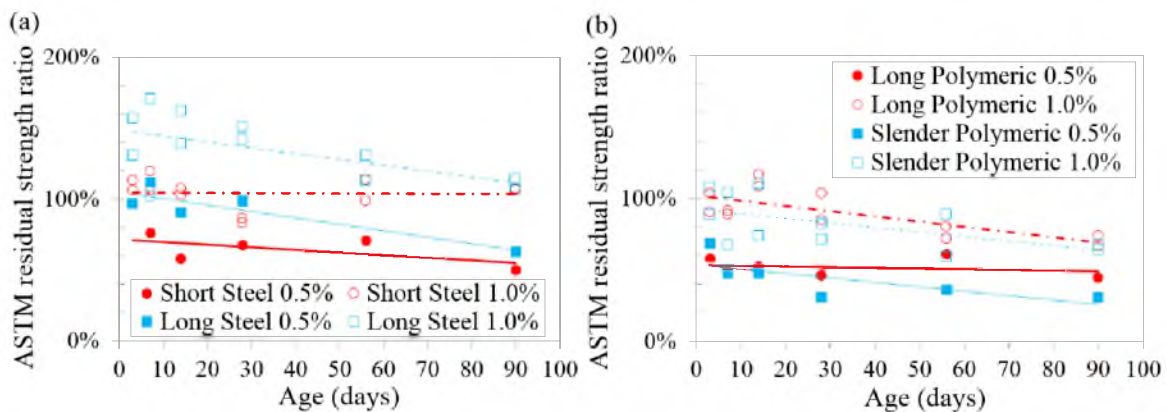
Figure 3.13. Effect of fibers on ASTM residual strength ratio for (a) SFRC and (b) PFRC.
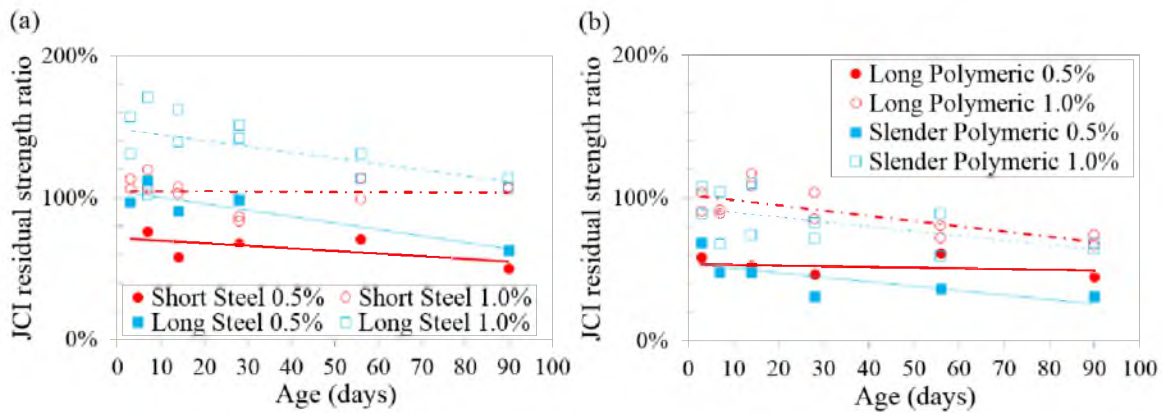
Figure 3.14. Effect of fibers on JCI residual strength ratio for (a) SFRC and (b) PFRC.

3.5.6 Fracture Energy

Figure 3.15 shows the effect of fiber on cut-off fracture energy, $G_{FRC,\ 2.5mm}$. It can be seen that the $G_{FRC,\ 2.5mm}$ for all FRC samples increased with age except for a relatively constant $G_{FRC,\ 2.5mm}$ with the slender and long polymeric fiber. The trend in increased $G_{FRC,\ 2.5mm}$ with age is in good agreement with findings by other researchers (Hodicky et al., 2013). Longer fibers, either steel or polymeric, had a higher rate of fracture energy increase with age, compared to shorter fibers.
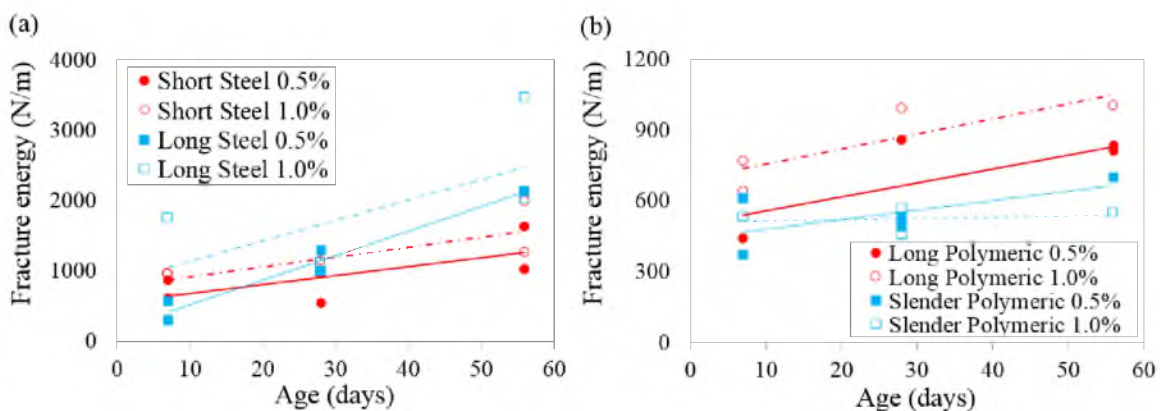
Figure 3.15. Effect of fibers on 2.5 mm cut-off fracture energy for (a) SFRC and (b) PFRC.

The constant fracture energy versus age seen with the slender polymeric fiber may be unexpected, except that other research studies have also indicated a possible decrease in the fracture energy with age for this same fiber type (Bordelon, 2007). The cause of this reduced or constant fracture energy among the one slender polymeric fiber is not known at this time.

3.6 Summary and Findings

This chapter aimed to investigate the age-dependent changes in flexural and fracture properties of FRC. Four different macrofibers with different volume contents (0%, 0.5%, and 1.0%) were selected and investigated for this study. The four fiber types studied were short steel hooked, long steel hooked, long polymeric, and slender and long polymeric fibers. Specific findings of the fiber type and fiber properties versus age are as follows:

- All FRC specimens showed the same or decreased residual strength ratios with age. Slender polymeric fiber with 0.5% of volume content showed the 69% reduction in residual strength ratio with age, while short steel fiber with 1.0% of volume content exhibited the constant residual strength ratio with age.

- All FRC mixtures except for those containing the slender polymeric fiber showed the increased fracture energy. When fracture occurs at later ages, steel FRC exhibited 2-4 times higher fracture energies than polymeric FRC.

- Of the deflection-hardening flexural response FRC mixtures, the postcracking flexural stresses carried by the FRC were 33% increased with age, despite the approximately 30% of reduced residual strength ratios with age.

- Of the deflection-softening flexural response FRC, the postcracking second peak

stress and toughness did not show any trends with age. First cracking stresses were increased by 75%, despite the 38% of reduced residual strength ratios with age.

- The compressive strength, free drying shrinkage, and coefficient of thermal expansion were all verified to have negligible affects when fibers were added to the concrete.

3.7 References

AASHTO, *AASHTO Guide for Design of Pavement Structures*, AASHTO, 1993.

ASTM Standard C157, Standard Test Method for Length Change of Hardened Hydraulic-Cement, Mortar, and Concrete. ASTM C157/C157M-04, West Conshohocken Pennsylvania: 2004.

ASTM Standard C1609, Standard Test Method for Flexural Performance of Fiber Reinforced Concrete (Using Beam with Third-point Loading). ASTM C1609/C1609M-05, West Conshohocken Pennsylvania: 2007.

ASTM Standard C39, Standard Test Method for Compressive Strength of Cylindrical Concrete Specimens. ASTM C39/C39M-05, West Conshohocken Pennsylvania: 2007.

Bernard, E. S. Age-Dependent Changes in Post-Crack Performance of Fibre Reinforced Shotcrete Linings. *Tunnelling and Underground Space Technology* **2015**, *49*, 241-248.

Bordelon, A. Fracture Behavior of Concrete Materials for Rigid Pavement Systems. MS Thesis, University of Illinois at Urbana-Champaign, Urbana, IL, 2007.

Brühwiler, E.; Wittmann, F. The Wedge Splitting Test, A New Method of Performing Stable Fracture Mechanics Tests. *Engineering Fracture Mechanics* **1990**, *35(1)*, 117-125.

Hodicky, K.; Hulin, T.; Schmidt, J. W. Wedge Splitting Test on Fracture Behaviour of Fiber Reinforced and Regular High Performance Concretes. *13th International Concrete on Fracture* **2013**.

JCI-SF 4, JCI Standards for Test Methods of Fiber Reinforced Concrete. Japan Concrete Institute: 1984.

Kim, D. j.; Naaman, A. E.; El-Tawil, S. Comparative Flexural Behavior of Four Fiber Reinforced Cementitious Composites. *Cement and Concrete Composites* **2008**, *30(10)*, 917-928.

Mobasher, B.; Bakhshi, M.; Barsby, C. Backcalculation of Residual Tensile Strength of Regular and High Performance Fiber Reinforced Concrete from Flexural Tests. *Construction and Building Materials* **2014**, *70*, 243-253.

Naaman, A.; Reinhardt, H. Proposed Classification of HPFRC Composites Based on Their Tensile Response. *Materials and Structures* **2006**, *39(5)*, 547-555.

CHAPTER 4

CRACK WIDTH PREDICTION EQUATION FOR FRC OVERLAYS

SUBJECTED TO TEMPERATURE GRADIENTS

4.1 Introduction

This chapter explains the modified theoretical equation for predicting the crack width of thin FRC overlays. These predicted crack widths are validated against field project data of a 50 mm (2 in.) constant slab thickness and constant FRC mixture. The field project had different joint spacings from 1.12 to 3.35 m (4 to 11 ft.) and all constructed slabs were subjected to only environmental loading, rather than traffic loading. One proposed crack width prediction equation based on temperature loading and properties of the mixture at a given age was modified to either include the fiber aspect ratio or the residual strength ratio of the FRC.

4.2 Field Project for Validation

Measurements from a previously constructed full-scale 50 mm thin FRC pavement (Bordelon and Roesler, 2011), as shown in Figure 4.1, were utilized for this study to validate the modified crack width prediction equation. The field overlay pavement was constructed in Rantoul, Illinois, which does exhibit significant temperature and humidity fluctuations throughout the year.

Figure 4.1. Constructed full-scale thin FRC overlay, view of section 1.

This full-scale experiment has only been subjected to environmental loading at the time of this research. No traffic loads have been applied to this pavement since casting. This condition allows us to modify Darter and Barenberg's equation (See Eq. 2.1), which was originally developed to predict joint opening of jointed plain concrete pavement (and also does not consider traffic load). The pavement mixture contained a hybrid of fibers: a 40 mm-long polypropylene-polyethylene-blended slender and long structural macrofiber (L_f/D_f = 90) and a 6 mm-long polypropylene microfiber (L_f/D_f = 300), at 0.48 and 0.06 percent V_f, respectively. The mixture contained a high cementitious content of 417 kg/m^3 for better mixing of FRC. The FRC overlay was roughly 50 mm (2 in.) thick, constructed

on a milled, aged, hot mixed asphalt (HMA) pavement, and cut at three difference slab sizes, as illustrated in Figure 4.2. For the full-scale project, mixed fiber-reinforced concrete was spread out with shovels and rakes. A vibratory screed was also used to strike-off and consolidate the pavement surface. Although some fiber clumping occurred primarily from server batches, these visible fibers were completely removed before final finishing (Bordelon, 2007).

Figure 4.3(a) shows the recorded free drying shrinkage values for samples cast in the field, but measured in a controlled 50% RH and 22 °C environment. Figure 4.3(b) and Figure 4.3(c) show the ambient air temperature and measured temperatures from thermocouples installed at the top and bottom of the FRC slab. Based on this measurement, the monthly extreme air temperature gradient $\Delta T = 17.6$ °C will be used to estimate crack width in the prediction equation. The temperature difference from the top to the bottom of the FRC slab at any given time of day was around $\Delta T = 2$ °C for nighttime, as will be an input for determining thermal loading in the finite element model. Developed finite element model will be introduced in Chapter 6.

		Section 1	Section 2	Section 3
Length (m)		1.12	1.68	3.35
Width (m)		1.15	1.73	1.72
Thickness (m)		0.05	0.05	0.05

Section 1	Section 2	Section 3
FRC, t = 50 mm	FRC , t = 50 mm	FRC, t = 50 mm
HMA, t = 50 mm	HMA, t = 50 mm	HMA, t = 50 mm
Binder course, t = 370 mm	Binder course, t = 370 mm.	Binder course, t = 200 mm
Lime modified Subgrade, t = 300 mm	Lime modified Subgrade, t = 300 mm	Lime modified Subgrade, t = 300 mm
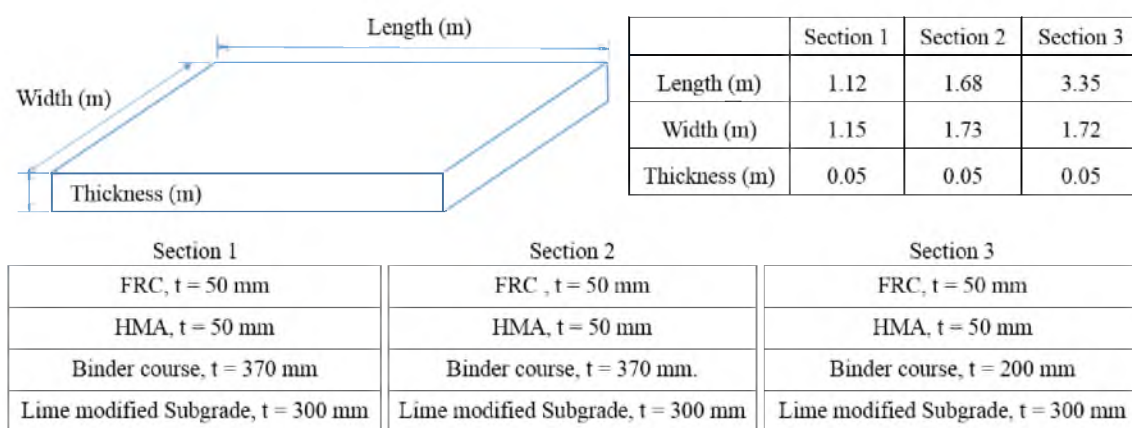
Figure 4.2. Field project saw-cut slab sizes and pavement layer information.
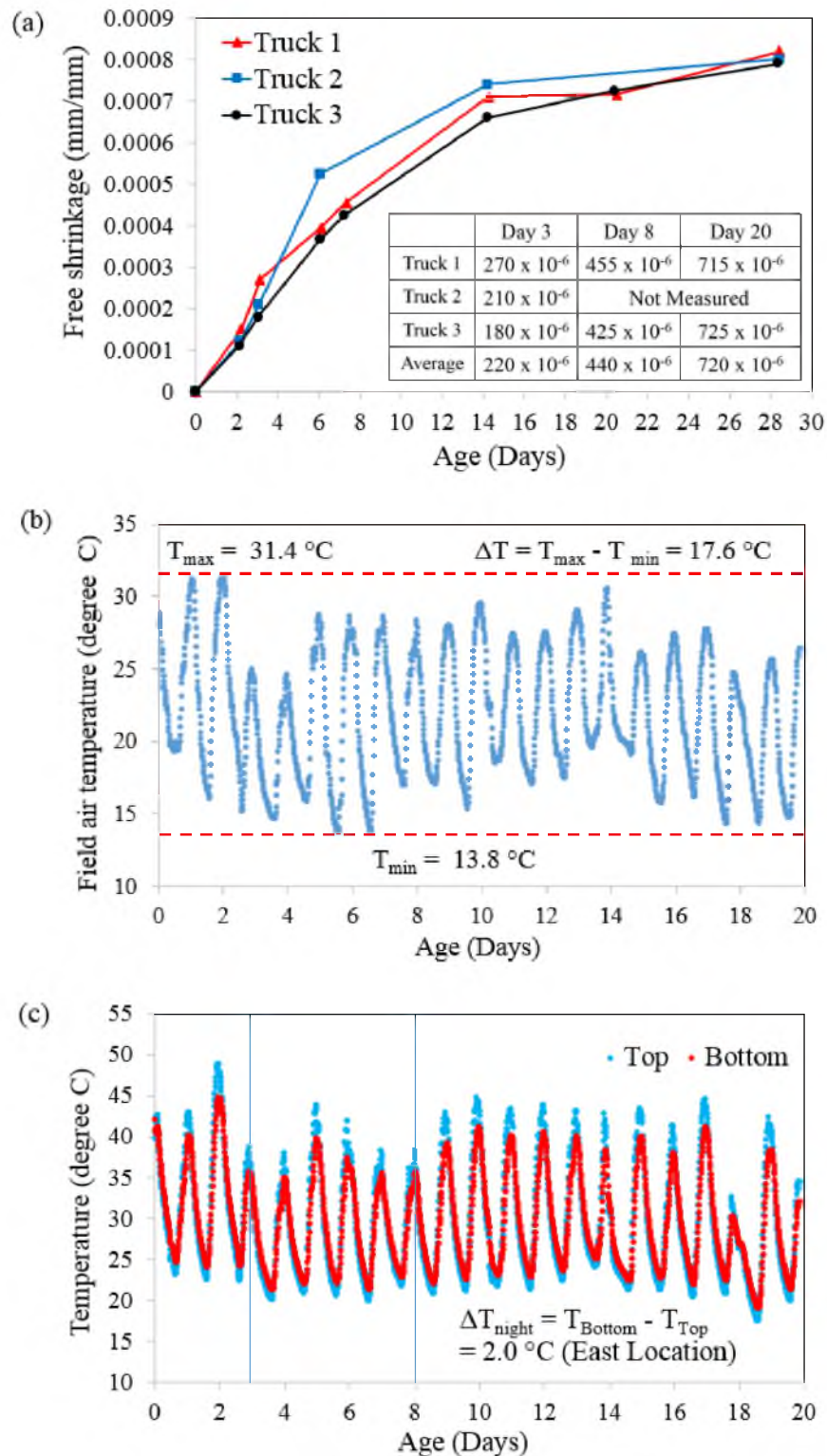
Figure 4.3. Measured free drying shrinkage and temperature (a) measured free drying shrinkage of concrete prisms collected from different truck batches on the day of construction; (b) measured field air temperature; (c) measured temperature differentials between top and bottom of FRC slab.

Table 4.1 shows the reported (Bordelon and Roesler, 2011) lab-cast flexural and fracture specimen properties of the FRC mixture. According to the field data source, the flexural strength f_1, residual strength $f_{L/150}$, and residual strength ratio R_{150} were all determined according to ASTM C1609 (2007). Two different sizes of beam (75 or 150 mm deep) were tested at 7 and 28 days for flexural properties of FRC. The split-tensile strength of the FRC $f_{t,FRC}$ was measured according to ASTM C496 (2004). The fracture properties G_f, G_{FRC}, and $CTOD_c$ of FRC were all determined based on the results of a single-edge notched beam (SEN[B]) test. The test was carried out according to the Two Parameter model (Jenq and Shah, 1986) and Hillerborg method (1985). Debonding was investigated in the field project at roughly 3 months after construction using a chain drag and in situ torsional test at specific cored locations. Based on these investigations, it was estimated that the potential for debonding was high for large portions of section 1, which counterintuitively had the smallest joint spacing. A torsional test on a limited number of samples (4 cores) was found highly variable, yet the average bond strength was estimated to be 400 N-m between FRC and HMA after 75 days age. The cracked joint spacing and crack widths were visually measured at 3, 8, and 20 days after construction.

Table 4.1 Flexural and fracture properties of FRC

Age	Flexural						Tensile	Fracture		
	7.5 × 7.5 cm beam			15 × 15 cm beam			$\phi 10 \times 20$ cm	15 × 8 × 70 cm SEN[B]		
	f_1	$f_{L/150}$	R_{75}	f_1	$f_{L/150}$	R_{150}	$f_{t,FRC}$	G_f	G_{FRC}	$CTOD_c$
(days)	(MPa)	(MPa)	(%)	(MPa)	(MPa)	(%)	(MPa)	(N/m)	(N/m)	(mm)
7	4.49	2.19	48.8	3.78	1.80	47.6	3.49	63.2	3691	0.026
28	4.77	2.12	44.4	5.02	1.41	28.0	4.25	52.8	3175	0.019

A crack comparator card was used to visually interpret the crack widths. Figure 4.4 shows the relationship between measured average cracked-joint spacing versus age and measured average crack width versus age, respectively. An important finding here was that only the joints cracked; there were no mid-panel cracks in the FRC overlay slabs. The larger slabs, representing the greatest average crack spacing, also had the largest crack widths, as expected.
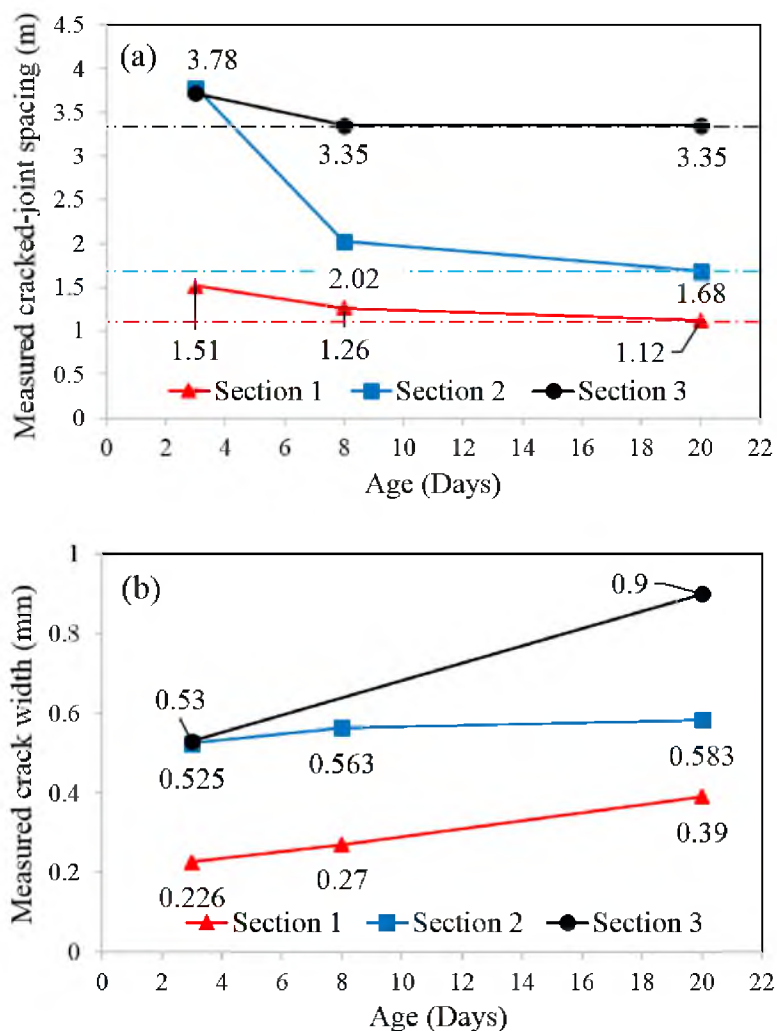
Figure 4.4. Cracked-joint spacing and crack width at different measured ages of the field FRC overlays (a) measured cracked-joint spacing versus age; (b) measured average crack width versus age.

Not all joints were found to have cracked after the first temperature cycle at the earliest ages, despite an exhibited 10 °C of air temperature differential in the first day. Still, cracks that formed at 1 day remained the largest at later ages, a phenomenon also seen by McCullough and Dossey (1999).

4.3 Crack Width Prediction Equation

As previously introduced, Eq. (2.1) is currently adopted for the design of JPCP, and was originally proposed by Darter and Barenberg (AASHTO 1993; Darter and Barenberg, 1977). Although this is used for all types of JPCP design today, fundamentally Eq. (2.1) may not be valid for dowelled or other reinforced concrete pavements because it does not consider the influence of reinforcement across joints. Also, as described previously, the RILEM/CNR structural design used a modification factor for crack widths to be predicted in structures with steel-fiber reinforcement (RILEM TC162-TDF, 2000). This RILEM/CNR modification factor is a reduction term based on the aspect ratio of ($50D_f/L_f$), which only considers the influence of the aspect ratio of steel fibers. It does not consider the fiber content or other properties of fiber. Several researchers suggested a modification factor proportional to the residual strength ratio, which is expected to be more accurate for alternative fiber types regardless of fiber material, volume fraction, or aspect ratio (Carlswärd, 2006; Jansson et al., 2010; Löfgren, 2007).

To develop a prediction equation for the crack width of FRC overlay, Eq. (2.1) was modified to consider fiber aspect ratio from Eq. (2.4) or residual strength ratio of FRC from Eq. (2.7). Thus, the cracked joint opening width of an FRC overlay can be expressed as Eq. (4.1).

$$w = Cs(\alpha_t \Delta T + \Delta \varepsilon_{sh})\{k_a \ or \ k_b\} \tag{4.1}$$

$$\Delta \varepsilon_{sh} = \varepsilon_{sh,free} - \varepsilon_{sh,restrained} \tag{4.2}$$

$$k_a = \frac{50}{L_f/D_f} \leq 1.0 \ or \ k_b = 1 - \frac{f_{residual}}{f_{mor}} \tag{4.3}$$

Note that both k_a and k_b are coefficients which express the positive fiber effect to reduce crack opening widths, and they were originally derived in previous studies (Jansson et al., 2010; RILEM TC-162 TDF, 2000). The measured free drying shrinkage at a specific age and temperature from the field investigation were applied to the crack width prediction. k_a was determined with using aspect ratio of incorporated macro-fiber and k_b was determined using the measured residual strength ratio of a 75 mm beam as shown in Table 4.1.

4.4 Comparison of Prediction Equation

Tables 4.2 and 4.3 show the calculated crack widths for each section using Eqs. (4.1) to (4.3), compared to measured crack widths from field and lab testing. The crack widths in Table 4.2 were calculated using the initial joint spacing, fixed for all ages as being the crack spacing. Otherwise, crack widths in Table 4.3 were calculated using the actual measured cracked-joint spacing shown in Figure 4.4(a) for each age. As expected, calculated crack widths with adjusted joint spacing show better prediction than crack widths with fixed joint spacing. These values in Table 4.3 with the actual average crack spacing were found to predict crack widths within ±25% or 0.18 mm of the actual measured field crack widths for the thin FRC slabs.

Table 4.2 Actual field and calculated crack width with fixed joint spacing

Age (days)	Section 1 (1.12 m long)			Section 2 (1.68 m long)			Section 3 (3.35 m long)		
	Crack width (mm) with fixed joint spacing								
	Actual	k_a	k_b	Actual	k_a	k_b	Actual	k_a	k_b
3	0.226	0.160 [-29%]	NA	0.525	0.240 [-54%]	NA	0.530	0.479 [-10%]	NA
8	0.270	0.249 [-8%]	0.230 [-15%]	0.563	0.374 [-34%]	0.344 [-39%]	NA	0.745	0.687
20	0.390	0.362 [-7%]	0.332 [-15%]	0.583	0.544 [-7%]	0.499 [-14%]	0.900	1.084 [+20%]	0.997 [+11%]

Note: values in brackets indicate either +% overpredicted crack or -% underpredicted crack widths

Table 4.3 Actual field and calculated crack width with adjusted joint spacing

Age (days)	Section 1 (adjusted)			Section 2 (adjusted)			Section 3 (adjusted)		
	Crack width (mm) with adjusted joint spacing								
	Actual	k_a	k_b	Actual	k_a	k_b	Actual	k_a	k_b
3	0.226	0.216 [-4%]	NA	0.525	0.541 [+3%]	NA	0.530	0.532 [+0.3%]	NA
8	0.270	0.280 [+4%]	0.258 [-4%]	0.563	0.449 [-20%]	0.414 [-26%]	NA	0.745	0.687
20	0.390	0.362 [-7%]	0.344 [-12%]	0.583	0.544 [-7%]	0.526 [-10%]	0.900	1.084 [+20%]	0.997 [+11%]

Note: values in brackets indicate either +% overpredicted crack or -% underpredicted crack widths

The predicted crack widths while using k_a showed better agreements with measured field crack widths for section 1 and section 3. The calculated results using the residual strength ratio k_b generally were 7% lower in crack width than the results using the aspect ratio k_a. Figure 4.5 and Figure 4.6 show graphical representations of these comparisons of predicted crack widths to measured average crack widths from the field observation for saw-cut joint spacing versus actual crack spacing, respectively. For section 2 only, it can be seen that measured field crack width is closer to the predicted crack width based on k_b instead of k_a at 20 days age.
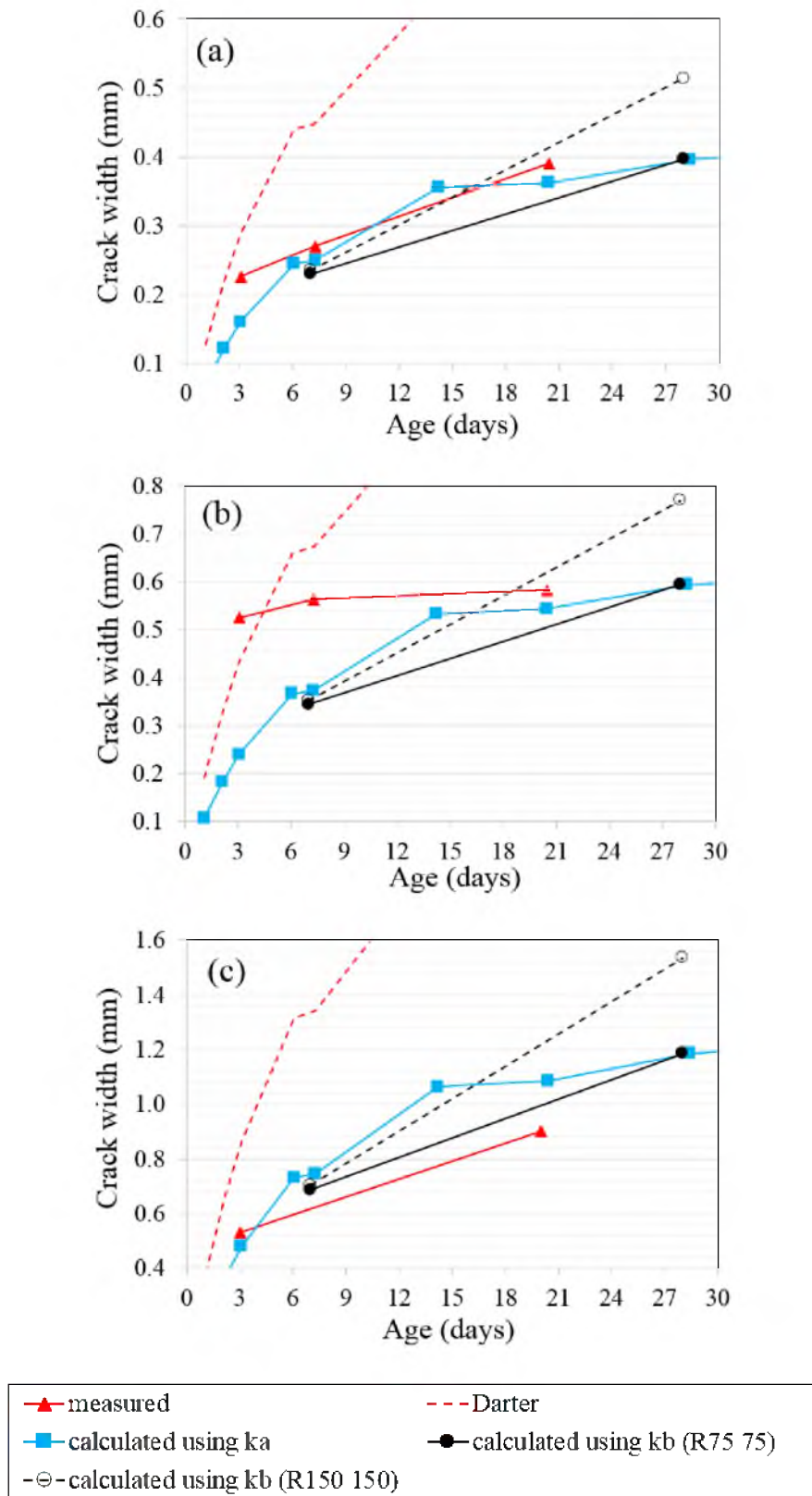
Figure 4.5. Comparison of calculated crack widths to measured actual crack widths using the constant saw-cut joint spacing of (a) section 1; (b) section 2; (c) section 3.
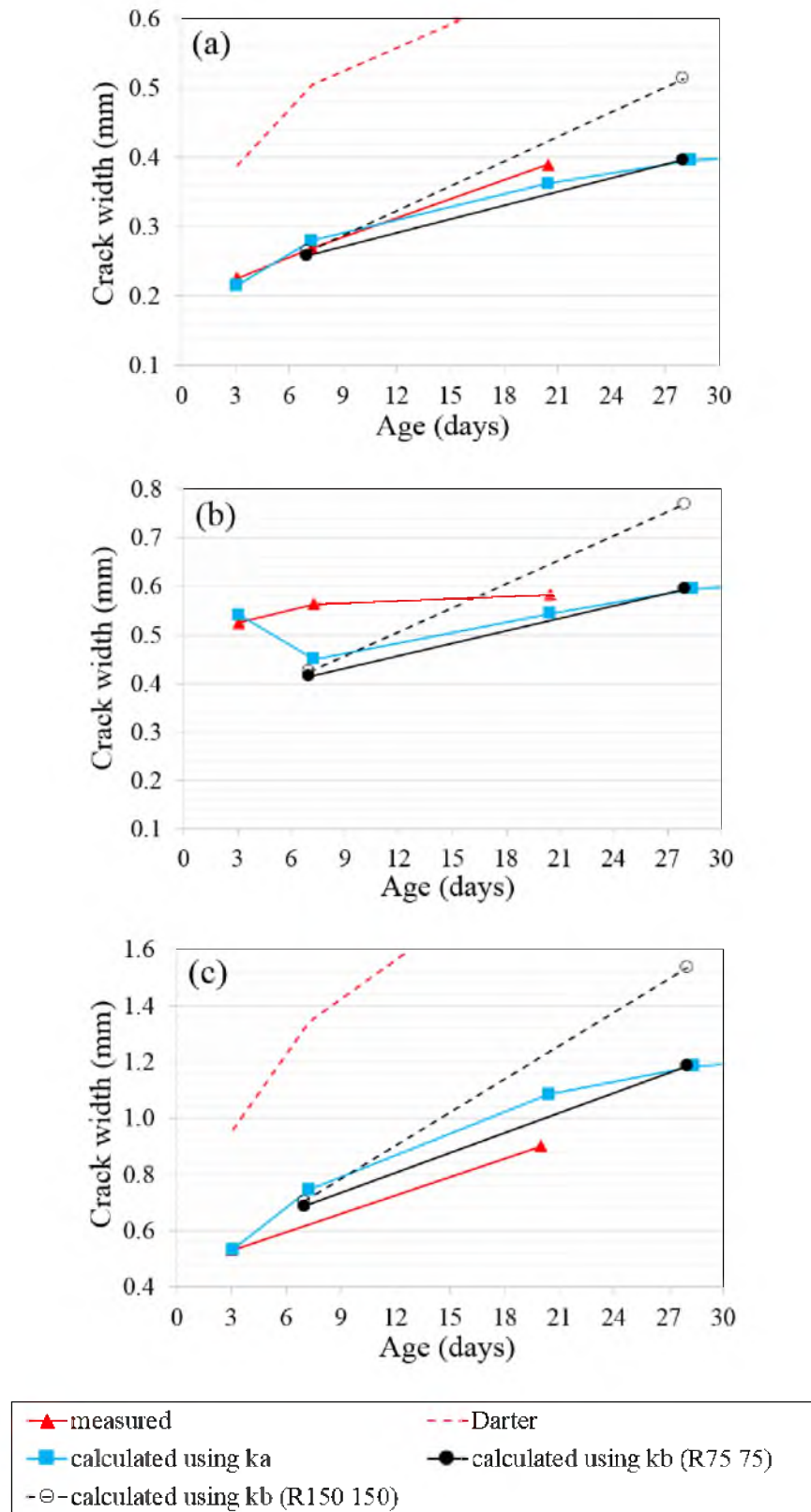
Figure 4.6. Comparison of calculated crack widths to measured actual crack widths using adjusted actual crack spacing from (a) section 1; (b) section 2; (c) section 3.

In this study, k_a showed the better crack width prediction compared to k_b. However, it cannot be concluded that k_a is more accurate than k_b based on this case study alone. This is because very limited field data were utilized to validate the predicted crack widths. In addition, k_a only considers fiber aspect ratio while k_b can consider more fiber properties, such as type and volume content. Thus, it is expected that k_b can give more accurate prediction than k_a, but further research needs to be conducted to verify this hypothesis.

Overall, it is restated here that the prediction equation Eq. (4.1) assumes the drying shrinkage and temperature differentials occur only in the FRC layer, and the equation does not consider traffic loading. Eq. (4.1) also does not account for possible constructed slab thickness variations or underlying HMA or base material stiffness or temperature changes on cracking. These assumptions and limitations may need to be accounted for the equation to be utilized for traffic-loaded FRC overlay designs. In this regard, further studies might be necessary to modify the proposed equation to consider traffic loading conditions, varying material stiffness properties, and age variation in FRC properties.

4.5 Summary and Findings

The research presents a modified equation to predict crack widths of a thin FRC overlay subjected to temperature gradients. The prediction equation is based on the Darter-Barenberg temperature and shrinkage-induced joint opening equation used for plain JPCP roads. The new prediction equation modifies this joint opening JPCP equation to consider the addition of fibers, either as a fiber aspect ratio or a measured residual strength ratio of the FRC. The proposed modified equation is able to predict the crack width within 0.19 mm (±25%) of that measured from a field-constructed 50 mm thin FRC overlay subjected

to only environmental loading. Further research is needed to determine whether the modified equation using fiber aspect ratio or residual strength ratio is more accurate for predicting crack widths for traffic-loaded FRC overlays, or FRC overlays containing a variety of other fiber types.

4.6 References

ASTM Standard C1609, Standard Test Method for Flexural Performance of Fiber Reinforced Concrete (Using Beam with Third-point Loading). ASTM C1609/C1609M-05, West Conshohocken Pennsylvania: 2007.

ASTM Standard C496, Standard Test Method for Splitting Tensile Strength of Cylindrical Concrete Specimens. ASTM C496/C496M-11, West Conshohocken Pennsylvania: 2004.

Bordelon, A.; Roesler, J. Flowable Fibrous Concrete for Thin Concrete Inlays. *Transportation and Development Institute Congress* **2011**, 874-883.

Carlswärd, J. Shrinkage Cracking of Steel Fibre Reinforced Self Compacting Concrete Overlays: Test Methods and Theoretical Modeling. Doctoral Thesis, Luleå University of Technology, Sweden, 2006.

Darter, M. I.; Barenberg E. J. Zero-Maintenance Design for Plain Jointed Concrete Pavements. Proceedings of the International Conference on Pavement Design, Purdue University, 1977.

Hillerborg, A. The Theoretical Basis of a Method to Determine the Fracture Energy G_F of Concrete. *Materials and Structures* **1985**, *18(4)*, 291-296.

Jansson, A.; Löfgren, I.; Gylltoft, K. Flexural Behaviour of Members with a Combination of Steel Fibres and Conventional Reinforcement. *Nordic Concrete Research* **2010**, *2(42)*, 155-171.

Jenq, Y.; Shah, S. P. Two Parameter Fracture model for concrete. *Journal of Engineering Mechanics* **1985**, *111(10)*, 1227-1241.

Löfgren, I. Calculation of Crack Width and Crack Spacing. *Nordic Mini Seminar: Fibre reinforced concrete, Trondheim, Norway* **2007**, 1-12.

McCullough, B.; Dossey, T. Considerations for High-Performance Concrete Paving: Recommendations from 20 years of Field Experience in Texas. *Transportation*

Research Record: Journal of the Transportation Research Board **1999**, *1684*, 17-24.

RILEM TC162-TDF, Test and Design Methods for Steel Fibre Reinforced Concrete: Bending Test. *Mater Struct*, **2000**, *33*, 3-5.

CHAPTER 5

FIBER EFFECT ON INTERFACIAL BOND BETWEEN CONCRETE

AND FIBER-REINFORCED MORTAR

5.1 Introduction

The bond performance between the old substrate and FRC overlay is commonly

assumed to not be affected by the addition of fibers, yet field studies (Chanvillard et al.,

1989; Delatte et al., 2000) indicate that curling and debonding is reduced with the addition

of fibers. Furthermore, the developed finite element model which will be introduced in

Chapter 6 showed the reduction in debonding length compared to plain concrete pavement.

Additional research was performed to determine whether there is any effect from adding

fibers in the new overlay concrete on the physical interfacial bond itself, besides just the

benefit of fibers to reduce crack widths and deflections from thermal loading. For this

chapter, experimental testing was performed to quantify the interfacial bond properties, as

between an aged concrete substrate and a new overlay of varying fiber types and volume

contents. Both tensile and shear bond strength at the interface between concrete and fiber-

reinforced mortar (FRM) are measured. The present chapter aims at identifying the

interfacial bond between an aged concrete substrate and a new overlay with common fiber

types and reasonable volume contents.

5.2 Experimental Investigation

5.2.1 Materials and Test Variables

Three different types of fibers (described in Table 5.1) and two different dosage rates for each fiber were considered in this study. The volume fraction dosage rates of the fibers were 0.40% and 0.78% for a slender and long polymeric fiber (Y1), 0.5% and 1.0% for a long polymeric fiber (Y2), and 1.0% and 2.0% for a short steel fiber (T). These fiber types and respective dosage rates were selected to represent the potential applications of slabs-on-ground, overlays, and bridge decks. The short steel fibers were expected to produce the highest tensile fracture resistance, and the long polymeric fibers were expected to have a slightly higher tensile performance than the slender and long polymeric fibers.

Table 5.1 Properties of fibers

Fiber Type	Slender and Long Polymeric (Y1)	Long Polymeric (Y2)	Short Steel (T)
Photo			
Material	Polypropylene-polyethylene	Polypropylene	Steel
Cross section	Rectangular	Rectangular	Circular
Length	40 mm (1.6 in.)	50 mm (2.0 in.)	33 mm (1.3 in.)
Diameter	-	-	0.55 mm (0.02 in.)
Thickness	0.105 mm (0.004 in.)	0.4 mm (0.016 in.)	-
Width	1.4 mm (0.06 in.)	1.2 mm (0.05 in.)	-
Aspect ratio	90	75	60
Specific gravity	0.92	0.91	7.85
Tensile strength	620 MPa (90 ksi)	550 MPa (80 ksi)	1300 MPa (189 ksi)
Modulus of elasticity	9.5 GPa (1378 ksi)	7.0 GPa (1015 ksi)	210 GPa (30458 ksi)

The mortar mixture proportions of those fiber materials are shown in Table 5.2. The mortar mixture was based on a FRM design with a reported good workability for higher fiber contents > 0.5% (Sevil et al., 2011). The original substrate material was made as a concrete with the mixture design listed in Table 5.2. This original substrate contained limestone coarse aggregates of 9 mm maximum aggregate size. All mixtures contained fine aggregates that were natural sand. The substrate concrete specimens were moist cured at a relative constant temperature of 30 °C (86 °F) for 28 days prior to the new overlay construction. All aged substrate samples were sandblasted prior to constructing the new overlay mortar.

Table 5.2 Mix design for substrate concrete and fiber-reinforced mortars

Material		Substrate Concrete	Control Mortar	Slender and Long Polymeric (Y1) Mortar	Long Polymeric (Y2) Mortar	Short Steel (T) Mortar
Water		187 kg/m^3 (315 pcy)	330 kg/m^3 (556 pcy)			
Type I/II Cement		468 kg/m^3 (788 pcy)	579 kg/m^3 (975 pcy)			
Coarse Aggregate		1052 kg/m^3 (1773 pcy)	0			
Fine Aggregate		857 kg/m^3 (1445 pcy)	1592 kg/m^3 (2684 pcy)			
Polycarboxylate High Range Water Reducer		1028 mL/m^3 (26.4fl.oz./yd^3)	880 mL/m^3 (22.6fl.oz./yd^3)			
Air Entraining Admixture		107 mL/m^3 (2.7fl.oz./yd^3)	0			
Fiber	(for low volume fraction)	0	0	3.6 kg/m^3 (6.1 pcy)	4.5 kg/m^3 (7.6 pcy)	79 kg/m^3 (133 pcy)
	(for high volume fraction)			7.2 kg/m^3 (12.2 pcy)	9.0 kg/m^3 (15 pcy)	157 kg/m^3 (266 pcy)

Table 5.3 summarizes the sample labelling nomenclature based on the tested variables of loading type, fiber type, and fiber volume contents.

5.2.2 Bulk Material Property Tests

Each of the mixtures was tested for bulk material properties for consistency, including fresh workability, compressive strength, and split tensile strength. For workability, the concrete mixture was tested for slump flow (ASTM C1611, 2009), while mortar mixtures were tested with a mini-slump test (ASTM C1437, 2013).

Table 5.3 Test variables

Specimen	Stress	Fiber Type	Fiber Content	Specimen
TM-0 (Control)	Tensile	NONE	-	Monolithically cast Fiber-Reinforced Mortar
TM-Y1-L		Slender and Long Polymeric	Low (0.40%)	
TM-Y1-H			High (0.78 %)	
TM-Y2-L		Long Polymeric	Low (0.50%)	
TM-Y2-H			High (1.0%)	
TM-T-L		Short Steel	Low (1.0%)	
TM-T-H			High (2.0%)	
TH-0 (Control)		NONE	-	Composite (Half Concrete Substrate + Half Fiber-Reinforced Mortar)
TH-Y1-L		Slender and Long Polymeric	Low (0.40%)	
TH-Y1-H			High (0.78 %)	
TH-Y2-L		Long Polymeric	Low (0.50%)	
TH-Y2-H			High (1.0%)	
TH-T-L		Short Steel	Low (1.0%)	
TH-T-H			High (2.0%)	
SH-0 (Control)	Shear	NONE	-	Composite (2/3 Concrete Substrate + 1/3 Fiber-Reinforced Mortar)
SH-Y1-L		Slender and Long Polymeric	Low (0.40%)	
SH-Y1-H			High (0.78 %)	
SH-Y2-L		Long Polymeric	Low (0.50%)	
SH-Y2-H			High (1.0%)	
SH-T-L		Short Steel	Low (1.0%)	
SH-T-H			High (2.0%)	

Compressive strength (ASTM C39, 2005; ASTM C109, 2013) was performed using 100x200 mm (4x8 in.) cylinders for the substrate concrete, or using 50 mm (2 in.) cubes for the mortar mixtures, respectively. All Brazilian split-tensile strengths (ASTM C496, 2004) were measured based on 100x200 mm (4x8 in.) cylinders regardless of whether it was concrete or mortar. Fracture properties of the concrete and mortar mixtures were determined using a wedge-split tension 150 mm (6 in.) cube samples similar to that shown in Figure 5.1 and described later. The test was conducted with constant vertical loading rate of 1 mm/min (0.04 in./min) and continued until failure showed at the interface or 2.5 mm of crack opening displacement (COD) is reached. Epoxy gel (4000 psi of bond strength) was utilized to fix rolling devices to the specimen.
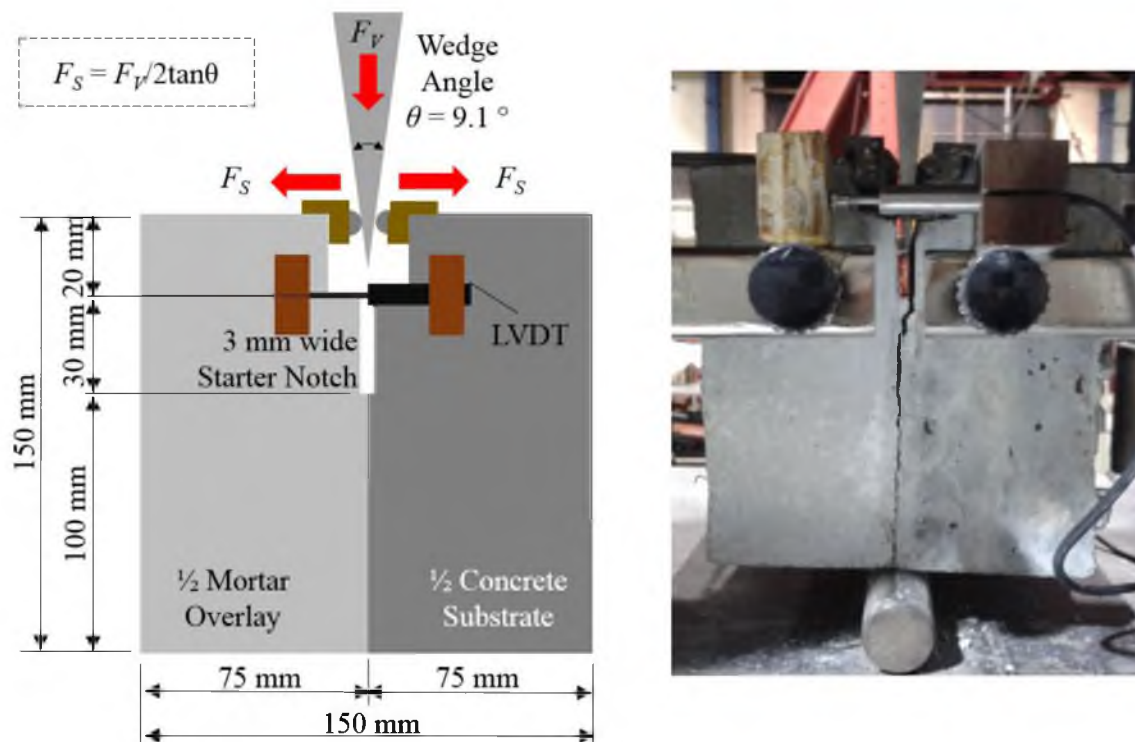
Figure 5.1. Interfacial wedge-splitting tension test configuration and LVDT mounting.

5.2.3 Composite Sample Fabrication

The size of the substrate concrete for the wedge-split test was $150 \times 150 \times 75$ mm ($6 \times 6 \times 3$ in.) and for the bisurface shear test was $150 \times 150 \times 50$ ($6 \times 6 \times 2$ in.). Sandblasting in combination with power-washing was found to be the best method by other researchers to create a rough textured interface similar to field milling (Momayez et al., 2004; Tayeh et al., 2012). The procedure to age and roughen the surface prior to casting the mortar overlay was as follows:

1. Styrofoam inserts placed in mold to occupy space of future overlay material, and an insert used for the roller assembly location for wedge-split specimens

2. Substrate concrete cast

3. At 24 hours from casting, the substrate concrete demolded and placed in fog room

4. Within 3 days of casting, substrate concrete sandblasted and power-washed then placed back in fog room

5. An hour prior to full 28 day cure, contact surface wiped dry with paper towel for saturated surface dry condition

6. The aged substrate concrete was placed back in the mold, with the same styrofoam insert for the roller assembly for the wedge-split specimens

7. Mortar mixture cast

8. At 24 hours from mortar casting, composite mortar-concrete demolded and placed in water bucket for 28 days

9. At the test date, a starter notch was cut in the composite sample for the wedge-split specimens. For the bisurface shear specimens, a guide notch along the side of the samples was cut.

5.2.4 Wedge-Split Tension Test

As listed in Table 5.3, both monolithically cast mixtures and the composite FRM overlay cast against the substrate concrete were tested with the wedge-split tension cube test. The applied vertical load and two opening displacements were measured. From the load versus displacement curve, the tensile bond strength, the fracture energy for bond, and crack growth resistance can be calculated (Hillerborg, 1985; Tschegg, 1991). Two replicate specimens were produced for each wedge split test configuration. Using the method explained in Chapter 3, horizontal splitting force F_S can be calculated according to Eq. (3.9). The test was conducted with a constant vertical loading rate of 1 mm/min (0.04 in./min).

Two linear variable differential transformers (LVDTs) were in line with the notch tip location and clamped against the specimen with a custom-built frame. The recorded average displacement was used to calculate the crack opening displacement (COD). For monolithically cast specimens, a cut-off total fracture energy, $G_{,2.5mm}$, was computed based on the load versus displacement area until the COD reached 2.5 mm (0.1 in.), as shown in Eq. (5.1).

$$G_{2.5mm} = \frac{area(F_{SP} \cdot COD)|_{COD=2.5}}{A} \tag{5.1}$$

where *area* is the sum of the area under the horizontal load F_{SP} versus COD curve, and A is the fracture cross-sectional area ahead of the notch tip (15000 mm^2 or 23.3 in.^{2}).

For the half-cast interfacial specimens, a similar fracture energy for the interface bond (G_{bond}) was computed based on the load-displacement area until the first failure

occurred, as seen in Eq. (5.2).

$$G_{bond} = \frac{area(F_{SP} \cdot COD)}{A} \qquad (5.2)$$

5.2.5 Bisurface Shear Test

Figure 5.2 shows the geometry and loading status of the bisurface shear specimen. The test was conducted with a constant loading rate of 1 mm/min (0.04 in./min). This loading is constant with the tensile splitting test. Two LVDTs were attached to estimate the shear displacement on both the front and back faces of the specimen. The test was determined complete when failure occurred at the interface. The shear bond strength, f_s, from Eq. (5.3) is calculated by dividing the load at failure P_P by the original bonded area A (15000 mm^2 or 23.3 in.^{2}).
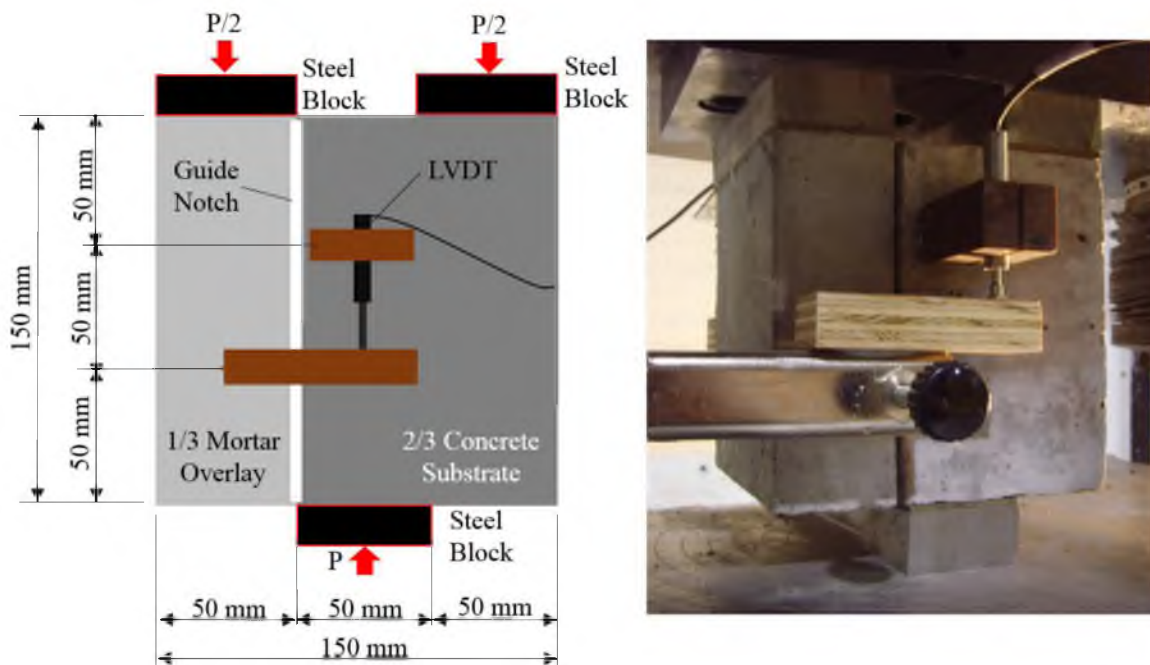
Figure 5.2. Bisurface shear test configuration.

5.3 Experimental Results and Discussion

5.3.1 Bulk Properties

The averaged compressive strengths of the mortar mixtures are shown in Table 5.4 based on three specimens each at 7 and 28 days. Table 5.5 shows that among these mortar mixtures the Brazilian split-tensile strength of the mortar mixtures was slightly higher with fiber reinforcement than that of control unreinforced mortar. It was also found from this small dataset that the tensile strength increased as fiber volume content increased. However, fiber showed the negligible effects on measured compressive strength.

Table 5.4 Fresh and hardened properties of concrete and fiber-reinforced mortar

Type	Slump Flow Concrete, mm Mortar, %	Compressive Strength, 7 days MPa [psi]	COV (%)	Compressive Strength, 28 days MPa [psi]	COV (%)	Split Tensile Strength, 28 days MPa [psi]	COV (%)
Substrate Concrete	508	N/A	N/A	60.7 [8804]	0.6	3.9 [566]	8.0
Control Mortar	125	22.9 [3321]	9.9	30.6 [4438]	9.5	2.1 [305]	18.7
Y1 – 0.40%	N/A	24.4 [3533]	5.8	26.9 [3902]	11.1	2.7 [392]	3.2
Y1 – 0.78%	N/A	18.7 [2712]	11.9	29.9 [4337]	5.9	2.8 [406]	8.5
Y2 – 0.5%	129	23.3 [3379]	2.0	26.6 [3858]	10.3	3.4 [493]	2.4
Y2 – 1.0%	135	20.5 [2973]	10.6	30.7 [4453]	3.3	3.5 [508]	9.2
T - 1.0%	131	26.8 [3887]	8.6	32.0 [4641]	13.3	3.7 [537]	8.1
T - 2.0%	133	25.4 [3684]	10.7	30.3 [4395]	4.5	3.9 [566]	4.1

Note: all strength values are an average of three samples. Slump values are recorded once for each mixture.

Table 5.5 P values (two-tailed) between strength of control mortar versus strength of each fiber-reinforced mortar

	Compressive Strength	Split Tensile Strength
Y1 – 0.40%	0.696	0.0002
Y1 – 0.78%	0.152	0.016
Y2 – 0.5%	0.369	0.002
Y2 – 1.0%	0.353	0.027
T - 1.0%	0.185	0.003
T - 2.0%	0.468	0.004

Note: P value less than 0.05 means not the same.

Table 5.6 lists the fracture properties and Figure 5.3 shows the splitting force versus crack opening displacement curves for monolithically cast mortar specimens. It was originally expected that the TM-T-H (short steel fiber with 2.0% of volume fraction) specimen would show the highest fracture energy. However, this could not be measured because the test failed. Unlike the bulk Brazilian split-tensile test, the wedge-split tensile strength was not found to have a significant trend (see Table 5.7) from the addition of fibers to the mortar. As expected, an increase in fiber volume content among the mortar fracture specimens did result in an increase in the postcracking performance.

Table 5.6 Results for monolithically cast wedge-splitting mortar samples

Specimen	$F_{SP,MAX}$			$G_{2.5mm}$*			$F_{SP,2.5mm}$		
	(kN)	(kip)	COV (%)	(N/m)	(lb/in.)	COV (%)	(kN)	(kip)	COV (%)
TM-0	9.92	2.23	21.4	56.47	0.322	4.0	0	0	-
TM-Y1-L	9.12	2.05	0.5	382	2.181	18.5	2.17	0.49	18.7
TM-Y1-H	11.09	2.49	8.6	606	3.460	18.9	2.65	0.60	19.0
TM-Y2-L	10.83	2.43	1.2	607	3.466	8.2	4.13	0.93	24.2
TM-Y2-H	9.23	2.07	16.2	1117	6.378	8.6	6.90	1.55	11.3
TM-T-L	10.59	2.38	5.6	1222	6.978	10.4	5.25	1.18	13.2
TM-T-H	-								

Note: all wedge-split test result values are an average of two samples.
*Total fracture energy of the unreinforced mortar fails before the 2.5 mm cut-off.
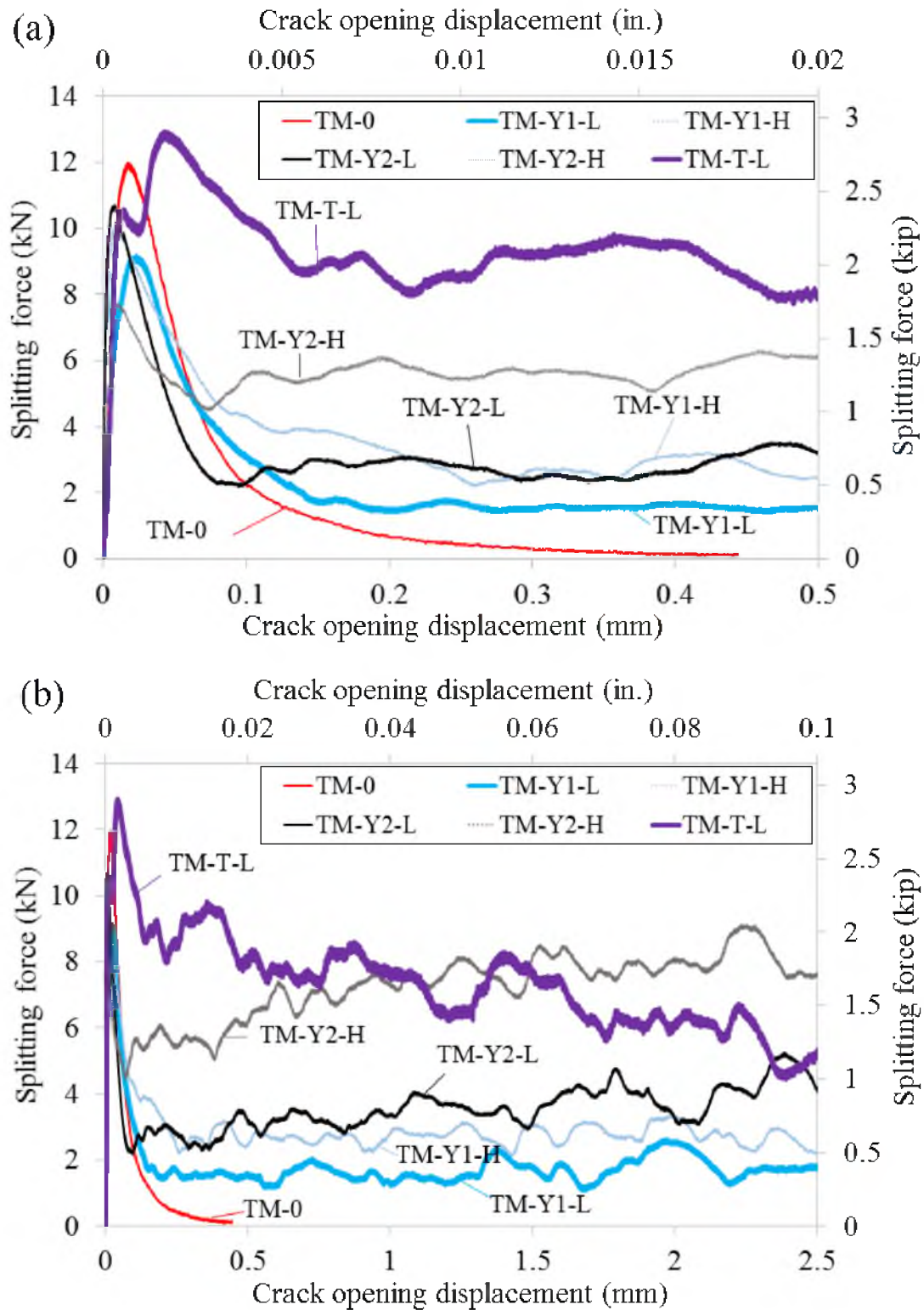
Figure 5.3 Wedge-splitting force versus COD curves for one replicate of each monolithically cast mortar specimens, (a) showing zoomed-in; (b) showing full displacement range.

Table 5.7 P values (two-tailed) between F_{SP} of control mortar versus F_{SP} of each fiber-reinforced mortar

	Splitting Force, F_{SP}
TM-Y1-L	0.771
TM-Y1-H	0.703
TM-Y2-L	0.743
TM-Y2-H	0.817
TM-T-L	0.901
TM-T-H	-

Note: P value less than 0.05 means not the same.

The cut-off fracture energy was again found to slightly decrease for the larger aspect ratio fibers, despite the more dominant effect of the increasing volume content on fracture energy.

5.3.2 Interface Tensile Splitting Results

It can be seen from Figures 5.4, 5.5, and 5.6 that all of the composite samples exhibited a sudden drop in load after the peak tensile bond strength is reached. For specimens containing FRM, a tensile stress was still carried for more than 0.3 mm COD than specimens containing the unreinforced mortar. The main difference between Figure 5.3 and Figures 5.4 to 5.6 is that with the monolithically cast mortar specimens there is a chemical and physical bond across the fracture plane, while the interface composite specimens are expected to only have a macrotexture friction to resist fracture. Table 5.8 shows the peak tensile strength, $F_{SP, MAX}$, and fracture energy for the interfacial tensile bond based on the wedge split composite specimens. Similar to the monolithic wedge split tensile specimens, these interfacial specimens were not found (see Table 5.9) to have a significant trend in peak load from the addition of fibers.
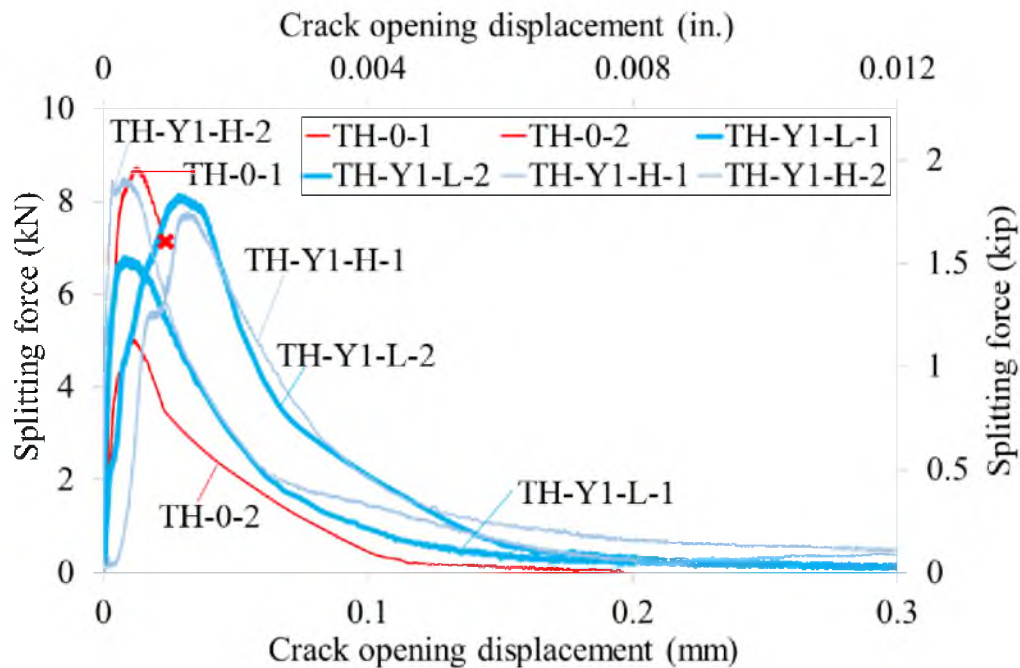
Figure 5.4. Interfacial splitting tension force versus crack opening displacement curves for ½ concrete + ½ slender and long polymeric FRMs.
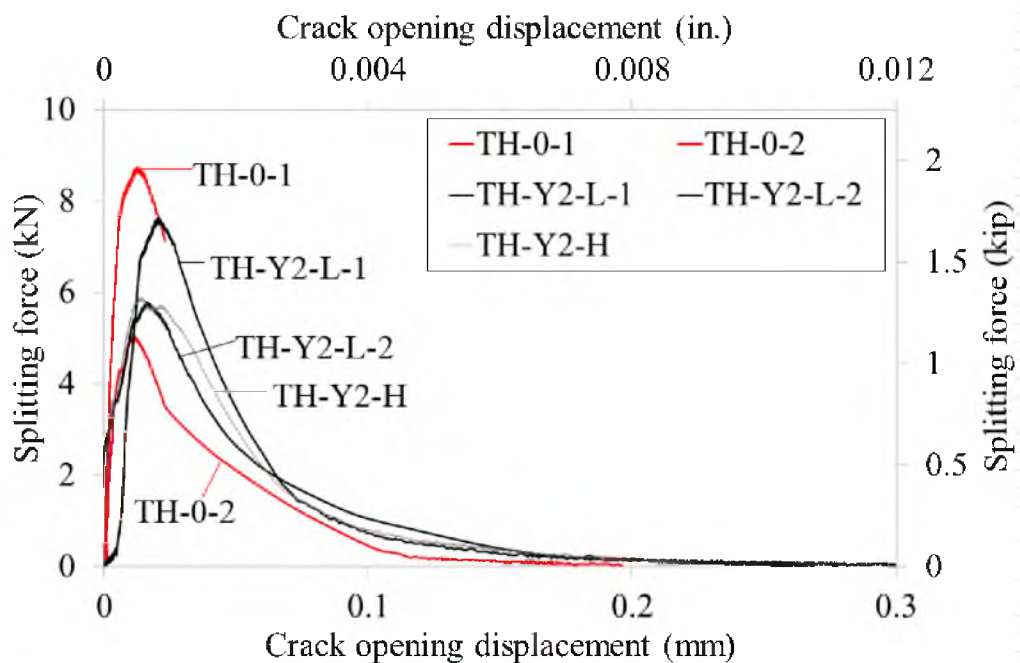
Figure 5.5. Interfacial splitting tension force versus crack opening displacement curves for ½ concrete + ½ long polymeric FRMs.
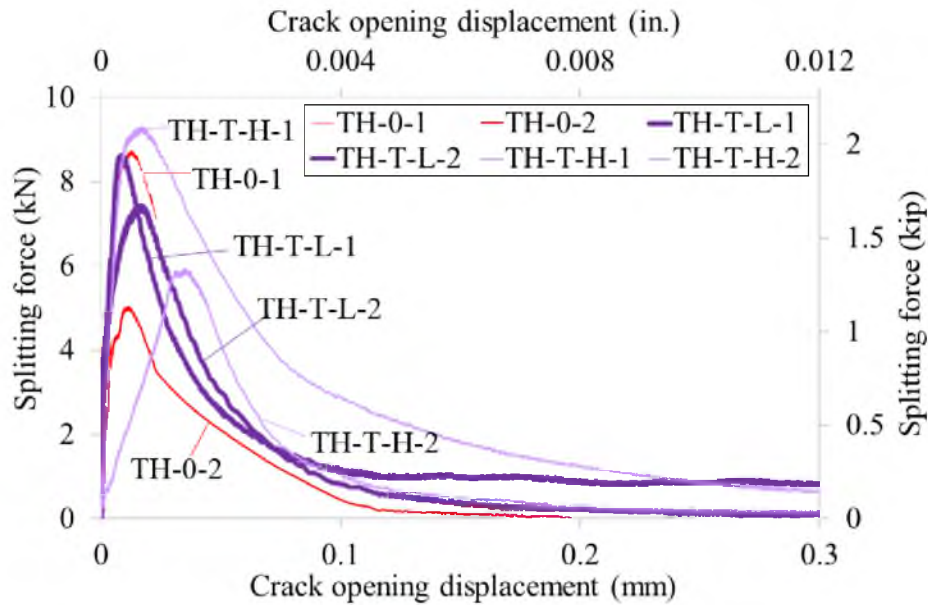
Figure 5.6. Interfacial splitting tension force versus crack opening displacement curves for ½ concrete + ½ short steel FRMs.

Table 5.8 Results for composite ½ concrete + ½ mortar samples

Specimen	$F_{SP,MAX}$			G_{bond}			# of fibers through fracture area
	(kN)	(kip)	COV (%)	(N/m)	(lb/in.)	COV (%)	
TH-0	6.89	1.55	26.9	13.60	0.078	18.4	-
TH-Y1-L	7.46	1.68	9.0	33.18	0.189	20.5	8
TH-Y1-H	8.15	1.83	4.6	79.82	0.456	16.8	45
TH-Y2-L	6.71	1.51	13.8	24.24	0.138	1.3	4
TH-Y2-H	5.87	1.32	-	23.46	0.134	-	9
TH-T-L	8.03	1.81	8.0	69.25	0.395	5.8	30
TH-T-H	7.61	1.71	22.2	70.70	0.404	6.4	35

Note: all wedge split test result values are an average of two samples.

Table 5.9 P values (two-tailed) between control mortar and each fiber-reinforced mortar

	Splitting Force, F_{SP}	Bond Energy, G_{bond}
TH-Y1-L	0.819	0.225
TH-Y1-H	0.626	0.129
TH-Y2-L	0.945	0.149
TH-Y2-H	0.855	0.420
TH-T-L	0.662	0.400
TH-T-H	0.800	0.427

Note: P value less than 0.05 means not the same

Based on the calculated P values, it was also verified that fiber did not show significant effect on tensile bond energy. This might be related to the small number (two replicates) of test specimens. One important finding here is that control mortar specimens showed the lowest tensile bond energy compared to any FRM specimens. Thus, it might not be reasonable to conclude that fiber has no effects on bond energy.

Based on the comparison of averaged bond energy, a slight increase was found with some of the FRM mixture, which is not commonly expected, since the fibers do not cross the original interface surface. In this experiment, the G_{bond} for the FRM specimens containing slender and long polymeric (Y1), long polymeric (Y2), or short steel (T) fibers at the highest fiber contents were about 5.8, 1.7, and 5.2 times higher, respectively, than that of the unreinforced mortar.

A closer look at the fracture surface revealed that many of the samples were found to have a tortuous crack which penetrated both the FRM overlay material and the aged concrete substrate material. As shown in Figure 5.7, a clear correlation was found (with a 97% confidence) between the number of fibers crossing the fracture plane, not necessarily the original fiber volume content, with the increasing tensile G_{bond}. It was also found that FRM specimens containing Y1 or T fibers had roughly 4-5 times more fibers crossing the fractured path compared to FRM specimen with Y2 fiber. It is expected that these fibers located in the crack path were the cause of the increased tensile bond energy performance compared to the unreinforced mortar overlay. However, further research might be necessary to identify the mechanism by which fiber count influenced increased tensile bond energy.
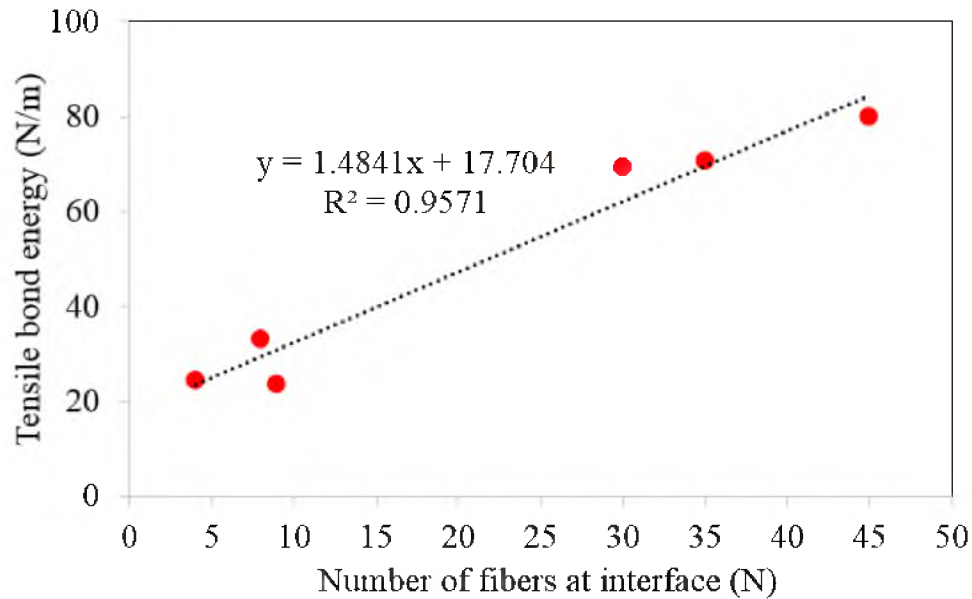
Figure 5.7. Plot shows the relation between G_{bond} and number of fibers at the fractured interface.

5.3.3 Bisurface Shear Results

Figure 5.8 shows the shear load versus displacement curves of the bisurface shear specimens. All composite specimens exhibited failure promptly after the ultimate shear bond, P_P, was reached. On average, most FRM samples exhibited an increased shear bond strength (shown in Table 5.10) compared to unreinforced mortar overlay samples. However, short steel (T) samples at high fiber content actually showed a significant decrease in shear strength at the interface. Although this test method was selected for producing low variability, the coefficient of variation is still relatively high for many of these samples and therefore no statistically significant trends could be drawn on most samples, as shown in Table 5.10. Table 5.11 shows the calculated P values between plain control mortar versus each fiber-reinforced mortar. It can be seen there were no significant fiber effects on measured shear bond strengths.
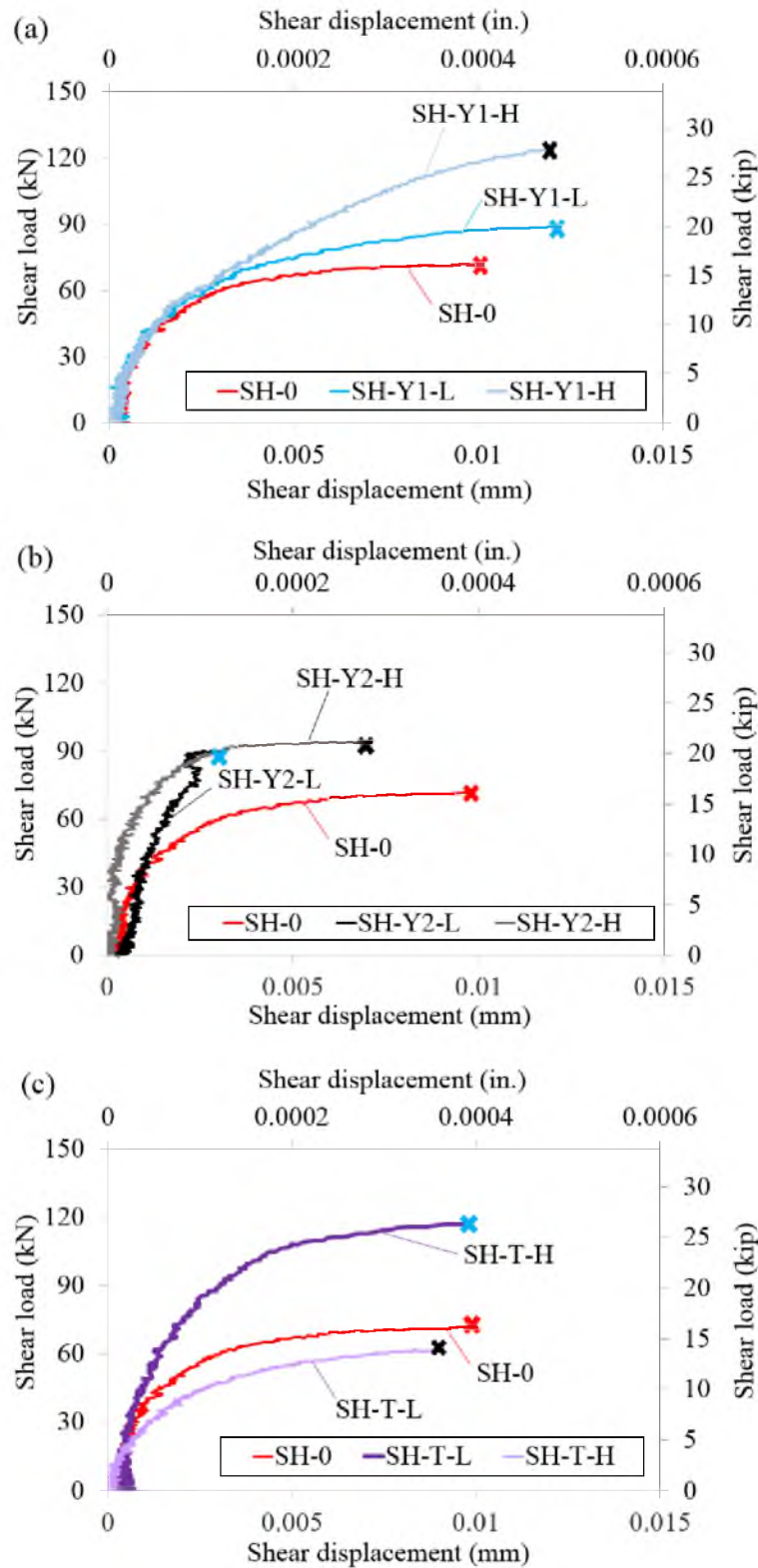
Figure 5.8. Averaged shear load-displacement curves for composite samples: (a) 2/3 concrete + 1/3 slender and long polymeric FRM; (b) 2/3 concrete + 1/3 long polymeric FRC; (c) 2/3 concrete + 1/3 short steel FRM.

Table 5.10 Results for bisurface shear test

Specimen	Shear Load P_P		Shear Bond Strength f_s			# of fibers through fracture area
	(kN)	(kip)	(MPa)	(psi)	COV (%)	
SH-0	71.79	16.14	4.79	695	14.4	-
SH-Y1-L	90.15	20.27	6.01	872	9.9	17
SH-Y1-H	124.48	27.98	8.30	1204	1.9	23
SH-Y2-L	81.15	18.24	5.41	785	26.7	2
SH-Y2-H	85.50	19.22	5.70	827	43.5	4
SH-T-L	117.22	26.35	7.81	1133	2.7	18
SH-T-H	62.91	14.14	4.19	608	26.4	35

Note: all bi-surface shear test result values are an average of two samples

Table 5.11 P values (two-tailed) between control mortar versus each fiber-reinforced mortar

	Shear Load, P_P	Shear Bond Strength, f_s
SH-Y1-L	0.409	0.409
SH-Y1-H	0.177	0.177
SH-Y2-L	0.874	0.874
SH-Y2-H	0.850	0.850
SH-T-L	0.209	0.209
SH-T-H	0.196	0.196

Note: P value less than 0.05 means not the same.

Unlike the previous tensile bond energy discovery, the number of fibers at the interface of the shear specimens (see Figure 5.9) was not correlated with the measured shear strength. It is possible that shear bond energy instead of strength might indicate a correlation with fiber content. Any possible postcracking response was not captured by the testing apparatus, and thus a shear bond energy could not be determined at this time. Further research is still needed to understand how fibers could influence the shear interfacial bond performance. Also, further research might be necessary to determine the suitable loading rate for shear bond test.
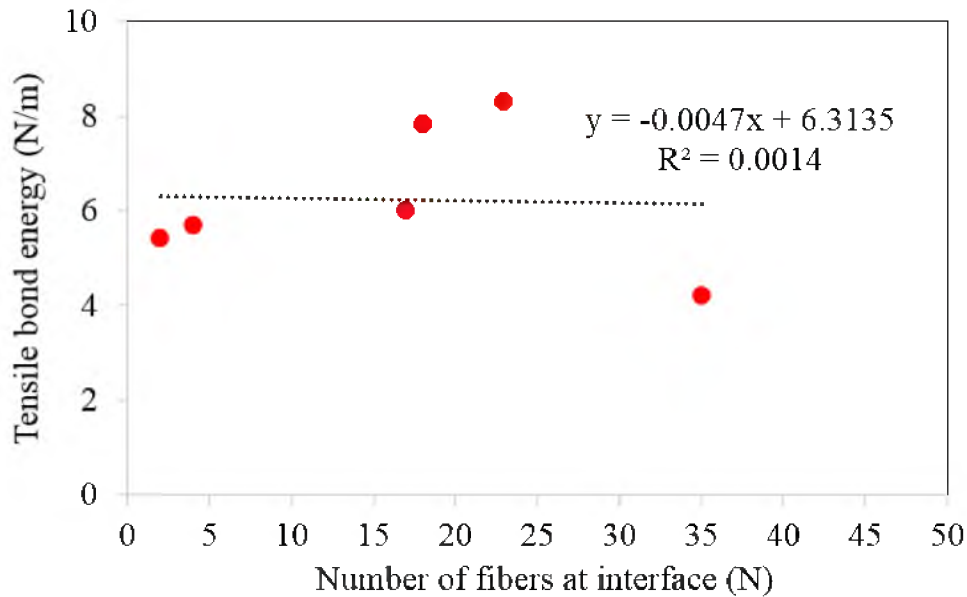
Figure 5.9. Plot shows the relation between f_s and number of fibers at the fractured interface.

5.4 Summary and Findings

Previous reports of field-constructed FRC overlays have indicated that fiber reinforcement may reduce debonding. This chapter shows experimentally determined tensile and shear bond properties that were measured for different fiber-reinforced mortar overlay materials cast against a sand-blasted 28-day old concrete substrate. One steel and two polymeric macrofibers were compared as reinforcement in the mortar mixture. The wedge-split tension cube test and the bisurface shear cube test were the methods selected to measure the properties, based on previous research indicating these had low variability in measured properties. Based on the measured property results, the following conclusions were drawn.

- All monolithic specimens containing fiber reinforcement did improve the measured split tensile strength and tensile fracture energy compared to unreinforced mortar specimens. Composite overlay specimens were found to have 2-6 times higher

tensile interfacial bond energy with the addition of fiber reinforcement.

- No statistical trend could be found with the interface shear strength of the composite specimens in relation to the fiber type or fiber content.

- The actual number of fibers crossing the tortuous fractured path during tensile interfacial bond fracture of the composite specimens was found to be well correlated with the measured tensile bond energy of the test.

Overall, selected fibers did not show any significant effects on measured tensile and shear bond strengths. This is due to the fact that the selected test methods only quantified pure bond strengths.

5.5 References

ASTM Standard C109, Standard Test Method for Compressive Strength of Hydraulic Cement Mortars (Using 2-in, or [50-mm] Cube Specimens). ASTM C109/C109M-13e1, West Conshohocken Pennsylvania: 2013.

ASTM Standard C1437, Standard Test Method for Flow of Hydraulic Cement Mortar. ASTM C1437-13, West Conshohocken Pennsylvania: 2013.

ASTM Standard C1611, Standard Test Method for Slump Flow of Self-Consolidating Concrete. ASTM C1611/C1611M-14, West Conshohocken Pennsylvania: 2014.

ASTM Standard C39, Standard Test Method for Compressive Strength of Cylindrical Concrete Specimens. ASTM C39/C39M-15a, West Conshohocken Pennsylvania: 2015.

ASTM Standard C496, Standard Test Method for Splitting Tensile Strength of Cylindrical Concrete Specimens. ASTM C496/C496M-11, West Conshohocken Pennsylvania: 2004.

ASTM Standard C1609, Standard Test Method for Flexural Performance of Fiber Reinforced Concrete (Using Beam with Third-point Loading). ASTM C1609/C1609M-05, West Conshohocken Pennsylvania: 2007.

Chanvillard, G.; Aitcin, P.; Lupien, C. Field Evaluation of Steel Fiber Reinforced Concrete Overlay with Various Bonding Mechanisms. *Transportation Research Record: Journal of the Transportation Research Board* **1989**, *1226*, 48-56.

Delatte, N. J.; Williamson, M. S.; Fowler, D. W. Bond Strength Development with Maturity of High-Early-Strength Bonded Concrete Overlays. *ACI Materials Journal* **2000**, *97(2)*, 272-280.

Hillerborg, A. The Theoretical Basis of a Method to Determine the Fracture Energy G_F of Concrete. *Materials and Structures* **1985**, *18(4)*, 291-296.

Momayez, A.; Ramezanianpour, A.; Rajaie, H.; Ehsani, M. Bi-surface Shear Test for Evaluating Bond between Existing and New Concrete. *ACI Materials Journal* **2004**, *101(2)*, 99-106.

Sevil, T.; Baran, M.; Bilir, T.; Canbay, E. Use of Steel Fiber Reinforced Mortar for Seismic Strengthening. *Construction and Building Materials* **2011**, *25(2)*, 892-899.

Tayeh, B. A.; Bakar, B. A.; Johari, M. M.; Voo, Y. L. Mechanical and Permeability Properties of the Interface between Normal Concrete Substrate and Ultra High Performance Fiber Concrete Overlay. *Construction and Building Materials* **2012**, *36*, 538-548.

Tschegg, E., New Equipments for Fracture Tests on Concrete. *Journal of Material Testing* **1991**, *33*, 338-342.

CHAPTER 6

FINITE ELEMENT MODELING OF FRC OVERLAYS

SUBJECTED TO TEMPERATURE GRADIENTS

6.1 Introduction

This chapter explains the analytical approach for predicting the crack width of thin

fiber-reinforced concrete (FRC) overlays. A finite element model was created as a two-

dimensional analysis with a focus on the crack opening widths and debonding of the FRC

overlay. Three different model geometries were created of each field slab size (1.12, 1.68,

and 3.35 m) and underlying structural pavement thickness as shown in Figures 4.1 and 4.2.

For each model geometry, a calculated equivalent thermal load was applied at specific ages

(3, 8, and 20 days) rather than a time-dependent model. A sensitivity analysis was carried

out to determine how variation in FRC fracture energy and other pavement design

parameters may change the crack width, vertical lift-off, and debonding length.

6.2 Finite Element Modeling

The magnitude of the thermal load was applied as a type of an equivalent deflection,

δ_T, shown as Eq. (6.1), based on the back-calculated shrinkage gradient and temperature

gradient expected at that age. Both shrinkage and temperature were simplified to be linear

gradients for this study.

The top of FRC layer was assumed to be subjected to the same free drying shrinkage as shown in Figure 4.3(a). The bottom interface was assumed to be restrained by the friction and bond with the HMA substructure, as defined in Eq. (4.2). The equation for displacement was derived by using elastic beam theory.

$$\delta_T = \frac{(\Delta\varepsilon_{sh} + \alpha_T \Delta T_{slab})L_{slab}^2}{2H} \tag{6.1}$$

where $\Delta\varepsilon_{sh}$: shrinkage strain gradient between top and bottom of the FRC slab shown in Eq. (4.2) (mm/mm); α_T: coefficient of thermal expansion of FRC (mm/mm-°C); ΔT_{slab}: linear temperature difference between the top and bottom of the slab (°C), assumed to be 2 °C for the field 50 mm overlay as stated previously or this would be 6 °C for an equivalent 150 mm overlay; L_{slab}: saw-cut joint spacing (mm); and H: slab thickness (mm). $\varepsilon_{sh,restrained}$ was estimated based on other literature studies to be 25 x 10^-6 mm/mm for the bottom of a concrete slab cast against aged concrete (Gilbert et al., 2012). Figure 6.1 shows the locations where equivalent deflections were applied in the model.
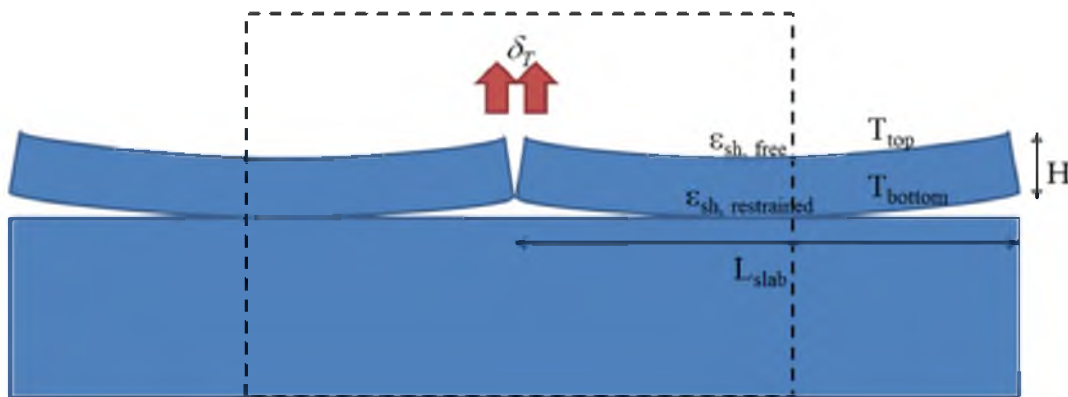
Figure 6.1. Applied quivalent deflection in the finite element model.

The model geometry consists of two side-by-side FRC half-slabs supported by HMA and subgrade, as illustrated in Figure 6.2. The HMA and underlying binder base-course properties (as shown in Table 6.1) were assumed to be constant at all ages in order to simplify the model. The subgrade was idealized as an elastic foundation that can only support compression.

In this study, a stiff elastic foundation stiffness value of 150 kPa/mm was applied as the default in order to create a worst-case curling scenario (Gaedicke and Roesler, 2009). A saw-cut joint which has 3 mm of width and 12 mm of depth was also created in the model geometry to match the field construction. No other external constraints were applied to the FRC slabs.

The contact areas across both the joint location FRC and across the FRC-HMA interface were defined using surface-based cohesive behaviors (ABAQUS, 2014). A linear traction-separation law was applied to describe both cohesive interfaces. This assumed an initial elastic behavior as defined by a penalty stiffness, in this case 1×10^{12} Pa/m was applied (Gaedicke and Roesler, 2009). After a maximum tensile strength is reached in the cohesive interface, a damage evolution is initiated. Debonding at the FRC-HMA interface is defined for nodes where this damage initiation has begun. The traction carried across the interfaces is defined based on the fracture energy and tensile strength of material. Table 6.1 shows the defined material and fracture properties in the model.

Fracture energy at the joint location was varied from 80 N/m to 3500 N/m to account for the possible expected range of fiber-bridging effect for plain unreinforced concrete to a 0.5% volume fraction of polymeric FRC at 7 days. All other properties except for fracture energy at joint location were constant.
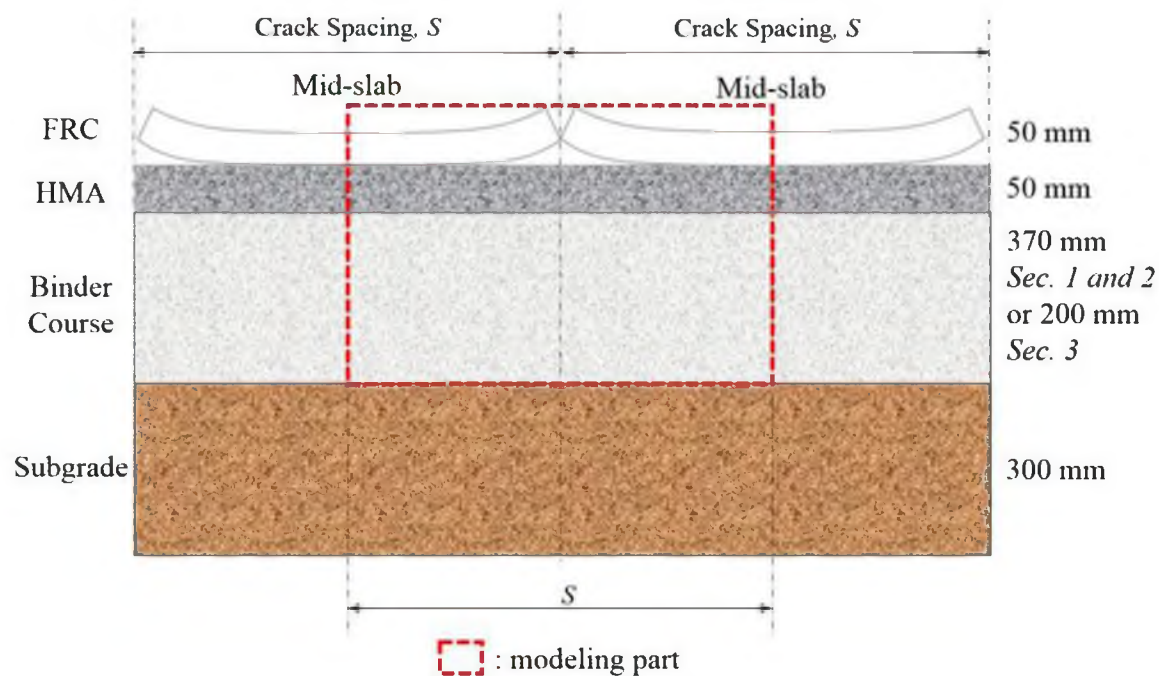
Figure 6.2. Diagram shows the 2D modeling boundaries for the finite element analysis.

Table 6.1 Applied material and fracture properties for FEM

Layer	Material Property	Value
FRC	Density (kg/m^3)	2313
	Elastic Modulus (GPa)	31.7
	Poisson's ratio	0.15
	Coefficient of thermal expansion (/$^{\circ}$C)	10×10^{-6}
HMA	Density (kg/m^3)	2300
	Elastic Modulus (GPa)	2.75
	Poisson's ratio	0.30
Binder (sub-base)	Density (kg/m^3)	1900
	Elastic Modulus (GPa)	0.3
	Poisson's ratio	0.35
Cohesive Interface	Fracture Property	Value
Joint location at FRC layer	Penalty stiffness (Pa/m)	1×10^{12}
	Fracture energy (N/m)	Varies (80 to 3500)
	Tensile strength (MPa)	2.0
FRC-HMA interface	Penalty stiffness (Pa/m)	1×10^{12}
	Fracture energy (N/m)	70
	Tensile bond strength (MPa)	0.5

Figure 6.3 shows a zoomed-in view of the stress distribution of the developed model as it gradually applied a single daytime thermal gradient load. The model predicts that at this thermal magnitude of 0.4 °C/mm, a crack and some debonding will occur, as did occur in many of the slabs in the field project. It should be restated that the developed model is not a time-dependent model. Thus, a step in Figure 6.3 indicates a unit of computation time based out of 1 second to achieve the thermal gradient magnitude applied in the analysis. The calculated crack widths from the numerical analysis were compared to crack widths from the field observation, as shown in Table 6.2. The calculated crack widths for Section 1 and Section 3 were within 18% or less than 0.04 mm difference of the actual experimental measurements. Although the crack widths for Section 2 underestimated the measured crack width by up to 32% (or 0.17 mm difference), some of this is anticipated due to either human error in measuring the crack widths or to statistical variability associated with the constructed FRC.
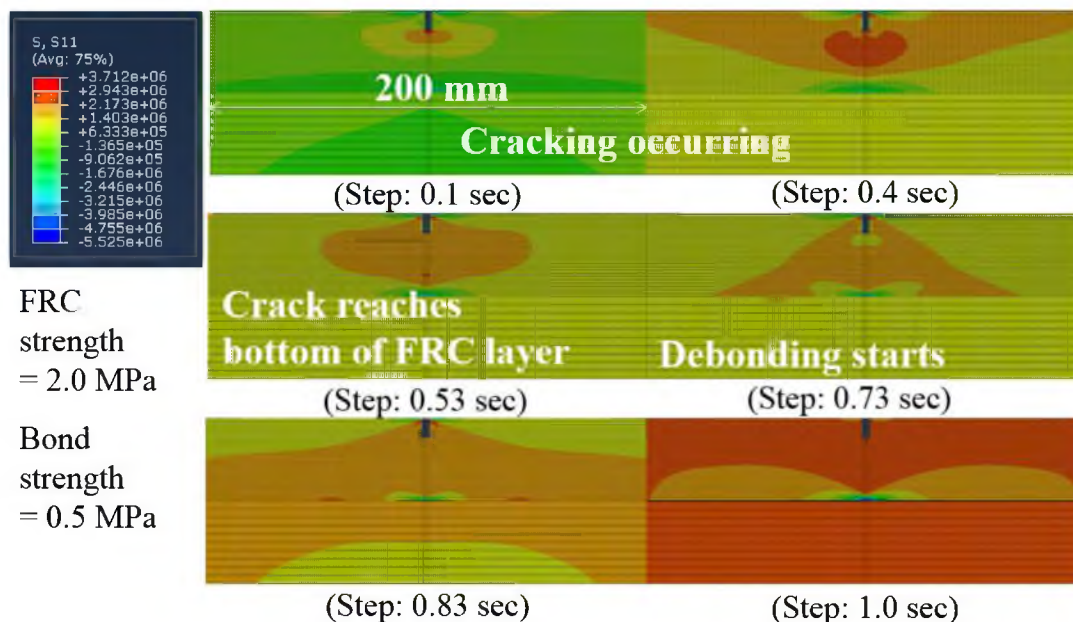
Figure 6.3. Zoomed-in stress distribution showing cracking and debonding near the joint.

Table 6.2 Actual field and calculated crack widths from FEM

Age (days)	Section 1 (1.12 m)		Section 2 (1.68 m)		Section 3 (3.35 m)	
	Calculated crack width (mm) from FEM					
	Actual	FEM	Actual	FEM	Actual	FEM
3	0.226	0.186 [-18%]	0.525	0.355 [-32%]	0.530	0.491 [-7%]
8	0.270	0.297 [+10%]	0.563	0.437 [-22%]	NA	0.645
20	0.390	0.362 [-7%]	0.583	0.608 [+0.4%]	0.900	0.889 [-1%]

Note: values in brackets indicate either +% overpredicted crack or -% underpredicted crack widths

6.3 Sensitivity Analysis

By using the developed model, the effects of the FRC fracture energy across a cracked joint, the tensile bond strength at the interface, elastic modulus of the FRC, and stiffness of elastic foundation were investigated. For each of these parameters that were varied, the crack width (w), debonding length (L_{deb}), and vertical deflection (δ_{lift}) were reported. Section 1 at 3 days' age was selected for this sensitivity analysis.

As illustrated in Figures 6.4 and 6.5, w, L_{deb}, and δ_{lift} all decreased as either the fracture energy or interface tensile bond strength were increased. The w and L_{deb} decreased by 13% and 15%, respectively, as the concrete elastic modulus is increased from that expected at 3 days versus 28 days: 15 GPa to 31.7 GPa. It was expected that a high elastic modulus will show greater w and L_{deb} (Lange and Shin, 2001). However, L_{deb} was not greatly affected by the variation of elastic modulus of the FRC layer. It was also found that the w, L_{deb}, and δ_{lift} all increased by 4, 6, and 22 times, respectively, with an increased stiffness of the elastic foundation from 50 kPa/mm to 150 kPa/mm. This trend is reasonable because it is expected that the softer soil with lower stiffness would have a lower deflection under the same pressure.
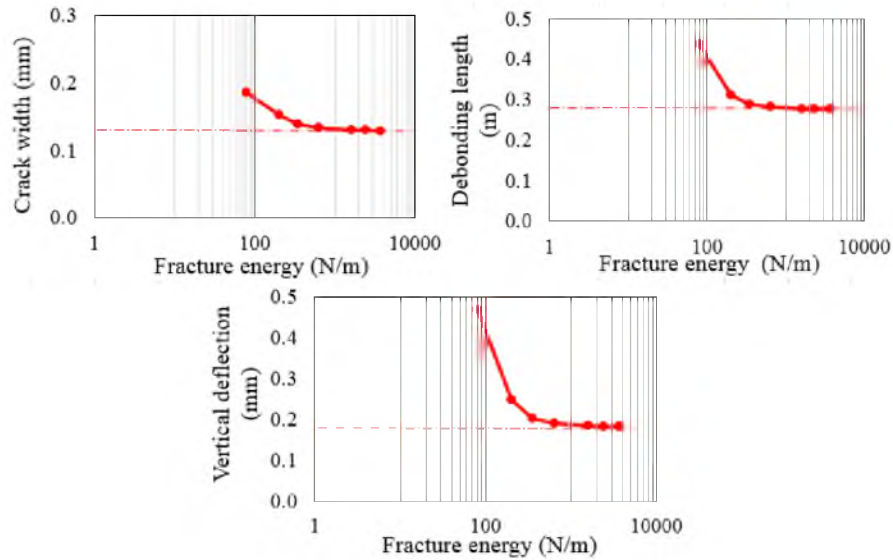
Figure 6.4. Plots show how different fracture energy values in the FEM affect the crack width, debonding length, vertical deflection at the joint representing Section 1 with 3 days-equivalent loading.
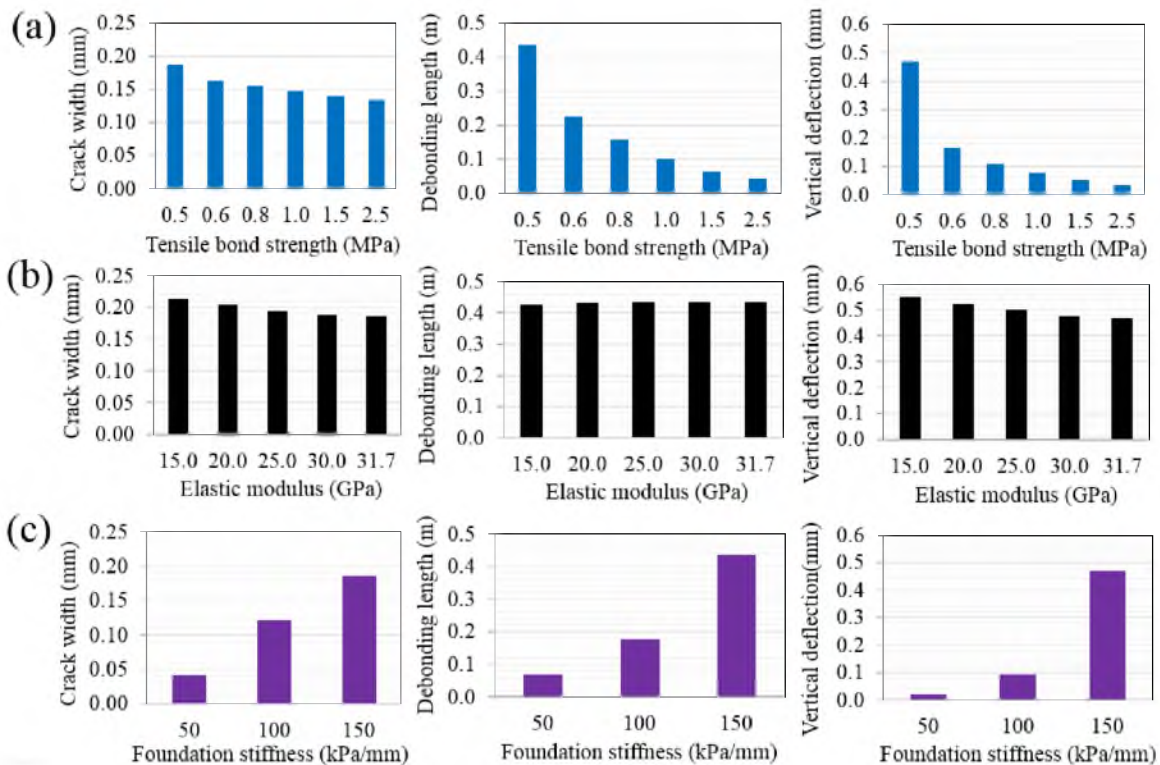
Figure 6.5. Plots show how different material inputs affect the crack width, debonding length, and vertical deflection at the joint representing Section 1 in the model. (a) effect of tensile bond strength on w, L_{deb}, and δ_{lift}; (b) effect of elastic modulus on w, L_{deb}, and δ_{lift}; (c) effect of foundation stiffness on w, L_{deb}, and δ_{lift}.

As confirmed by the sensitivity analysis, the L_{deb} is not as affected by fracture energy of the FRC; or in other words, L_{deb} is influenced primarily by the subgrade stiffness and interfacial tensile bond strength between the FRC and underlying HMA.

6.4 Fracture Energy Effect

The fracture energy for each section was varied to understand the influence of fiber-bridging effect. A unique finding made was that for Section 1, the effect of fracture energy was not a significant factor to improve the prediction of crack width (see Figure 6.6 (a)). In this case, the crack widths with using FRC were reduced by approximately 11% compared to equivalent design containing plain concrete with a fracture energy of 80 N/m.
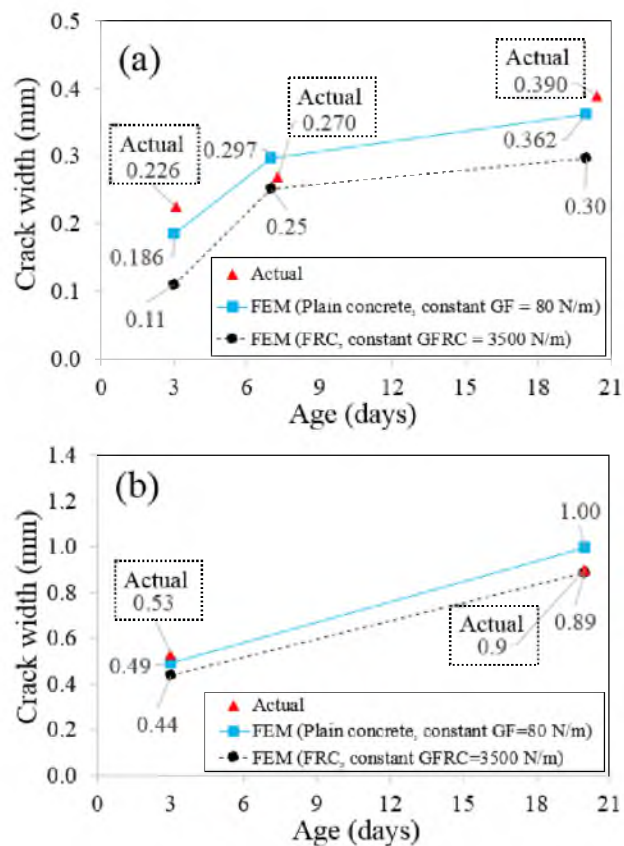
Figure 6.6. Fracture energy effect on the crack width for (a) Section 1 and (b) Section 3 (with fixed saw-cut joint spacing).

For Section 1 (see Figure 6.4), a minimum fracture energy of approximately 200 N/m is needed to reduce crack widths and would also likely to be closer matched the actual field results. For Section 3, however, the crack widths response is more closely matched with the actual crack widths for when the joint FRC fracture was increased to 3500 N/m by 20 days' age.

6.5 Summary and Findings

A simple finite element model was developed to analyze other material properties on crack width, vertical deflection and debonding length of a FRC overlay. As expected, high subgrade stiffness increased the measured crack width, vertical deflection, and debonding length exhibited from the FRC overlay. The developed model was able to predict crack widths within 0.17 mm (or 26%) of the same field-constructed overlay subjected only to environmental loading. Fracture energy at the joint location in the model was varied to investigate the fiber-bridging effect. Among 3.35 m (11 ft.) slab sizes, the developed model was able to predict the crack width within 11% with a FRC fracture energy of 3500 N/m.

6.6 References

ABAQUS, *ABAQUS/standard user's Manual*, Hibbitt, 2001.

Gaedicke, C.; Roesler, J. Fracture-Based Method to Determine the Flexural Load Capacity of Concrete Slabs. *FAA COE Rep* **2009**, *31*.

Gilbert, R.; Bradford, M.; Gholamhoseini, A.; Chang, Z.-T. Effects of Shrinkage on the Long-Term Stresses and Deformations of Composite Concrete Slabs. *Engineering Structures* **2012**, *40*, 9-19.

Lange, D.; Shin, H.-C. Early Age Stresses and Debonding in Bonded Concrete Overlays. *Transportation Research Record: Journal of the Transportation Research Board* **2001**, *1778*, 174-181.

CHAPTER 7

COMPARISON OF DOWEL BARS TO FRC OVERLAYS

7.1 Introduction

Dowels located in concrete pavement play a significant role in increasing load transfer efficiency and reducing joint deflection. Many experimental and analytical studies have been carried out to investigate the performance of dowel bars in concrete pavement, such as load transfer efficiency, stress concentration, joint opening, and pull-out behavior (Bronuela et al., 2015; Davids, 2000; Ioannides and Korovesis, 1992; Mack et al., 1998; Maitra et al., 2009; Pierce, 1997; Prabhu et al., 2009). The objective of this chapter is to verify whether fiber reinforcements are comparative to dowels in resisting crack opening width, debonding length, and vertical deflection. The previously developed finite element model in Chapter 6 was modified to consider a single dowel bar located at the FRC layer. In practice, dowels are not applicable in a 50 mm (2") thick pavement section. Thus, the thickness of the FRC layer was increased to 150 mm (6"), which is more common for dowels to be used. The material properties, load, contact, and boundary conditions utilized in the model were kept the same as used in the previous model except for the increased overlay thickness and the optional placement of a single dowel bar across the joint. Crack width (w), debonding length (L_{deb}), and deflection (δ_{lift}) were monitored and compared between dowelled versus undowelled and among plain versus FRC as the overlay material

in the dowelled case. The effects of two commonly-found dowel diameters, three reported concrete-dowel friction coefficients, and three dowel lengths were investigated in this study.

7.2 Model Geometries

Table 7.1 shows the summary of state practices concerning dowel bar diameter as a function of pavement thickness (Snyder, 2011). It can be seen that dowels can be applicable in at least 150 mm (6") slab thickness, and most states use 25 mm (1") dowel bar diameter for 150 mm (6") thickness pavement. Figure 7.1 shows the dimensions of the model, modeling boundary, and finite element mesh. Two adjacent half-slabs 0.755 m or 2.3 m long were modeled, connected with a cohesive zone at the joint, and an optional dowel bar was placed at mid-height (75 mm) of the slab. Common practice for 150 mm (6") thick pavements is to use dowel bars that are between 19 to 32 mm (0.75 to 1.25") in diameter and 457 mm (18") long (Snyder, 2011). It was expected that a larger diameter, longer length, and higher ungreased surface would have reduced deflections. Economic issues, placement challenges, and increased stresses from high-friction bonds have led the industry to restrict the dimensions to smaller diameters and standardized lengths, with greased dowels for more slippage of the dowel during loading. Underneath the slabs is a 50 mm (2") thick Hot Mix Asphalt (HMA) layer followed by a tied 370 mm thick binder coarse. A separate cohesive zone was defined between the concrete overlay pavement and underlying HMA layer. The subgrade was idealized as an elastic foundation that only supports compression. An initial notch at the joint location was 3 mm wide and 12 mm deep to simulate a constructed saw-cut.

Table 7.1 Common dowel diameters (Snyder, 2011)

| Thickness	6.0 in.	6.5 in.	7.0 in.	7.5 in.	8.0 in.	8.5 in.	9.0 in.	9.5 in.	10 in.
California	1.250	1.250	1.250	1.250	1.250	1.500	1.500	1.500	1.500
Iowa	0.750	0.750	0.750	0.750	1.250	1.250	1.250	1.250	1.500
Illinois	1.000	1.000	1.250	1.250	1.500	1.500	1.500	1.500	1.500
Michigan	1.000	1.000	1.000	1.000	1.250	1.250	1.250	1.250	1.250
Minnesota	1.000	1.000	1.250	1.250	1.250	1.250	1.250	1.250	1.250
Missouri	N/A	N/A	1.250	1.250	1.250	1.250	1.250	1.250	1.250
Ohio	1.000	1.000	1.000	1.000	1.000	1.250	1.250	1.250	1.250
Texas	N/A	N/A	N/A	N/A	1.000	1.000	1.125	1.125	1.250
Wisconsin	N/A	N/A	1.000	1.000	1.250	1.250	1.250	1.250	1.500
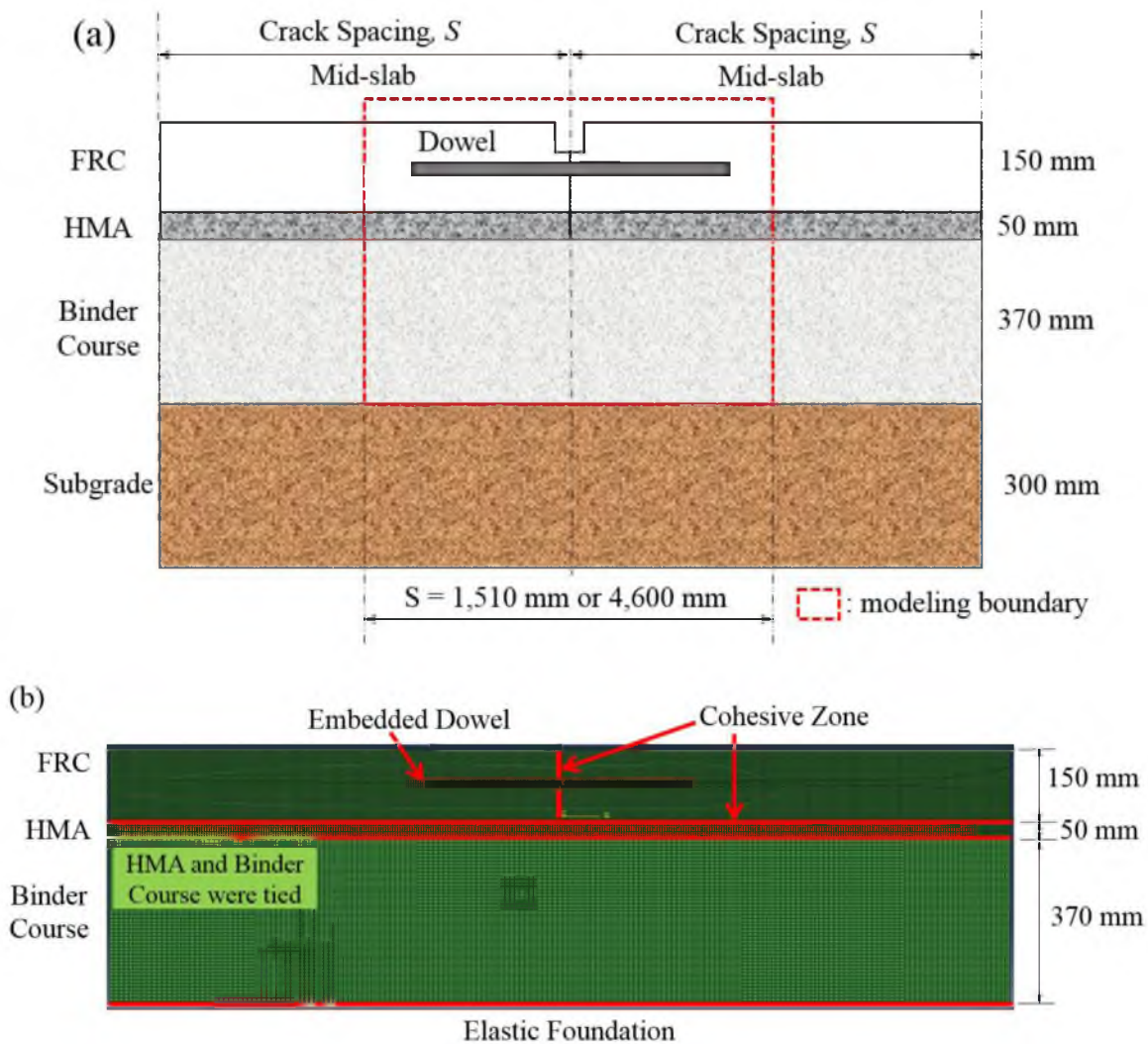
Figure 7.1. Diagrams for (a) modeling boundaries; (b) finite element mesh.

The modeling boundary was simplified to focus on the top overlay joint and interface behavior rather than considering strains or loading distributed through the entire pavement structures.

7.3 Material and Interface Properties

Table 7.2 and Table 7.3 summarize the defined material and interface properties, respectively. The dowel was modeled to be low-carbon steel with isotropic linear elastic properties. The same linear traction-separation laws introduced in Chapter 6 were applied in this model. 80 N/m of fracture energy was applied to simulate the precast cohesion and 3500 N/m was utilized for the FRC full cohesion. All material and interface properties were constant with previous model except for dowel properties.

Table 7.2 Applied material properties

Layer	Material Property	Value
Top Layer: PCC* or FRC	Density (kg/m^3)	2313
	Elastic Modulus (GPa)	31.7
	Poisson's ratio	0.15
	Coefficient of thermal expansion (/$^\circ$C)	10 x 10^{-6}
	Fracture energy (N/m)	0 or 3500
HMA	Density (kg/m^3)	2300
	Elastic Modulus (GPa)	2.75
	Poisson's ratio	0.30
Binder Coarse	Density (kg/m^3)	1900
	Elastic Modulus (GPa)	0.3
	Poisson's ratio	0.35
Dowel	Density (kg/m^3)	7800
	Elastic Modulus (GPa)	200
	Poisson's ratio	0.30
	Coefficient of thermal expansion (/$^\circ$C)	12 x 10^{-6}

* in this case the PCC material was assumed to have a worst-case scenario of zero fracture energy, such as a precast panel might have.

Table 7.3 Applied interface properties

Cohesive Interfaces	Interface Property	Value
Joint with Pre-cast cohesion	Penalty stiffness (Pa/m)	1×10^{12}
	Fracture energy (N/m)	80
	Tensile strength (MPa)	2.0
Joint with FRC full cohesion	Penalty stiffness (Pa/m)	1×10^{12}
	Fracture energy (N/m)	3500
	Tensile strength (MPa)	2.0
Overlay-HMA interface	Penalty stiffness (Pa/m)	1×10^{12}
	Fracture energy (N/m)	70
	Tensile bond strength (MPa)	0.5

7.4 Dowel-Concrete Interaction

The contact between dowel and concrete was modeled as a hard contact, which is a unique option in ABAQUS to define the friction between two separate materials. This option is based on the modified friction coulomb model, as shown in Figure 7.2. Khazanovich and coworkers proposed this modified coulomb method to analyze the dowel-PCC interaction (Khazanovich et al., 2001). In the same study, the authors also suggested that a friction coefficient of 0.3 and a shear strength of 2.1 MPa showed good agreement with experimental results (Khazanovich et al., 2009).
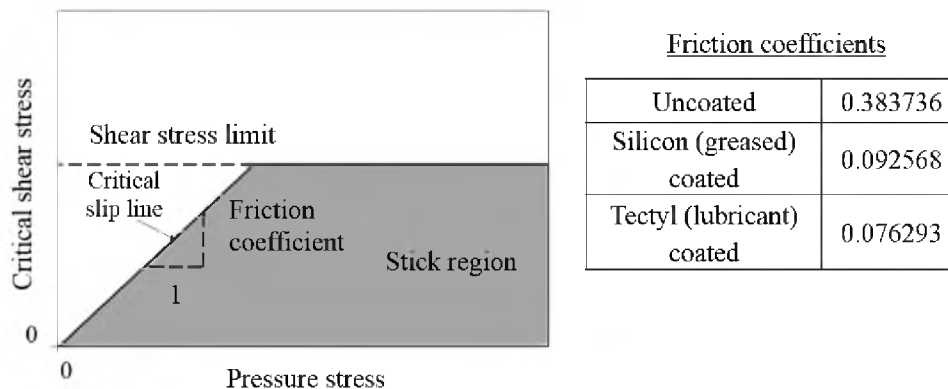

Friction coefficients

Uncoated	0.383736
Silicon (greased) coated	0.092568
Tectyl (lubricant) coated	0.076293

Figure 7.2. Modified coulomb model (Khazanovich et al, 2001)

7.5 Applied Temperature Gradient Loading to Overlay

The temperature is linear and only applied to the overlay as a positive 20°C difference at the top of the slab (daytime curling). An equivalent displacement at the top joint opening was the applied load. The equivalent displacement was calculated (according to Chapter 6) based on strains from the concrete free drying shrinkage at 3 days and the linear temperature gradient strain.

7.6 Analytical Results

Figure 7.3 (a), (b), and (c) show the stress distributions in a 150 mm (6 in.) thick overlay of either plain concrete without fibers or dowels, a fiber-reinforced concrete, and a PCC overlay with a dowel bar, respectively. As the pavement is subjected to a positive temperature gradient of 20 °C (resembling changes in daytime temperature, see Figure 4.3 (b) and (c)), in all cases the tensile opening of the joint near the top is first seen, followed by different patterns in the stress fields as the crack reaches the interface of the HMA layer below or the dowel bar at the mid-overlay height. Similar to the response of the 50 mm (2 in.) overlay (as shown in Chapter 6), some debonding of the PCC or even FRC can be seen directly at the joint. For the dowel bar with high friction (as shown in Figure 7.3 (c)), zones of compression can be seen from the bearing capacity of the steel against the concrete. Crack widths, debonding lengths and vertical deflections for a 1.51 m (5 ft.) or a 4.60 m (15 ft.) slab size are shown in Tables 7.4 and 7.5, respectively. All of the undoweled simulations predicted that the interface between the overlay and the underlying HMA became debonded; furthermore, greased dowels in short slabs also showed debonding tendencies.
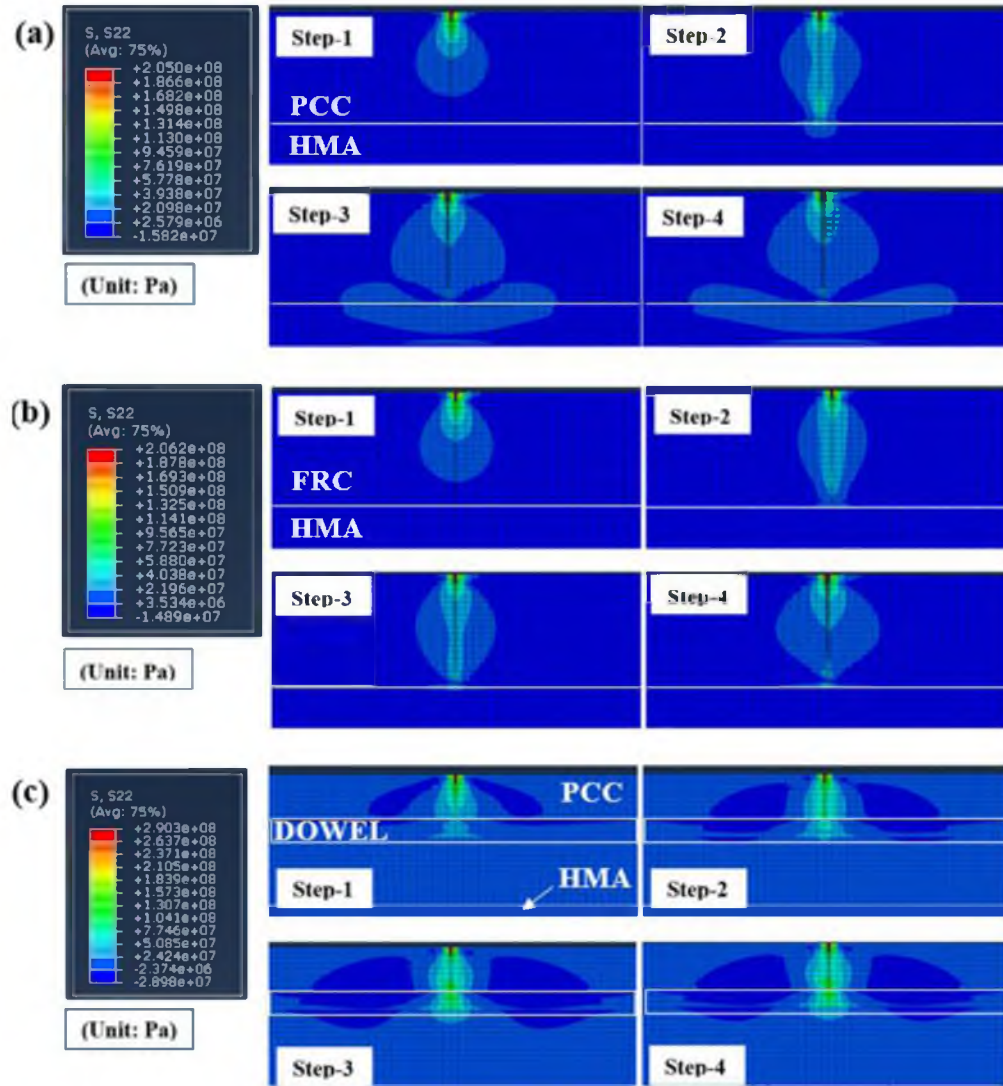
Figure 7.3. Zoomed-in stress distribution during cracking and debonding for (a) PCC without dowel; (b) FRC without dowel; (c) single dowel bar model (457 mm long, 25mm diameter dowel bar, 0.38 high friction coefficient) in PCC.

It was assumed that a plain concrete slab will show zero load transfer which can cause wider crack-opening width and higher debonding length. The use of fiber-reinforced concrete in even the 150 mm (6 in.) thick overlay does also reduce the crack width by a factor of 1.3 times compared to the plain concrete. However, dowel bars alone were more effective at reducing the crack width by 4.3 times compared to the unreinforced plain concrete.

Table 7.4 Result of sensitivity analysis for 1.51 m (5 ft.) slab

	Zero Cohesion (Precast)			
Dowel diameter	(Unit: mm)	No dowel	19 mm (3/4")	25 mm (1")
	Crack width	0.5113	0.2114	0.1511
	Debonding length	79.8942	0	0
	Vertical deflection	0.1610	0.0905	0.0503
FRC	(Unit: mm)	No dowel	19 mm (3/4")	25 mm (1")*
	Crack width	0.3758	0.1463	0.1323
	Debonding length	47.9366	0	0
	Vertical deflection	0.1173	0.0347	0.0290
Friction coefficient	(Unit: mm)	0.383736	0.092568	0.076293
	Crack width	0.1323	0.2914	0.6827
	Debonding length	0	84.2462	86.3829
	Vertical deflection	0.0290	0.0781	0.0821
Dowel bar length	(Unit: mm)	200 mm (8")	450 mm (18")	700 mm (28")
	Crack width	0.1520	0.1323	0.1142
	Debonding length	0	0	0
	Vertical deflection	0.0291	0.0290	0.0287

*default settings for other simulations

Table 7.5 Result of sensitivity analysis for 4.60 m (15 ft.) slab

	Zero Cohesion (Precast)			
Dowel diameter	(Unit: mm)	No dowel	19 mm (3/4")	25 mm (1")
	Crack width	2.56515	0.73291	0.59605
	Debonding length	255.556	0	0
	Vertical deflection	0.68534	0.06712	0.04470
FRC	(Unit: mm)	No dowel	19 mm (3/4")	25 mm (1")*
	Crack width	1.97767	0.52783	0.48532
	Debonding length	95.833	0	0
	Vertical deflection	0.45662	0.04568	0.04263
Friction coefficient	(Unit: mm)	0.383736	0.092568	0.076293
	Crack width	0.48532	0.710582	2.28571
	Debonding length	0	287.5	306.1
	Vertical deflection	0.04263	0.051	0.052
Dowel bar length	(Unit: mm)	200 mm (8")	450 mm (18")	700 mm (28")
	Crack width	0.58915	0.48532	0.43158
	Debonding length	0	0	0
	Vertical deflection	0.04124	0.04263	0.04250

*default settings for other simulations

There was slight additional reduction of crack width by 1.2 times using dowel bars and FRC combined versus dowel bars and PCC in this 150 mm thick overlay. This trend is further realized graphically in Figure 7.4 showing that the crack width is significantly reduced with dowels and only slightly reduced with the addition of fiber reinforcement across the joint.

The w, L_{deb}, and δ_{lift} were all decreased as dowel diameter increased. Figure 7.5 shows an example of the reduction in crack width versus effective reinforcement diameter. This figure combines the effects of fibers and dowels in a composite effective diameter assuming roughly 10 fibers cross the joint, each with a diameter of 0.44 mm, all summed with any possible dowel diameter to get the composite size. The δ_{lift} is reduced with FRC and even further reduced with the addition of dowels (see Figure 7.6). Of the different dowel types, longer dowel bars showed a decreased crack width but negligible change on vertical deflection. An increase in friction coefficient between the dowel and surrounding concrete showed a decrease in w, L_{deb}, and δ_{lift}.

Figure 7.7 illustrates the effect of friction coefficient between the dowel and the surrounding FRC material. The highest friction coefficient (see Figure 7.3(c)) shows that compressive stresses develop in the concrete and the interface no longer exhibits debonding. In the case of the lubricated dowels, the FEM indicated that there might be separation and liftoff of the concrete from the dowel. Figure 7.8 illustrates the zoomed-in stress distribution during cracking of dowelled FRC overlay with the lowest friction coefficient. The separation between dowel and concrete can be seen from the lowest friction coefficient only. This might be related to the slip of reinforcement due to the low friction between concrete and dowel bar under the same load condition.
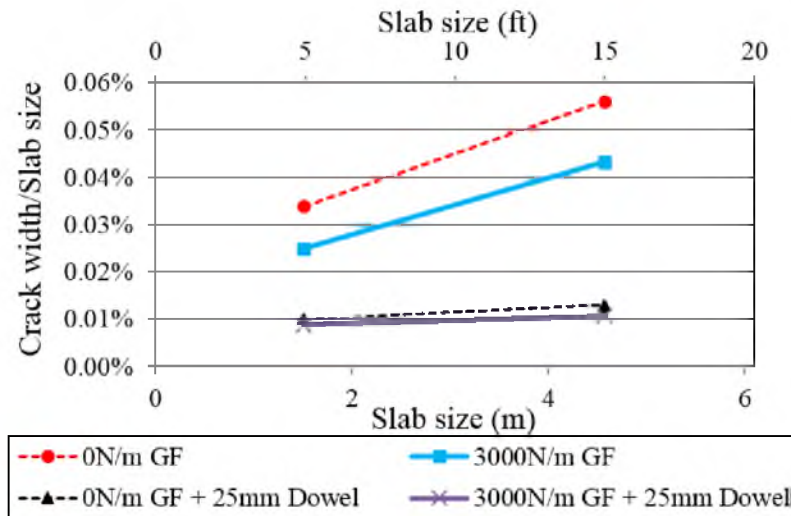
Figure 7.4. Fracture energy and dowel bar effect on crack widths relative to slab size.
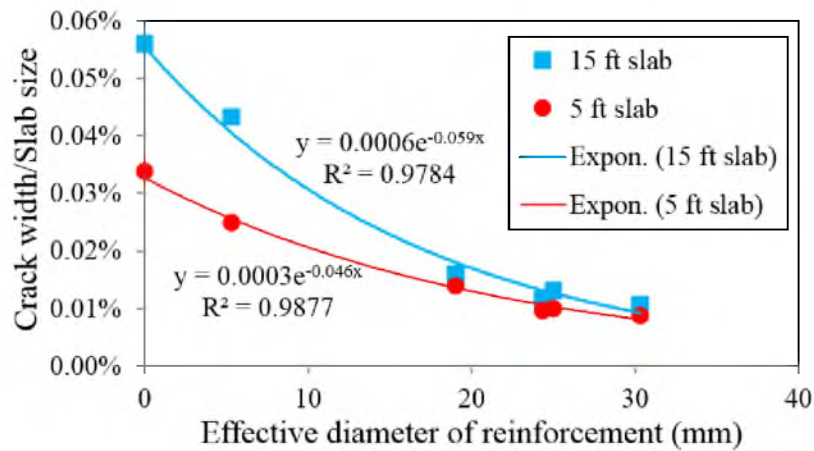

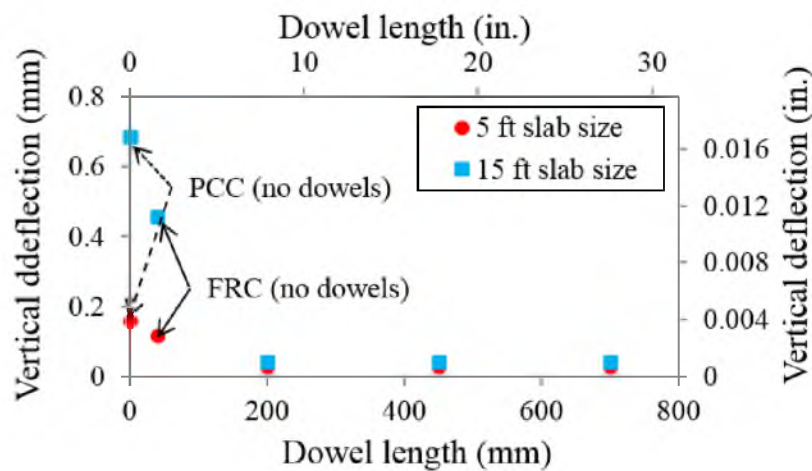Figure 7.5. Effect of dowel and/or fiber diameter on crack width.

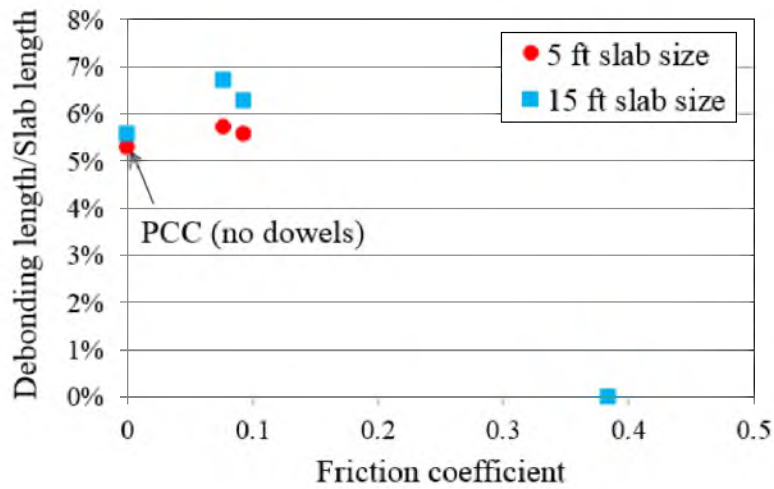Figure 7.6. Effect of dowel length on vertical deflection in an overlay.

Figure 7.7. Debonding length versus friction coefficient of dowel bars in a PCC overlay.
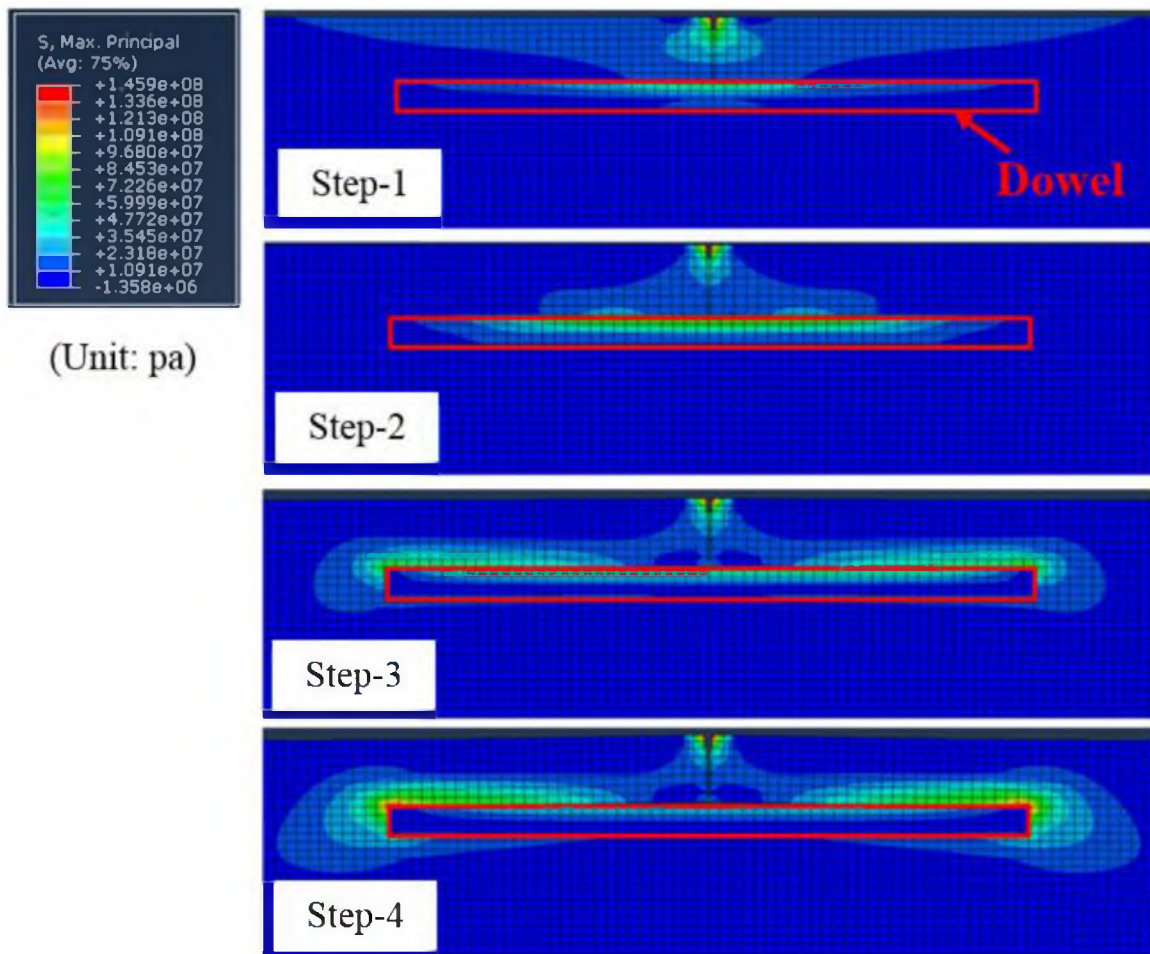

Figure 7.8. Zoomed-in stress distribution during cracking of dowelled FRC overlay with the lowest friction coefficient shows separation of concrete from dowel at joint location.

7.7 Summary and Findings

The two-dimensional modeling verified that fiber reinforcement can be comparative to dowels in resisting crack opening width, debonding length, and vertical deflection. This finite element model was modified from the previously defined model in order to compare pavements of equivalent thickness at 150 mm (6 in.). Again, two different pavement joint spacings were investigated: short panel sizes seen in thin overlays (1.5 m or 5 ft.) and more typical panel sizes for this thicker pavement (4.6 m or 15 ft.). Based on the results of analytical study, the following conclusions can be drawn.

- Fiber reinforcement does contribute to reduction in crack width and vertical deflection in thick pavements and in the presence of dowel bars, although FRC is not as effective as a larger dowel to reduce crack widths and vertical deflection.

- An increased amount of reinforcement in the joint cross-section, such as larger dowel diameters, reduced the joint opening widths and the vertical deflection.

- A high-friction coefficient between the reinforcement and the surrounding FRC overlay material prevented debonding of the interface with the underlying HMA, while also decreasing the crack widths and vertical deflections.

7.8 References

Bronuela, L.; Ryu, S.; Cho, Y. H. Cantilever and Pull-Out Tests and Corresponding FEM Models of Various Dowel Bars in Airport Concrete Pavement. *Construction and Building Materials* **2015**, *83*, 181-188.

Davids, W. G. Effect of Dowel Looseness on Response of Jointed Concrete Pavements. *Journal of Transportation Engineering* **2000**, *126(1)*, 50-57.

Ioannides, A. M.; Korovesis, G. T. Analysis and Design of Doweled Slab-on-Grade Pavement Systems. *Journal of Transportation Engineering* **1992**, *118(6)*, 745-768.

Mack, J.; Hawbaker, L.; Cole, L. Ultrathin Whitetopping: State-of-the-Practice for Thin Concrete Overlays of Asphalt. *Transportation Research Record: Journal of the Transportation Research Board* **1998**, *1610*, 39-43.

Maitra, S. R.; Reddy, K.; Ramachandra, L. Load Transfer Characteristics of Dowel Bar System in Jointed Concrete Pavement. *Journal of Transportation Engineering* **2009**, *135*(11), 813-821.

Pierce, L. Design, Construction, Performance and Future Direction of Dowel Bar Retrofit in Washington State. *International Purdue Conference on Concrete Pavement Design and Materials for High Performance, 6th, 1997, Indianapolis, Indiana, USA* **1997**, *2*.

Prabhu, M.; Varma, A.; Buch, N. Analytical Investigation of the Effects of Dowel Misalignment on Concrete Pavement Joint Opening Behaviour. *International Journal of Pavement Engineering* **2009**, *10(1)*, 49-62.

Snyder, M. B. Guide to Dowel Load Transfer Systems for Jointed Concrete Roadway Pavements. **2011**.

Khazanovich, L.; Buch, N.; Gotlif, A. *Evaluation of Alignment Tolerances for Dowel Bars and Their Effects on Joint Performance*; Michigan State University, Pavement Research Center of Excellence: 2001.

Khazanovich, L.; Hoegh, K.; Snyder, M. B. *Guidelines for Dowel Alignment in Concrete Pavements*. Transportation Research Board: 2009.

CHAPTER 8

CONCLUSIONS AND RECOMMENDATIONS

8.1 Conclusions and Contributions

This study aimed to investigate how fibers affect cracking, deflections and debonding of a thin fiber-reinforced concrete (FRC) overlay subjected to temperature loading. Based on the results of experimental and analytical studies, the following conclusions and contributions were made.

1) FRC specimens exhibited either the same or a decreased residual strength ratio between 3 and 90 days. Slender polymeric fiber with 0.5% of volume fraction showed a 69% reduction in residual strength ratio from 3 to 90 days, while short steel fiber with 1.0% of volume fraction exhibited constant residual strength ratio. This is critical because residual strength ratio measured at 28 days is commonly used in FRC overlay design, and testing age is not specified in current design method.

2) A crack width prediction equation for FRC overlays was proposed based on the Darter-Barenberg temperature and shrinkage-induced joint opening equation. It was modified to consider the addition of fibers, either as a fiber aspect ratio or a measured residual strength ratio of the FRC. The proposed equation is limited at this time to predict crack width based on single imposed thermal gradients and

single age shrinkage properties. Despite these limitations, the equation was found to predict FRC overlay crack widths within 0.19 mm (±25%) of that measured from the field-constructed 50 mm (2 in.) thin overlay subjected to environmental loading.

3) Interfacial bond tests indicated that higher fiber contents near the interface were directly related to the higher tensile bond energy. Although the wedge-split tension cube test and the bisurface shear cube test were selected methods to measure the properties based on previous research indicating these had low variability in measured properties, the results indicated these still had a high coefficient of variation (approximately 44%) for the same FRC mixture. Fiber effects on measured tensile and shear bond strengths were negligible.

4) Finite element modeling was performed, and it was found that fracture energy of at least 200 N/m was enough to resist significant crack opening, debonding and vertical deflection movement in a 50 mm (2 in.) thick overlay cut at 1.12 m (4 ft.) joint spacing and subjected to a 2 °C nighttime temperature gradient.

5) A finite element analysis comparison of pavements containing either a dowel bar or fiber reinforcement indicated that a dowel bar is 2.3 times more effective at reducing crack opening width under the same loading condition. This is because of their larger effective diameter relative to the cross-section of the joint. However, analytical results showed fiber reinforcement still can reduce crack widths, vertical deflection, and debonding length. In this regard, FRC is still a preferred reinforcement method for thin overlay to control pavement responses.

The main contribution of this research is that the FEM study proved debonding is linked to crack widths and fracture energy of FRC in thin overlays. The finite element

model also verified how the fiber affects crack widths, vertical deflections, and debonding lengths. The FRC overlay showed 28% less crack opening width, 58% less vertical deflection, and 38% less debonding length with 200 N/m of fracture energy at a joint location compared to plain concrete of 80 N/m fracture energy.

The research indicated that the fracture energy and residual strength ratio of FRC are both influenced by age. The fact that the residual strength ratio reduces with age for FRC mixtures means that overlays containing fibers are more effective at crack reduction as well as debonding and deflection reductions, when cracking forms during early ages.

A crack width prediction equation was proposed from this research to incorporate the shrinkage and residual strength age-dependent properties of thin FRC overlays. Compared to the current FRC design methodology, which uses a constant FRC property to extend fatigue life, this equation can be utilized for predicting cracking that occurs during early age thermal cycles. The equation can also be utilized to determine optimum joint spacing and thickness for the design of thin FRC overlays.

8.2 Recommendations for Future Research

In this study, k_a, which considers fiber aspect ratio showed the better crack width prediction compared to k_b, which considers fiber residual strength ratio. However, it cannot be concluded that k_a is more accurate than k_b based on this case study alone. This is because very limited field data were utilized to validate the predicted crack widths. In addition, k_a only considers fiber aspect ratio, while k_b can consider more properties, such as fiber type and fiber volume content. Thus, it is expected that k_b can give more accurate prediction than k_a. In this regard, further research is needed from field experiments to validate the new modified crack width prediction equation with overlays containing different fiber types,

fiber aspect ratios, and fiber volume contents.

Selected fibers did not show any effects on measured tensile and shear bond strengths. This is due to the fact that selected test methods do not account for curling-induced overlay debonding. The FEM study indicated that the benefits of incorporating fiber materials in overlays led to reduced cracking and curling, while experimental tests verified FRC does not increase the bond strength. Additional testing to capture the curling response in a thin overlay may be a more appropriate test for the debonding response seen in the field.

Lastly, the proposed finite element model only considers temperature and shrinkage loading at a given age, and thus more research is needed to cover fatigue effects and traffic-loading influence on crack widths in FRC overlays. Field projects are also needed to validate the brief FEM study to compare pavement responses with FRC mixtures and dowel reinforcing.